Estimation of Parabolic Microwave Antenna Movements Using Sensor Fusion

Nikhil Challa

September 29, 2023

LUND UNIVERSITY

ERICSSON

MSc Thesis
TFRT-6218
ISSN 0280-5316

Department of Automatic Control
Lund University
Box 118
SE-221 00 LUND
Sweden

Printed in Sweden by Tryckeriet i E-huset
Lund 2023

Abstract

Wireless communication has seamlessly integrated itself into our daily lives, with Ericsson pioneering the development of comprehensive mobile ecosystems. As the demand for data traffic continues to surge, the enhancement of both cellular radio systems and backhaul infrastructure remains paramount. Within this context, Ericsson leverages microwave transport network solutions to address backhaul needs. However, the implementation of microwave radio solutions introduces its own set of challenges, particularly concerning physical movements and meteorological fluctuations. The thesis focuses on analyzing a typical link using microwave radio solutions, which rely on a Line of Sight (LoS) path and narrow beam width for high gain. However, the very attribute that renders the link efficient—its narrow beam width—also renders it vulnerable to potential deterioration or malfunction due to factors such as antenna and mast movements.

In response to these challenges, the thesis puts forth a comprehensive solution involving the deployment of sensors for movement detection. This approach encompasses the development of sensor fusion models and innovative signal processing methodologies. The primary objective revolves around accurately estimating the deviation of the antenna's orientation from the optimal LoS alignment. Existing scholarly works have harnessed magnetometer data from an Inertial Measurement Unit (IMU) sensor to refine estimation precision. However, the radio system under consideration features an embedded sensor located directly on its circuitry. This circuitry is ensconced within a casing, potentially offering shielding against external magnetic fields. To bolster the accuracy of the sensor model, the proposed strategy is to incorporate Received Signal Strength Indicator (RSSI) measurements.

The research outlined within the thesis encompasses two areas. First and foremost, it seeks to establish a correlation between the movements of the antenna and the corresponding variations in the received signal strength. By probing this relationship, the aim is to arrive at an understanding of the underlying causes for the observed link degradation. The second facet of this research delves into the domain of estimation using a variant of Kalman Filter. Specifically, the thesis endeavors to estimate the deviation in the antenna's orientation from its optimal alignment. This estimation process is fortified by leveraging properties from historical data to estimate current deviations and possibly forecast future deviations. Moreover, the thesis recommends certain corrective measures that hold the potential to mitigate the impacts of link degradation. However, the implementation or validation of these corrective actions is not explicitly undertaken within the scope of this study. Instead, this constitutes a fertile ground for subsequent research investigations to explore and validate further.

Keywords: inertial measurement unit (IMU), received signal strength indicator (RSSI), extended kalman filter (EKF), numerical methods, optimization.

Acknowledgement

I extend my heartfelt gratitude to both Ericsson and Lund University for embarking on this collaborative journey aimed at tackling wireless challenges through the lens of this thesis. My sincere appreciation goes to Professor Bo Bernhardsson for his invaluable guidance in shaping the design of the Extended Kalman Filter, as well as to Senior Lecturer Emma Tegling for her time in assessing the thesis.

I would like to express my deep thanks to Frans Erik Isaksson, whose unwavering support and daily guidance have been instrumental in comprehending Ericsson's radio design, the intricacies of software architecture, and the review of embedded software code—essential for extracting sensor data. My gratitude extends to Henric Broström for his consistent guidance, and for facilitating the acquisition of the mast sway generator—a pivotal component for capturing real-world swaying data, which in turn enriched the thesis.

Chandrika Bhaskara, I am grateful for the opportunity to collaborate with Ericsson on this thesis, and for your instrumental support in timely tool and apparatus provisioning, pivotal for advancing the thesis. A special acknowledgment goes to Tobias Nilsson and Magnus Wållberg for their warm welcome to the team, and their support during the embedded software development phase, as well as their constructive input on the practical viability of the thesis research.

Furthermore, I'd like to extend my appreciation to other members at Ericsson—Anders Claesson R, Giuseppe Moschetti A, Maniteja Darisipudi, Lars Skog J, Lars Manholm, and Mikael Erdegren—for their invaluable contributions at various junctures of the thesis's progression. Your collective insights and support have proven invaluable.

Contents

List of Figures

List of Tables

Acronyms

4G	**4**th **G**eneration
5G	**5**th **G**eneration
APC	**A**daptive **P**ower **C**ontrol
AWGN	**A**dditive **W**hite **G**aussian **N**oise
BCA	**B**and and **C**arrier **A**ggregation
BL	**B**oot **L**oader
dB	**d**eci**B**el
DC	**D**irect **C**urrent
DFT	**D**iscrete **F**ourier **T**ransform
dps	**d**egrees **p**er **s**econd
EKF	**E**xtended **K**alman **F**ilter
FIFO	**F**irst **I**n **F**irst **O**ut
FIR	**F**inite **I**mpulse **R**esponse
G	**G**ravity
Gbps	**G**iga**b**its **p**er **s**econd
GHz	**G**iga **H**ert**z**
Gx	**G**yroscope **x**-axis
Gy	**G**yroscope **y**-axis
Gz	**G**yroscope **z**-axis
H/H	**H**orizontal/**H**orizontal
Hz	**H**ert**z**
I2C	**I**nter-**I**ntegrated **C**ircuit
IAB	**I**ntegrated **A**ccess **B**ackhaul
IDE	**I**ntegrated **D**evelopment **E**nvironment
IF	**I**ntermediate **F**requency
IIR	**I**nfinite **I**mpulse **R**esponse
IMU	**I**nertial **M**easurement **U**nit
KHz	**K**ilo **H**ert**z**
LoS	**L**ine **o**f **S**ight
MATLAB	**MAT**rix **LAB**oratory
MHz	**M**ega **H**ert**z**

MIMO	**M**ultiple **I**nput **M**ultiple **O**utput
mm	**m**illi**m**eter
ms	**m**illi**s**econds
OFDM	**O**rthogonal **F**requency **D**ivision **M**ultiplexing
RF	**R**adio **F**requency
RSSI	**R**eceived **S**ignal **S**trength **I**ndicator
RTOS	**R**eal **T**ime **O**perating **S**ystem
Rx	**R**eceiver (**x**)
Tx	**T**ransmitter (**x**)
USB	**U**niversal **S**erial **B**us
V/V	**V**ertical/**V**ertical
Var	**Var**iance
WSL	**W**indows **S**ubsystem for **L**inux
XPIC	Cross(**X**) **P**olarization **I**nterference **C**ancellation

1 Introduction

1.1 Network Infrastructure

Communication in today's world thrives on the interplay of wired and wireless infrastructures, a realm that has witnessed remarkable growth in recent decades. The inception of wireless technology traces back to the 1970s when wireless phones and the first professional wireless network emerged [5]. These early strides primarily catered to voice communication, and yet today, we find ourselves immersed in an era where data streams at speeds surpassing 1 Gigabits per second (Gbps).

Before delving into the intricacies of backhaul systems, it's useful to understand the fundamental components that constitute the end-to-end network infrastructure, preceding the core network stage. Figure 1 below illustrates a plausible network infrastructure layout. At the outermost edges of this framework are the ubiquitous mobile phones, engaging in communication with base stations or WiFi access points. The traffic originating from these mobile devices is directed to the Aggregation point or service provider, which then forwards it to the core network through backhaul infrastructure (e.g. millimeter wave, microwave, and wired). This network traffic subsequently finds its way to the intended destination via packet-based networks or dedicated links. For incoming traffic, this journey unfolds in a reverse manner.

In response to the growing demand for data transfer to and from mobile devices, there is a pressing need not only to improve the mobile network infrastructure but also to upgrade the backhaul infrastructure. This upgrade empowers the routing of escalated traffic volumes to their intended destinations. The broader classification of backhaul infrastructure spans both wired and wireless realms, each with its unique characteristics and capacities.

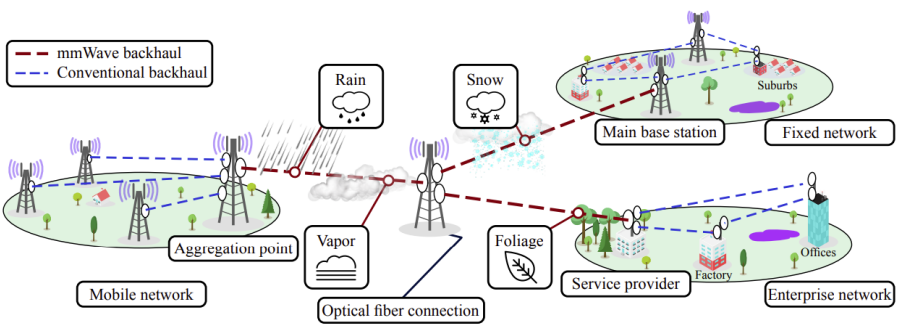

Figure 1: Network architecture [1]

The heart of this thesis resides in the analysis of wireless microwave backhaul systems, specifically with the intent to deduce and forecast antenna movements. Microwave backhaul systems, integral to the communication landscape, have evolved in response to escalating data demands. Yet, these evolutionary trajectories have engendered novel challenges that warrant examination—an exploration that shall be delved into in the next section.

1.2 Microwave Backhaul Systems

Ericsson's microwave backhaul antenna systems predominantly comprise dish antennas (Figure 2a), which hinge on unobstructed line-of-sight signals for establishing dependable communication links. Illustrated in Figure 1, the integrity of these backhaul links may deteriorate due to an array of factors, encompassing precipitation (rain, snow, and vapor), impediments (foliage, birds, and drones), or the non-rigidity of antenna mast structures (Figure 2b) that can prompt swaying induced by the wind[6]. A degradation in link quality precipitates reduced channel efficiency, consequently diminishing the data rates achievable through the link. In reaction to variations in channel quality metrics, the radio possesses the capability to adjust transmission link channel parameters. These adjustments may encompass modifications to the coding rate, modulation order, transmit power, or other elements often denoted as link adaptation[7]. This proactive approach serves to enhance the overall dependability of transmissions.

(a) Dish antenna - Ericsson (b) Mast system [6]

Figure 2: Example of a dish antenna and a mast system

The evolution of backhaul infrastructure [8] is achieved through the incorporation of the following features:

- Cross Polarization Interference Cancellation (XPIC [9])
- Band and Carrier Aggregation (BCA [10])
- Integrated Access Backhaul (IAB [11])
- Line of Sight[1]; Multiple Input Multiple Output[2] (LoS, MIMO)
- Adopting higher frequency spectrum such as E-Band [12] (60 - 90 GHz)
- Higher gain and lower impact from multipath with narrower beams

The characteristics of the antenna radiation pattern exhibit variability contingent upon diverse factors, including antenna dimensions, channel frequency, orientation concerning another antenna within a link, in conjunction with external influences unrelated to the radio system, such as weather conditions, obstacles along or near the propagation path, and other such factors.

Parabolic antennas demonstrate a highly directional radiation pattern, typically depicted using a polar radiation plot, as illustrated in Figure 3a. Alternatively, they may be represented in a rectangular radiation pattern plot, as demonstrated in Figure 3b. Both of these representations aim to illustrate signal attenuation as the antenna's orientation deviates from the LoS path. Within the thesis, LoS orientation will also be referred to as **optimal alignment** or **optimal orientation**.

In the case of perfect alignment between the transmitter (Tx) and receiver (Rx), the attenuation is 0 dB. However, as the alignment deviates, the attenuation becomes non-zero, resulting in increased signal loss at the receiver. This attenuation is separate from the attenuation caused by electromagnetic wave propagation through space, commonly known as path loss.

[1]Line of Sight : A direct path or link between the transmitter and receiver

[2]Multiple Input Multiple Output : More than one transmit antennas and more than one receive antennas

For subsequent analysis, only rectangular radiation pattern representation will be utilized but can be extended to the polar radiation pattern as well if needed. None of the subfigures from Figure 3 depict specific radiation pattern specifications; instead, they serve as visual examples for better understanding.

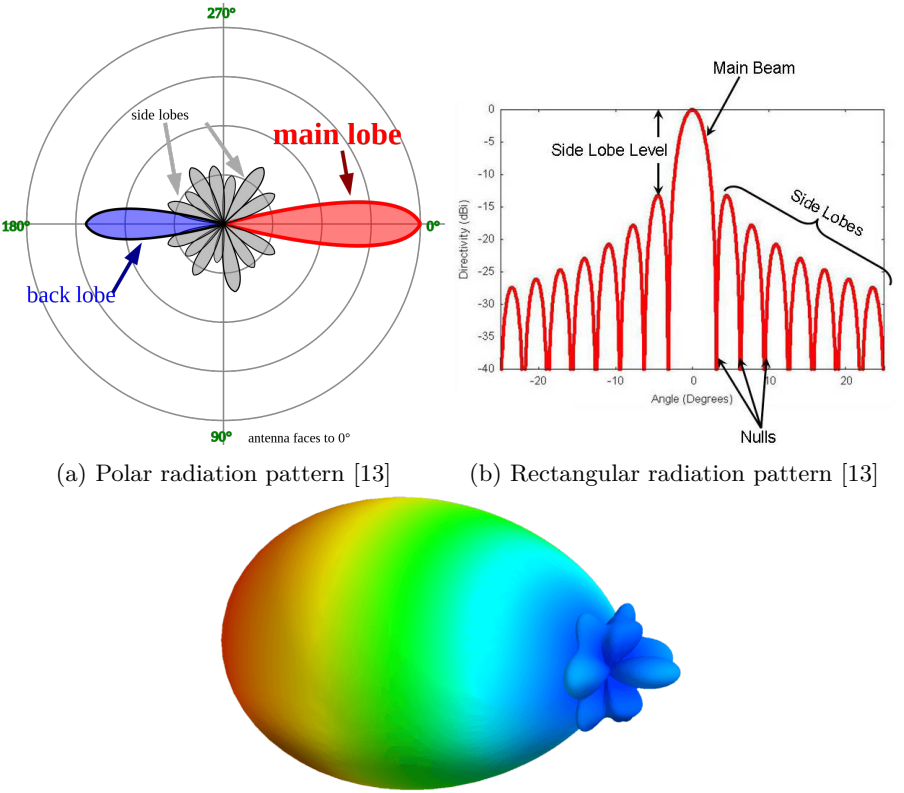

(a) Polar radiation pattern [13]

(b) Rectangular radiation pattern [13]

(c) Radiation pattern represented in 3D [14]

Figure 3: Examples of radiation patterns representations

Figure 4 depicts the radiation pattern specifications for several antennas endorsed by Ericsson for utilization with their radios in backhaul links. This graphical representation encompasses an aggregate of antenna specifications, exhibiting diversity in antenna size and channel frequency.

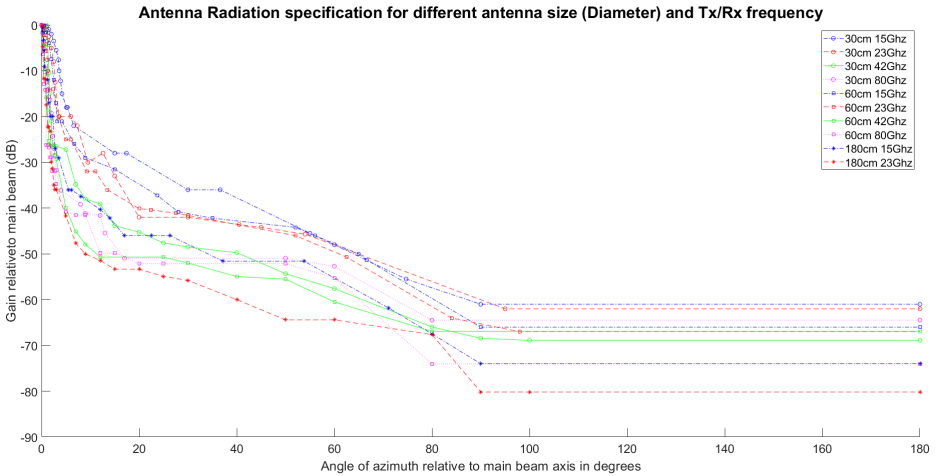

Figure 4: Antenna radiation pattern specification for different antennas

To facilitate a clearer understanding of the plot's intricacies, identical colors (or line style) correspond to identical frequencies, while consistent marker shapes signify the same antenna size. Please consult Figure 5, which specifically zooms in on the angle of the main lobe, restricting the gain to -50 dB and the angle to 10 degrees.

Within this context, two significant observations can be gleaned by confining our focus to points exclusively located within the main lobe[3] for all categories of antennas.

- Beam width tends to decrease when higher frequencies are employed
- Beam width tends to decrease when larger antenna sizes are utilized

[3]Determining the maximum azimuth angle encompassed by the main lobe might not be immediately evident solely from the visualization. For a comprehensive explanation, please consult Section 7.2.3

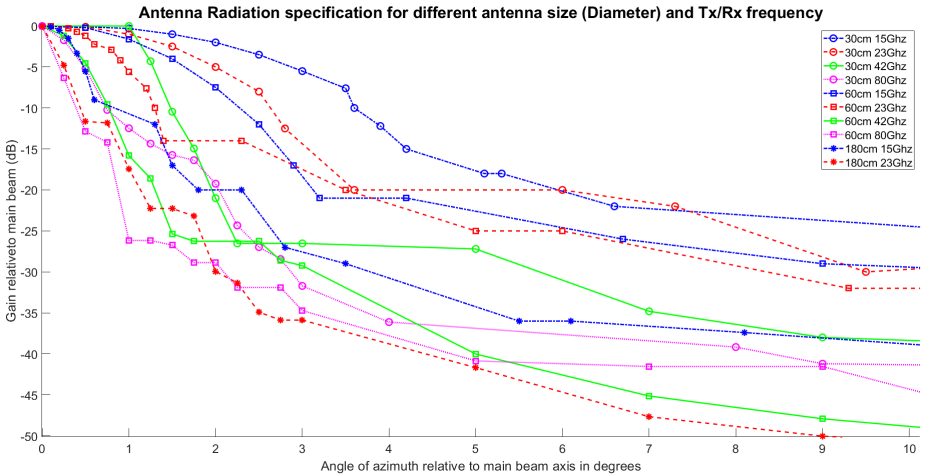

Figure 5: Antenna radiation pattern specification for different antennas - **magnified**

As microwave backhaul systems evolve to use higher spectrum and narrower beams for increased capacity and efficiency, the susceptibility to link degradation due to antenna movements becomes a significant concern. The reduction in beam width, while beneficial in terms of interference and signal gain, also makes the link more vulnerable to disruptions caused by external factors such as antenna swaying, weather conditions, and obstructions. Adopting higher spectrum and narrower beams are inevitable outcomes of the backhaul evolution, and such problems need to be addressed.

1.3 Current Research Work

Ericsson is actively engaged in research work addressing the challenge of estimating antenna orientation angle deviation from the LoS orientation using a high-quality Inertial Measurement Unit (IMU) sensor. This sensor chip installed on a separate circuitry is intended to be directly integrated onto the back surface of the parabolic reflector, strategically positioned to avoid obstructing the signal propagation path to the antenna feed (as depicted in Figure 6). By utilizing data from the IMU sensor, Ericsson aims to dynamically adjust the antenna orientation to maintain alignment with the LoS path.

While this solution holds promise and is technically feasible for deployment, it introduces a noteworthy increase in the product costs compared to conventional parabolic antennas. This cost escalation arises due to a range of necessary modifications and additions. These include the provision of a separate casing for the IMU, a separate power feed, additional cabling to link the external IMU system with the radio, creation of a new antenna physical structure to accommodate the attachment of the IMU casing, efforts to develop embedded drivers, installing a motor controlled adjustable antenna feed system, and implementation of other requisite adjustments to the existing antenna-radio systems.

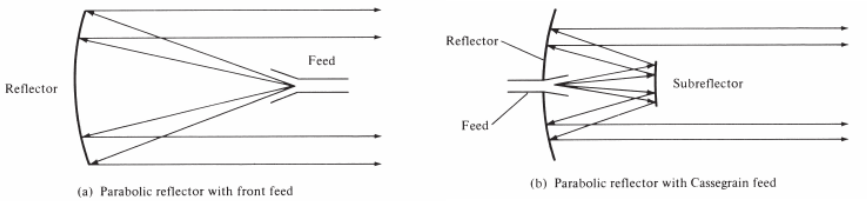

Figure 6: Common antenna feed types [2]

As part of the thesis, cost-effective options are explored to address this challenge. One such solution is to embed the IMU sensor directly onto the radio unit. This strategy aims to achieve the estimation of antenna movements indirectly, without necessitating most of the modifications outlined earlier. The key additional effort in this approach is the integration of the IMU sensor onto the radio circuit board, along with the associated driver development effort to extract the IMU data. By adopting this approach, the need for a separate IMU casing, distinct power feed, extra cabling, additional processor or microcontroller, modifications to the antenna structure, and the new motor systems to adjust antenna feed orientation can be circumvented, resulting in a substantial reduction in additional costs.

However, this alternative solution does involve certain trade-offs that warrant careful consideration. While it offers cost savings, it may introduce compromises in terms of estimation accuracy compared to the more comprehensive setup involving a separate IMU sensor installed on the back surface of the parabolic reflector. The extent to which accuracy is sacrificed for cost efficiency will need to be carefully evaluated. The scope of the thesis not only encompasses the proposal of a model to estimate antenna movements but also extends to specifying the inherent limitations of this model.

As part of its conclusions, the thesis will undertake the application of the proposed model to simulated antenna movements and manually induced mast swaying data. This practical evaluation aims to ascertain the accuracy of the model's estimations. Through these comprehensive efforts, the thesis provides valuable insights and solutions to the challenges posed by antenna movements within microwave backhaul systems.

2 Challenges and Questions

2.1 Antenna-Radio Configurations

Given that the IMU sensor is integrated into the radio unit rather than the antenna, a significant challenge emerges in accurately discerning antenna movements. This challenge is particularly pronounced when the frames of reference for the antenna and the IMU sensor are not aligned. Ericsson offers a diverse array of antenna-radio configurations, exemplified by various configurations as depicted in Figure 7. These configurations represent a comprehensive spectrum of scenarios in which the relative alignment and orientation between the antenna frame and the IMU frame can significantly differ.

Figure 7: Various backhaul antenna-radio systems provided by Ericsson [3]

The diversity exhibited by the various antenna-radio configurations leads to discrepancies in the frames of reference between the radio's integrated IMU sensor and the associated antenna. This disparity presents a challenge in applying a uniform reference frame transformation matrix across all configurations. For optimal accuracy, a tailored transformation matrix must be established for each individual configuration. However, this approach demands a dedicated transformation matrix for every existing antenna-radio setup, accompanied by ongoing costs and efforts to incorporate forthcoming configurations.

2.2 Mast Swaying Behavior

To describe the various scenarios of mast swaying, a simplified representation of the antenna, radio, and mast system is depicted in Figure 8b. This simplified model treats these components as rigid bodies and introduces the concept of "focal points" (Figure 8a) that possess a certain degree of freedom in rotational motion when an object linked to the focal point is subjected to external forces. This freedom of motion could arise from factors such as weak joints, degraded structural integrity over time, or other reasons. The main external force contributing to such motion is wind, although impacts from objects such as hailstones or any flying object could also play a role.

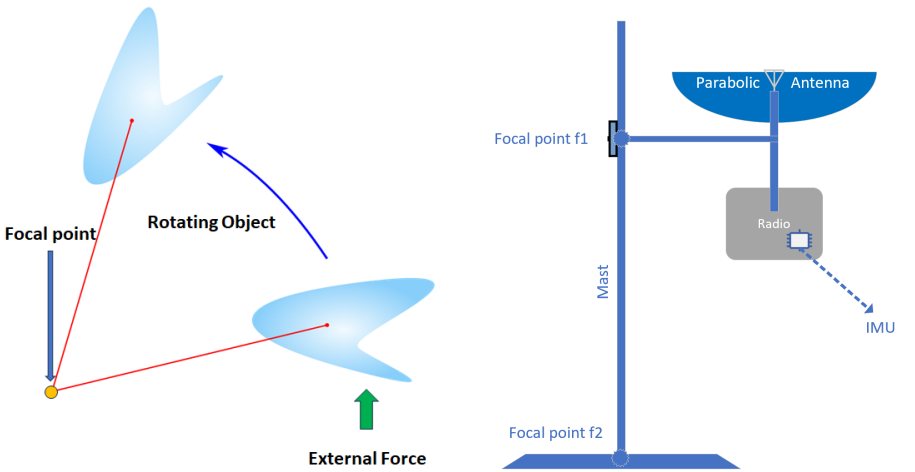

(a) Definition of focal point [15] (b) Simplified rigid body

Figure 8: Understanding focal points

The motion of the rigid body around these focal points can lead to misalignments with the LoS path. For the sake of illustration, the Figures 9, 10, and 11 depicts a configuration where the radio is directly mounted behind the antenna, and the IMU sensor's Z-axis direction is in the exact opposite direction of the antenna orientation. It is important to note that these drawings are for descriptive purposes only; the actual antenna-radio system used for data collection in the thesis does not share the same configuration. The component situated between the antenna and the radio is the waveguide [2], which is a highly rigid structure in reality.

Please refer to Figure 12 and Figure 98 (Appendix D) to visualize the antenna-radio system employed in this thesis. To comprehend the potential movements of the system, consider them as combinations of the fundamental motions illustrated in Figure 9, Figure 10, and Figure 11. On the right side of each figure, a rainbow-colored ellipsoid-shaped lobe is drawn next to the transmitter figure, which serves as an approximate visual representation of the radiation pattern's shape for parabolic antennas [2][4].

Although the drawings are original unless specified, credit for the distinctive rainbow lobe shape in the below figures goes to [14].

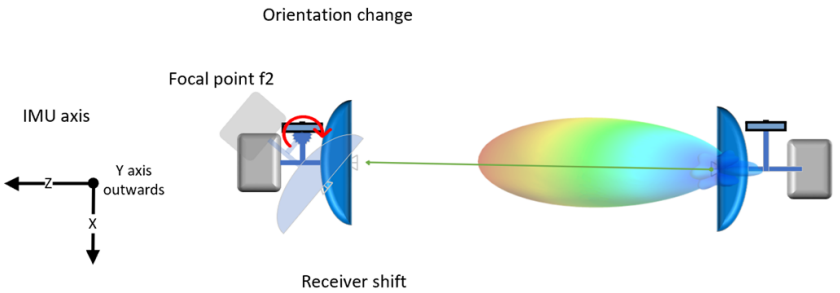

Figure 9: Case1 - Rotation around the mast (focal point 2)

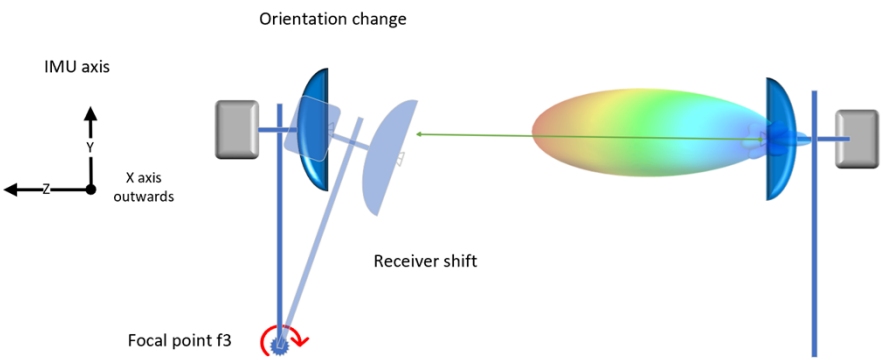

Figure 10: Case2 - Moving along the LoS path (focal point 3)

[4]Please note that the radiation pattern shapes in the figures may not necessarily align precisely with the radiation specifications of the antenna used in this thesis.

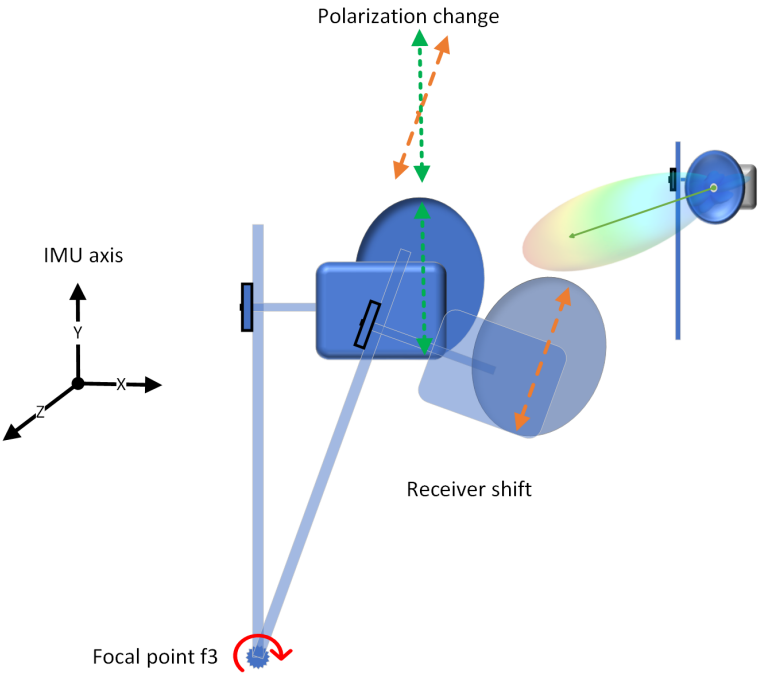

Figure 11: Case3 - Moving perpendicular to the LoS path (focal point 3)

The aforementioned figures are based on the assumption of rigid body motion, although mast systems might not necessarily be rigid. It is essential to note that only the antenna-radio system, as detailed in the preceding subsection, can be considered rigid due to the close integration between the antenna, waveguide, and radio components. The diverse range of movement types, varying focal point locations, and non-rigid structures present a substantial challenge in formulating a model to accurately characterize antenna movements.

2.3 Questions to be Answered

As previously mentioned, a key distinction from existing approaches is that the IMU sensor is not directly placed on the antenna. Instead, this thesis explores the potential for inferring antenna movements through an indirect association with movement data acquired from the IMU sensor integrated into the radio. The thesis thus aims to answer the following primary questions:

1. How can insights from existing published literature be leveraged to determine the sampling and signal processing requirements?
2. Can a correlation between received signal strength variation and IMU sensor data be effectively measured for strong oscillations?
3. Is it feasible to utilize the Kalman Filter or its variants to estimate, sample-by-sample, the deviation of the antenna oritentation from the optimal orientation?
4. What is the impact of fluctuating received signal strength on link performance, and what measures can be taken to mitigate these issues?

3 Resources Provided by Ericsson for the Thesis

Since incorporating IMU sensors onto radios is a relatively recent approach undertaken by Ericsson, there is a lack of swaying data from existing deployed networks. Therefore, a setup was arranged involving a new radio equipped with an embedded IMU chip and a motor system designed to simulate mast swaying.

3.1 Hardware Resources

- Parabolic Antenna with waveguide: ANT3 C 0.3 HPX 15 (Figure 12)
- Radio: 63xx Series
- Mast Sway Generator System: Simplex Motion Motor with an integrated rotation mechanism
- Mast on the Roof
- Transmitter system: Transmitting a wireless signal with a fixed power level at approximately 15 GHz carrier frequency.
- Node[5]
- Signal generator to test the radio
- Coaxial Cable (Power + Node connection)
- USB Type C (Extract IMU sensor data and RSSI data)
- Laptop for embedded development, data collection, and signal processing

[5]Node is a separate processing unit that connects directly to the radio to receive intermediate frequency (IF) signal for baseband processing

3.2 Software Resources

- Visual Studio: Windows based IDE for Software development
- WSL2: Linux environment for source code editing, compiling, debugging and unit testing
- MCUXpresso IDE: Load symbols onto radio, set breakpoints for real-time debugging, and hardware debugging (BL3 ARM build and debugging environment on Windows)
- TomSender: Software tool to configure radio parameters via serial port (USB)
- Logtool: Software tool to read serial port data (USB) and convert raw hex data to legible log using string maps
- TeraTerm: Open source software tool to read serial port

To simulate mast swaying, the clamps used to attach the antenna-radio system to the pole, as depicted in Figure 12, were substituted with a mast sway generator motor system, as illustrated in Figure 13.

ANT3 C 0.3 HPX

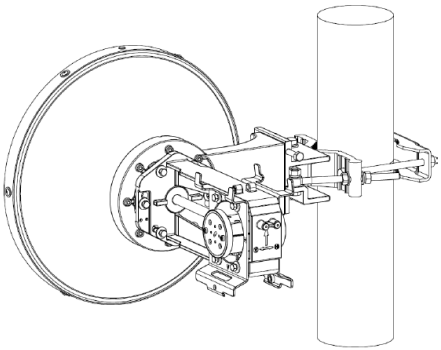

Antenna 13-42 GHz and 80 GHz.

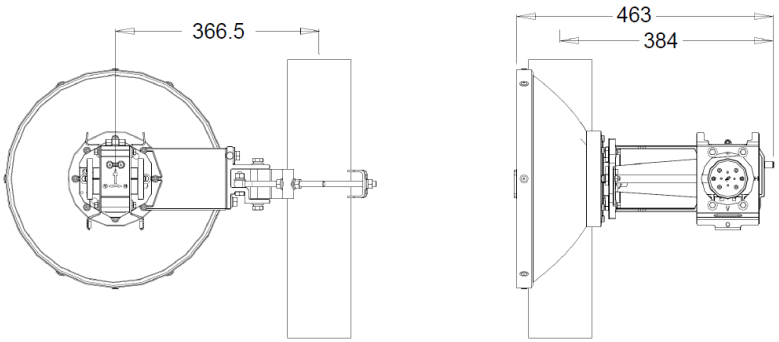

[mm]

Antenna, rear and side view.

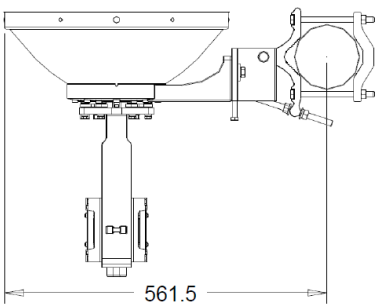

[mm]

Antenna, top view.

Figure 12: Antenna physical dimension specification (courtesy of Ericsson)

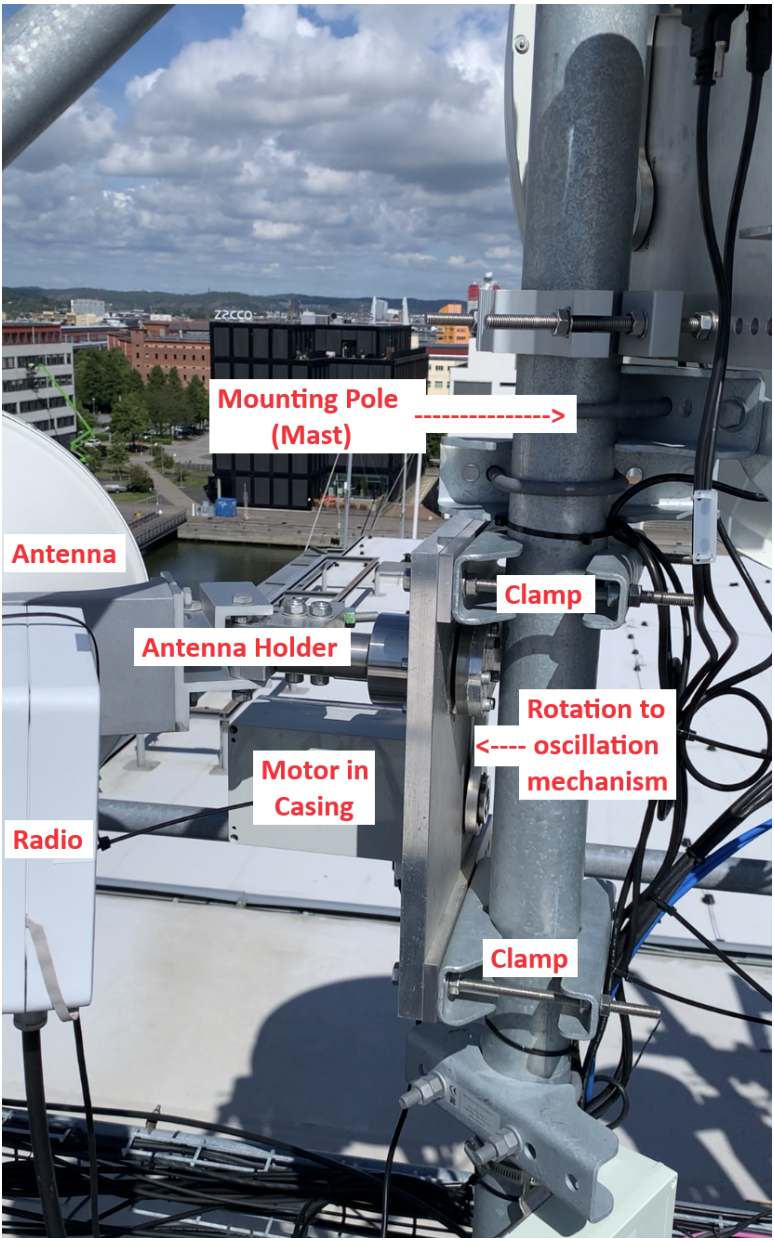

Figure 13: Mast sway system coupled with the antenna-radio system for data collection

4 Embedded C I2C Driver Development for Extracting IMU Data

Owing to the proprietary nature of Ericsson's radio software, extensive technical specifics cannot be shared. However, this section addresses fundamental signal processing requisites. For a succinct overview of the codebase, refer to Figure 14.

4.1 Data From the IMU Sensor and the Radio

The Inertial Measurement Unit (IMU) sensor offers essential information, including accelerometer data and/or gyroscope data, while certain IMU sensor models may also supply additional details such as temperature and magnetometer data. For this thesis, the selected sensor can furnish linear acceleration (G's)[6] for all three orthogonal axes, angular velocity (degrees/sec) for three rotational axes, temperature ($^{\circ}C$), and a time-stamp (counter value).

Temperature data is included in the IMU sensor results but is not utilized in the realm of signal processing or analysis. The time-stamp information plays a role in identifying any gaps in the data collection process. By assessing the continuity of values, instances of missing samples can be identified. These gaps might stem from issues such faulty external connectivity (USB disconnections) or more complex radio failures, encompassing both software and hardware malfunctions.

The RSSI measurements are obtained from a dedicated module within the radio software architecture, known as the radio controller. These measurements represent the received signal strength of the transmitter signal, and they are expressed in decibels (dB). This module interfaces with the Radio Frequency (RF) components and updates the RSSI variable value approximately every 6 milliseconds (ms).

The crux of the analysis hinges on the data obtained from key sensors: the accelerometer, gyroscope, and RSSI. These sensors provide the fundamental dataset that will be subjected to thorough examination and processing. Subsequent sections will present numerous plots displaying the data from all sensors within the IMU, along with the RSSI values collected from the radio.

[6] In this context, 'G' represents gravity, which is a predefined value $\sim 9.8 m/s^2$. The sensor's accelerometer data is provided in units of gravity ('G') rather than meters per second squared (m/s^2)

4.2 Signal Processing Requirements

The paper [16] provides an insightful overview of mast swaying, including its various properties such as the frequency range of fast swaying (0.4 Hz - 5 Hz) and the amplitude of deflections for thin poles ($1° - 4°$). Additionally, the paper discusses the occurrence of non-periodic deviations with durations ranging up to several minutes. However, the focus of the thesis will be limited to addressing fast-swaying scenarios and assuming the presence of thin poles. Thicker poles tend to exhibit lower deflections, which makes their estimation relatively simpler given sufficient measurable movements.

Regarding non-periodic slow deviations, these can be tracked using methods such as monitoring the shift in gravity direction through accelerometer data, a technique commonly employed in digital angle finders. However, this method might not work effectively for movements where the direction of gravity remains constant, such as pure twists (rotational motion axis aligns with the direction of gravity) or vertical movements (direction of motion perfectly aligned with gravity). Furthermore, translating linear acceleration data into angular motions can be challenging, especially if the exact focal point of rotation is unknown [17]. For these reasons, the thesis will not cover methods relying on accelerometer data.

The fluctuations in RSSI caused by swaying can manifest within a frequency range spanning from the mast swaying frequency (one-sided oscillation from peak - Figure 21) to twice the mast swaying frequency (balanced two-sided oscillation across peak - Figure 19). Given a maximum mast swaying frequency of 5 Hz, this implies that RSSI fluctuations can occur at frequencies up to 10 Hz. In signal processing tasks such as filtering and frequency domain analysis on the RSSI signal, it's essential to adhere to the Nyquist theorem, which stipulates that the sampling rate should be at least twice the maximum frequency of interest ($10 \text{ Hz } \times 2 = 20 \text{ Hz }$).

For effective filtering, both IIR and FIR filters necessitate a transition from the pass band to the stop band frequency, referred to as the roll-off [18]. To ensure that the roll-off has minimal impact on the frequency of interest, oversampling is recommended. Therefore, a sampling rate of 100 Hz has been selected for both the IMU sensor data and RSSI measurements. It's worth noting that while the IMU sensor is capable of very high sampling frequencies (> 6 KHz), increasing the sampling frequency introduces higher noise levels in measurement data and quicker processing requirements. It is counterproductive to exploit higher sampling frequencies unless there are clear signal processing benefits.

4.3 Data Collection Methodology

As part of thesis work, a commercially low cost IMU sensor chip was mounted on a radio but required driver development to extract the IMU data from the sensor chip. Since there was no provision for an interrupt from the IMU sensor chip to the radio's processor for the provided radio system, an alternative approach was taken to extract IMU data. The method employed deviates from the use of a First-In-First-Out (FIFO) mechanism [19] for extracting IMU data. Instead, a straightforward approach was adopted wherein sensor data is read through register access at pseudo-periodic intervals, achieved by introducing a sleep interval of 10 ms between consecutive register reads. With this approach, a sensor data reading is obtained approximately every 10 ms, resulting in a sampling rate of about 100 Hz. This sampling rate aligns with the recommendation put forth in the preceding subsection. The specific register values and configurations utilized for interfacing with the IMU sensor are documented in Appendix B.

4.4 Packing IMU Sensor Data and RSSI Data

The software module responsible for collecting data from the IMU and the radio controller will be termed as "data gatherer". Potential conflicts can arise when simultaneous write-to-variable operations (performed by the radio controller) and read-from-variable operations (executed by the data gatherer) occur for the RSSI data. This necessitates the implementation of critical sections, similar to mutex locks[20], to ensure data consistency. Given that the radio software operates on the FreeRTOS [21] platform, the processes involving writing to and reading from variables are encapsulated within what is termed a "task critical section".

The raw binary data retrieved from the IMU sensor registers undergoes a processing step to convert them into floating-point numbers. These processed sensor readings are then structured and organized into a unified format. Following this organization, the data is transmitted through a USB interface. Once received, this data can be accessed and read using applications capable of serial port communication. It is crucial that the tool being used understands the data encoding format. MATLAB[22] software was utilized for various tasks, including the reading of serial data and subsequent signal processing on the data.

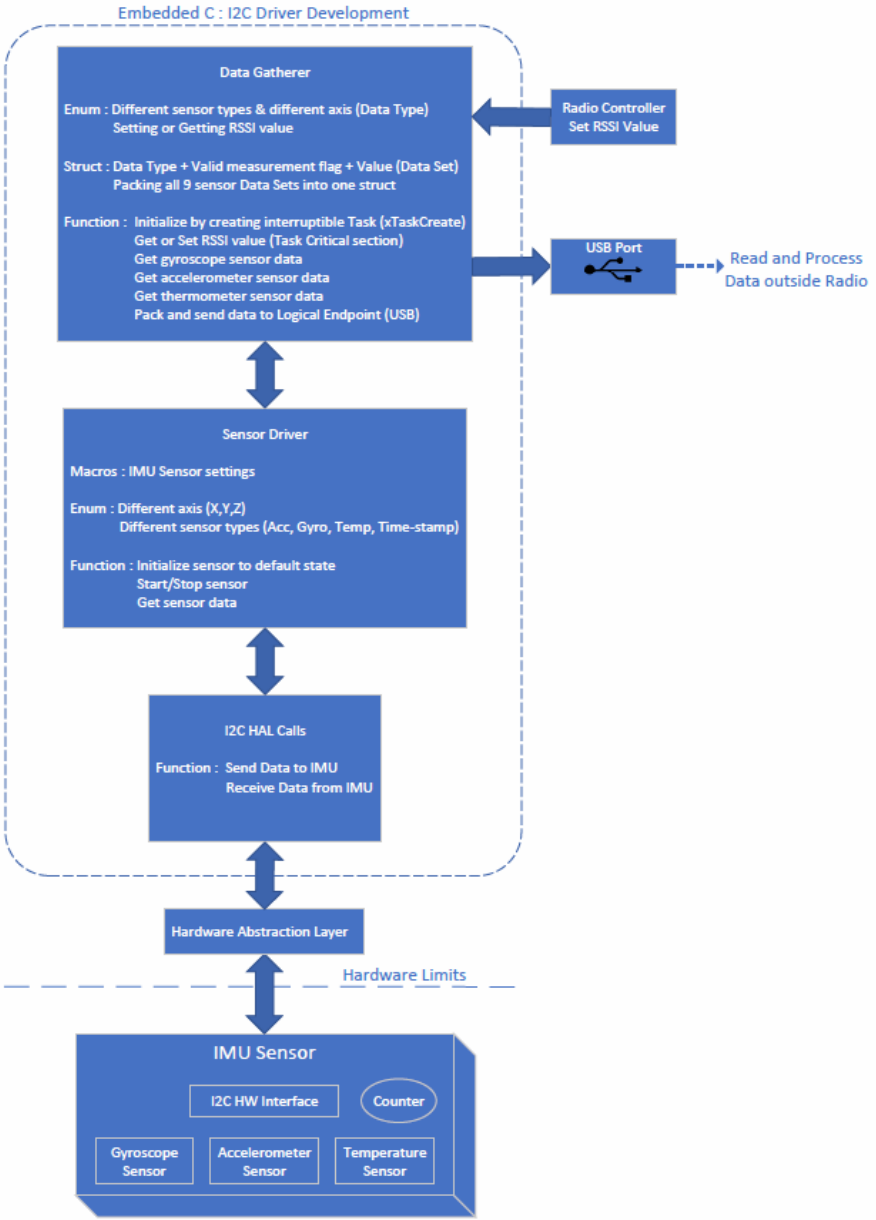

Figure 14: Overview of software development work and various hardware components

5 Understanding IMU Sensor Data and RSSI Data for Various Movements/Oscillations

Before delving into the specifics of signal processing, it's important to highlight certain characteristics of sensor outputs. These characteristics need to be taken into account when calculating the correlation factor and developing the final estimation model. The following impacts should be considered:

- Sensor bias error
- Stochastic noise
- Short deep fades in RSSI value
- Attenuation in RSSI value due to precipitation such as rain, fog, snow, etc

In this thesis, the terms "balanced oscillation" and "unbalanced oscillation" have been introduced to describe the two contrasting scenarios of antenna oscillations. As illustrated in Figure 15, if the antenna oscillates equally on both sides of the optimal orientation or LoS alignment, it is referred to as a "balanced oscillation". Conversely, if the antenna oscillates exclusively on one side of the optimal orientation, it is termed an "unbalanced oscillation". There are also cases of "partially balanced" (or partially unbalanced) oscillation that fall roughly between the balanced and unbalanced type. Due to challenges in simulating exact balance or unbalanced cases, terms such as "almost balanced" and "almost unbalanced" oscillations are used to denote scenarios that are in proximity to the balanced and unbalanced type respectively.

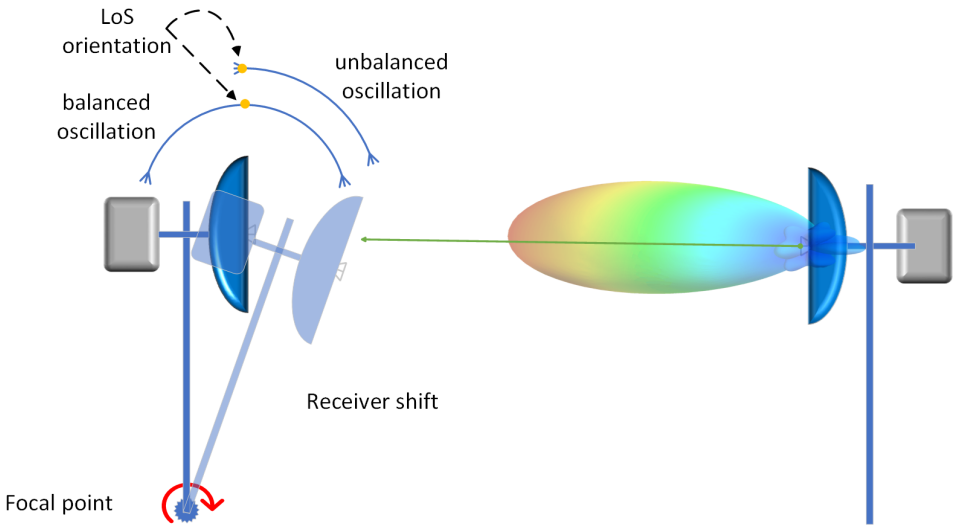

Figure 15: Balanced and unbalanced oscillation

To gain familiarity with the terminology, the proposed transition terms between balanced and unbalanced are as follows:

balanced ↔ almost-balanced ↔ partially-balanced[7] ↔ almost-unbalanced ↔ unbalanced

↔ signifies proximity of the oscillation type. Moving from left to right in the above terminology sequence, "balanced" and "almost-balanced" exhibit a slight difference. In the case of "balanced", the antenna sways approximately equally on both sides of the optimal alignment. Conversely, "almost-balanced" implies that the antenna sways slightly more on one side of the optimal alignment. If the oscillation angle on one side of the optimal alignment is about half that of the other side, it is considered "partially balanced". When the oscillation is predominantly on one side of the optimal alignment, it falls into the category of "almost-unbalanced". If the oscillation is entirely on one side, it is termed "unbalanced".

Most swaying systems fall into a category between balanced and unbalanced oscillation, and is further elobarated with different logs possessing different oscillation types. Some oscillations fall outside this category, explained with samples logs and in Section 7.1.2.

[7]"partially balanced" and "partially unbalanced" represent the same type of oscillation, but only "partially balanced" term will be used

In the following subsection, 10-second logs are presented, each accompanied by a concise description. These logs provide examples of different scenarios, showcasing the signal's characteristics and variations. The analysis encompasses both the time and frequency domains. Majority of the data is generated through motor-induced mast swaying to simulate real-world conditions. Nonetheless, certain cases are not representative of the natural mast swaying behavior or represent extreme corner cases that pose significant challenges for modeling. In such instances, a statement "will not be addressed within the thesis" is highlighted in red and underlined for clarity.

In certain logs that exhibit oscillatory behavior, frequency domain analysis is employed to identify peaks. By utilizing peaks detected from various sensors, we can derive properties that are subsequently utilized in the determination of model parameters for estimating antenna movements. The cross-visualization between the time domain and the frequency domain provides additional properties that can be valuable in later stages.

On the other hand, stationary logs primarily serve to highlight "bias" errors present in the IMU sensor data. These bias errors, alongside other properties such as Allan variance, are carefully documented and become valuable information for later stages of the analysis, correction and estimation processes.

As detailed in Section 4, the data gatherer operates by collecting sensor data from both the IMU and the radio. Subsequently, it transfers this data in the form of a standard packet over USB. MATLAB utilizes serial port read functions to receive and unpack the incoming packets, storing each set of sensor data using distinct variables. The sampling rate employed in this process is 100 Hz, resulting in a total of 1000 samples gathered over a 10-second duration.

5.1 Case1: Stationary System

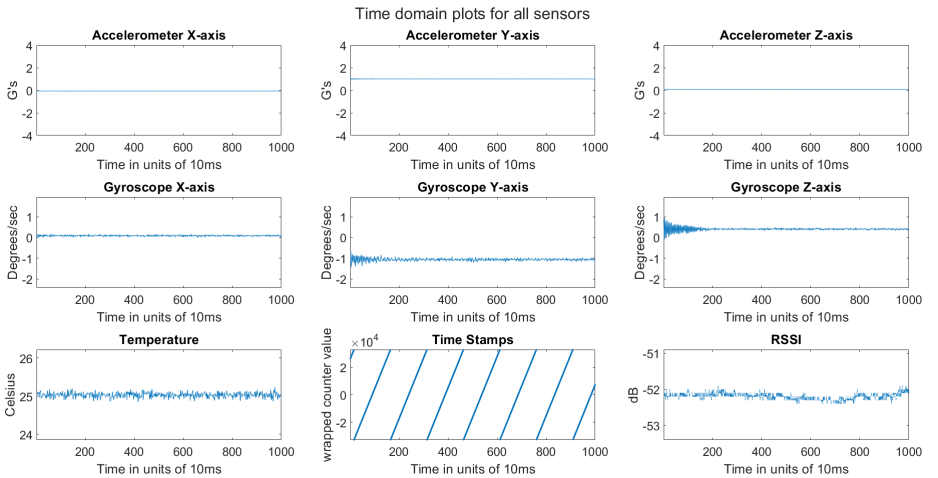

Figure 16: Sensor data - Stationary (time domain)

Figure 16 represents an example of an almost stationary antenna-radio system. In an ideal IMU sensor, the gyroscope values should be close to zero. However, most IMU sensors exhibit a non-zero offset, known as bias error. This bias error remains relatively consistent over the sensor's lifecycle unless the sensor undergoes significant physical movements or impacts. When estimating antenna movements, it is crucial to consider and incorporate these bias errors into the proposed models. This is essential for accurately estimating the deviation of antenna orientation from its optimal alignment.

It's crucial to note that when representing sensor data, there's a distinction in scaling. The accelerometer and gyroscope data employ a linear scale, while the RSSI data is expressed in decibels (dB), which utilizes a logarithmic scale.

Minor variations in RSSI can occur even under relatively stable conditions. The non-stationary nature of the medium between the receiver (Rx) and transmitter (Tx), including factors such as airborne particles, objects such as foliage, and humidity in the air can induce RSSI variations. These variations can also arise from the receiver's signal processing characteristics and thermal noise generated by hardware components.

For the given radio equipped with the embedded IMU sensor, Table 1 presents the bias error and variance associated with the gyroscope data and RSSI data. The bias and variance values were obtained by keeping the radio in a stationary position for extended periods of time. Multiple logs were collected with the radio in a stationary position with different orientations, and the mean values of the measurements are presented. Information pertaining to the log data for this dataset can be located in Appendix E.

Sensor	**Gx**	**Gy**	**Gz**	**RSSI**
Bias	0.10	-1.14	0.33	NA
Variance	6.9×10^{-4}	9.8×10^{-4}	6.2×10^{-4}	23.5×10^{-4}
Allan variance	6.76×10^{-6}	7.84×10^{-6}	5.76×10^{-6}	NA

Table 1: Bias and variance info for gyroscope sensor and RSSI sensor

Obtaining equivalent data for accelerometers is more complex due to the presence of natural gravity, which can affect multiple axes unless the radio is perfectly aligned with the force of gravity. Achieving such precise alignment can be challenging without specialized leveling equipment, resulting in bias errors in the sensor's accelerometer measurements and some degree of influence from gravitational forces. The difficulty lies in determining the proportion of the measurement data that is attributed to bias error as opposed to natural gravitational effects. This serves as an additional justification for excluding accelerometers from the final model.

5.2 Case2: Manually Induced Oscillations, Unbalanced

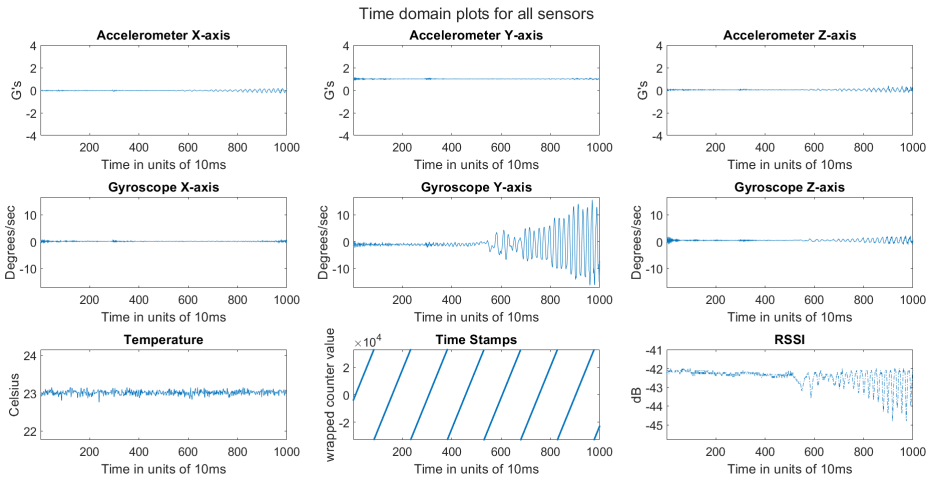

Figure 17: Sensor Data - Delayed manually induced oscillations (time domain)

Irrespective of the oscillation type, Figure 17 illustrates a behavior commonly observed in various structures: oscillations around the resonance frequency when influenced by an external force. This behavior often leads to a dominant frequency component in the frequency domain analysis (IMU sensor data[8], namely accelerometer and gyroscope data), with relatively weaker energy distributed across other frequencies. This behavior can be leveraged in the signal-processing techniques. As depicted in Figure 18, a strong frequency signal can be observed around 5.2 Hz for sensors that exhibit favorable excitations.

[8]RSSI may have two dominant frequency components depending on the type of oscillations, and will be discussed in greater detail in subsequent sections

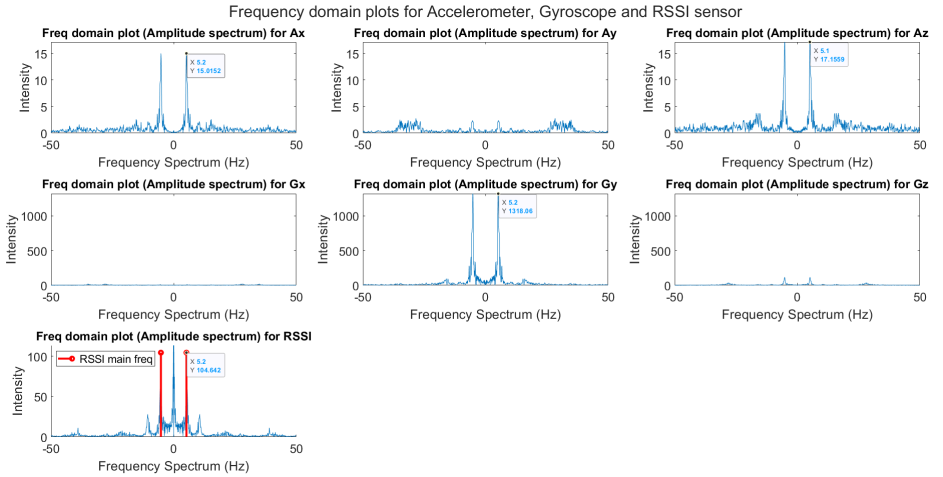

Figure 18: Sensor Data - Delayed manually induced oscillations (frequency domain)

Before conducting the Discrete Fourier Transform (DFT), the mean value was subtracted from the sensor data to reduce bias error. This adjustment ensures that the intensity at 0 Hz or the Direct Current (DC) offset component is not vital in the frequency domain analysis. The focus can then be on the oscillatory frequency components. For one sided RSSI oscillation (unbalanced oscillation), subracting the mean value does not remove the DC component.

The non-DC component (higher than 0.5 Hz and below 10 Hz) is picked up as primary oscillation frequency, as shown in RSSI stem plot in red. The peak RSSI sensor frequency is about 5.2 Hz, similar to the gyroscope and accelerometer frequency. The term "RSSI main freq" (shown in Figure 18, subplot *Frequency domain plot (Amplitude spectrum) for RSSI*) should signify the frequency that best characterizes a well-balanced oscillation (approximately double the gyroscope or accelerometer frequency). In instances of unbalanced oscillation, the DFT plot fails to exhibit a robust signal (frequency component) indicative of a balanced scenario. Consequently, this poses challenges when attempting to accurately estimate certain model parameters.

Due to challenges in computing K_{gyro} (described in Section 7.9) and calculating β parameter for modeling (described in Appendix G), this case of pure unbalanced oscillation will not be addressed within the thesis.

5.3 Case3: Motor Induced Oscillations, Almost Balanced

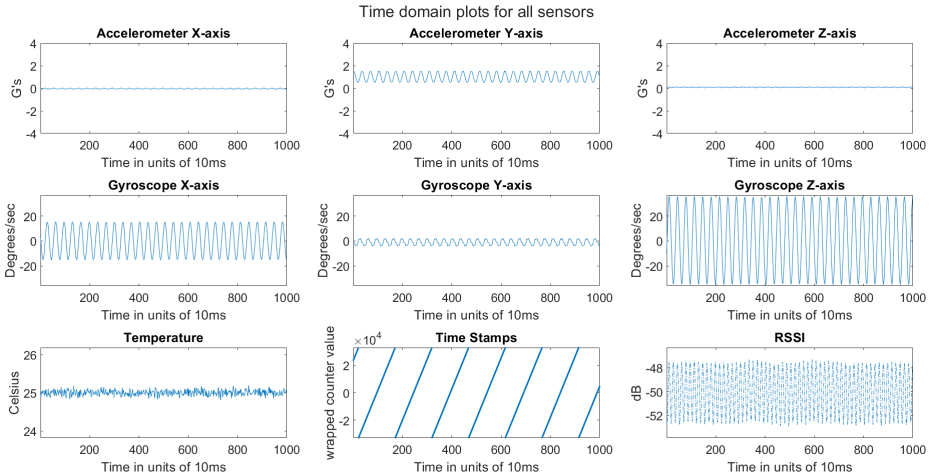

Figure 19: Sensor Data - Motor induced oscillations, almost balanced (time domain)

Figure 19 depicts an example of an almost balanced RSSI oscillation. This situation arises when oscillations occur in a manner that consistently passes through the optimal orientation, covering almost equal angles on both sides of the optimal orientation. Notably, there's a difference in the relative Gyro-RSSI frequency shown in Figure 20 as compared to Figure 18. In cases of balanced oscillations, the frequency of RSSI variations will be approximately double that of the sensor frequency. At each end of the oscillations, the RSSI value reaches a local minimum. Over a complete mast swaying cycle, the RSSI hits the local minima twice, resulting in a frequency that is twice that of the oscillation frequency.

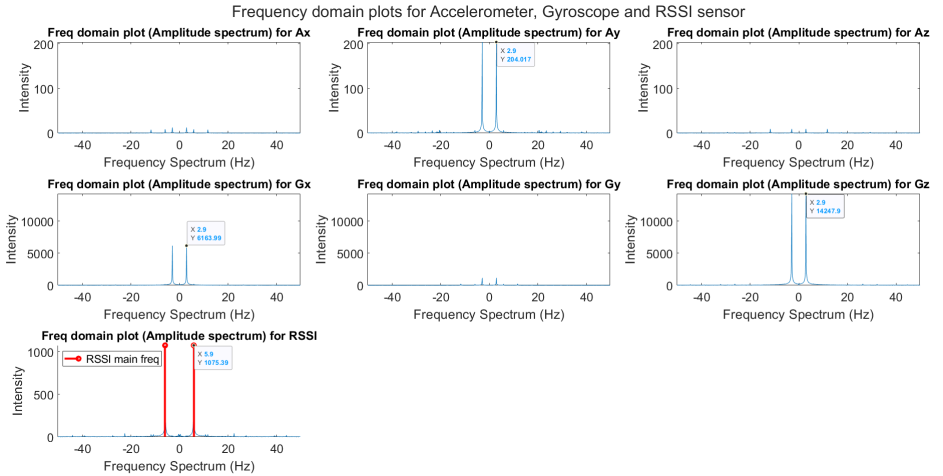

Figure 20: Sensor Data - Motor induced oscillations, almost balanced (frequency domain)

The RSSI sensor value oscillates at a frequency of approximately 5.9 Hz, which is roughly twice the frequency of the gyroscope and accelerometer sensors, both at approximately 2.9 Hz. The deviation from an exact integer multiple is attributed to the resolution limit of 0.1 Hz due to the DFT size.

5.4 Case4: Motor Induced Oscillations, Almost Unbalanced

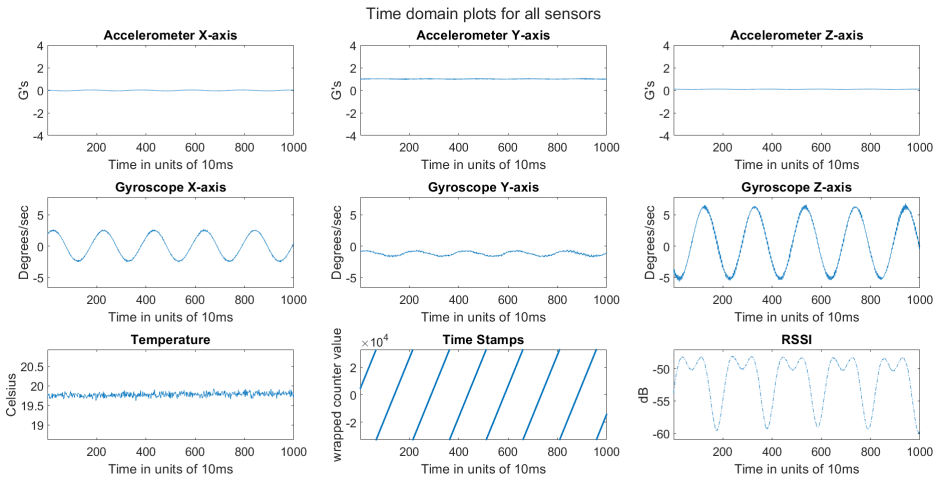

Figure 21: Sensor Data - Motor induced oscillations, almost unbalanced (time domain)

Figure 21 illustrates a more general scenario of almost unbalanced RSSI oscillations. In this case, the antenna direction passes through the optimal orientation but with unequal angles on both sides of the optimal orientation. Such a situation could arise from improper initial antenna alignment (antenna not at optimal orientation even in stationary state) or a deviation from the optimal orientation due to continuously induced external forces. To develop a model for estimating antenna movements, it becomes necessary to accurately estimate the deviation of the antenna from the optimal orientation. The methodology employed is explained in more detail in Section 7.8.

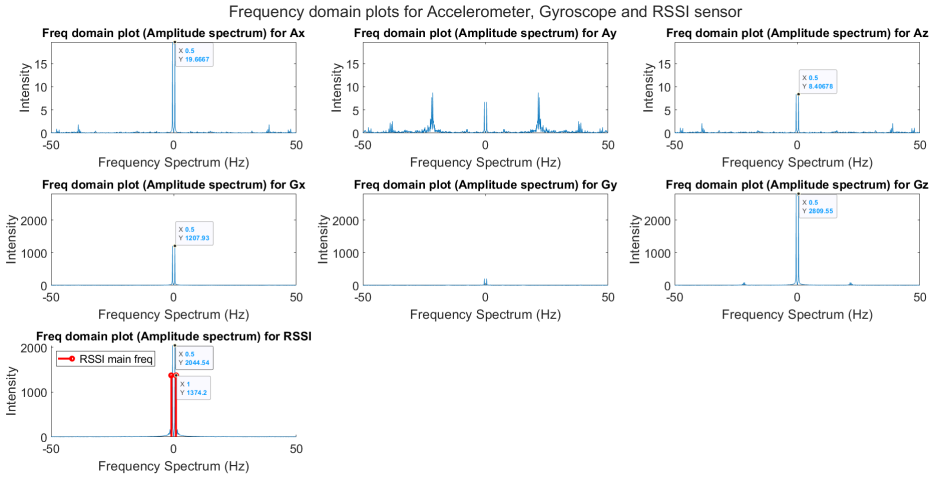

Figure 22: Sensor Data - Motor induced oscillations, almost unbalanced (frequency domain)

Owing to the inherent imbalance within RSSI signal oscillations, a duality of robust frequency components (0.5 Hz and 1 Hz in Figure 22, subfigure *Freq domain plot(Aplitude spectrum) for RSSI*) emerges, contrasting with the singular dominant frequency component below 10 Hz evident in the IMU sensor data (all other subplots in the same Figure 22).

5.5 Case5: Motor Induced Oscillations with Short Deep Fade

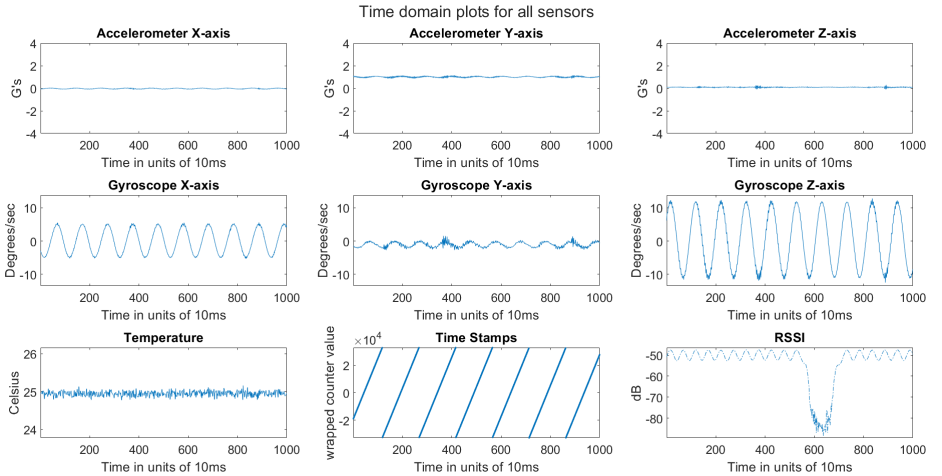

Figure 23: Sensor Data - Motor induced oscillations, with deep fade (time domain)

Figure 23 ("RSSI" plot at around 600 unit on the Time axis) illustrates a scenario characterized by deep fading resulting from a temporary obstruction to the LoS path during a balanced oscillation. Though uncommon, it is possible for natural objects such as birds [23], floating objects, flying objects (e.g. drones), or humans on the roof to intermittently obstruct the LoS, albeit for brief periods. The model needs to exhibit resilience against such drops in RSSI values, ensuring its ability to gauge antenna deviations by leveraging data from IMU sensors during periods of disrupted communication links.

5.6 Case6: Motor Induced Oscillations with Slight Variation in Oscillation Frequency and High Variance in Peak RSSI

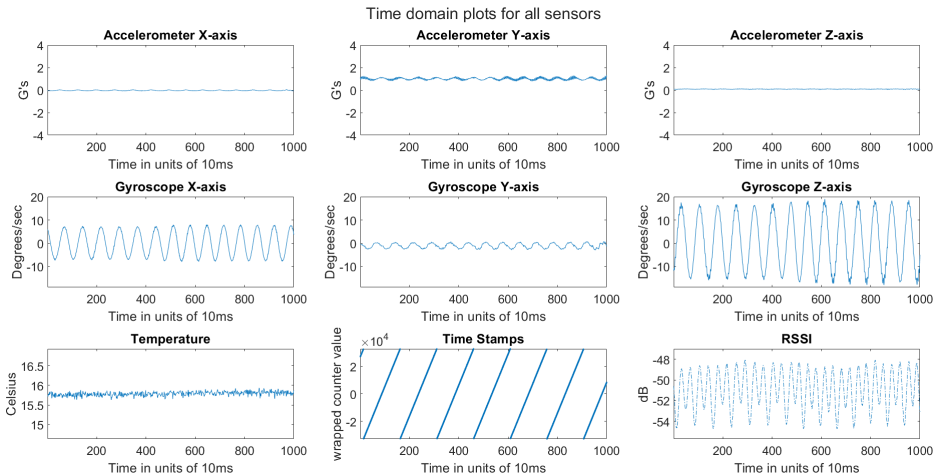

Figure 24: Sensor Data - Motor induced oscillations, increase in oscillation frequency (time domain)

Figure 24 depicts a more natural oscillation process characterized by a minor decrease or increase in oscillation frequency over time. This phenomenon could occur due to various factors such as gradual changes in wind velocity or direction, as well as energy dissipation over time. It's worth noting that an increase in oscillation frequency results in higher peak values in the gyroscope sensor data, as the swaying object needs to complete the same oscillation cycle in a shorter time (indicative of faster rotational movements). On the other hand, a decrease in frequency leads to the opposite effect. The gyroscope Z-axis peak values exhibit distinct levels in the first and second halves of the plot, offering insight into the underlying changes in oscillation characteristics. While the example was motor-induced, similar processes occurring naturally might be linked to wind behavior (direction change) or energy dynamics (energy dissipation from oscillating obejcts).

Observing the RSSI data, a scenario unfolds marked by a higher variance of peak RSSI power, despite the relative constancy in gyroscope behavior except for its oscillatory pattern frequency. This distinct behavior frequently materializes during instances of rainfall or heightened precipitation. Rainfall induces supplementary signal attenuation, albeit with a stochastic essence, culminating in this capricious amplitude fluctuation.

To precisely gauge the departure of the antenna orientation from the optimal alignment, it becomes imperative to accurately ascertain the peak RSSI value (value at zero rainfall induced attenuation and optimal alignment). Given the stochastic attribute of this phenomenon, a potential remedy involves computing the peak value across a wide sampling window of past data (e.g. a 10-second window) and incorporating this data into the model to estimate antenna movements with greater accuracy.

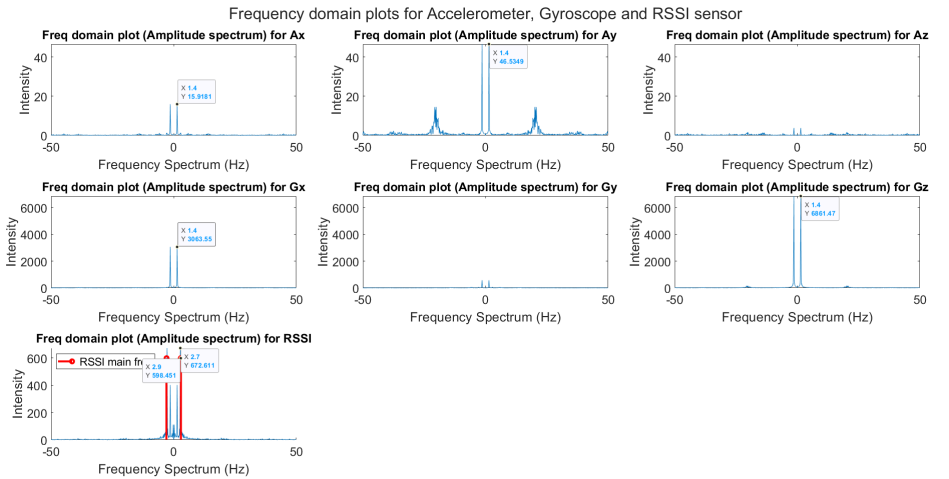

Figure 25: Sensor Data - Motor induced oscillations, increase in oscillation frequency (frequency domain)

There is a slightly wider frequency spead around the peak component, as compared to oscillations with stictly one frequency component, attributed to the slight variation in oscillation frequency.

5.7 Case7: Motor Induced Oscillations with Bad Jitter

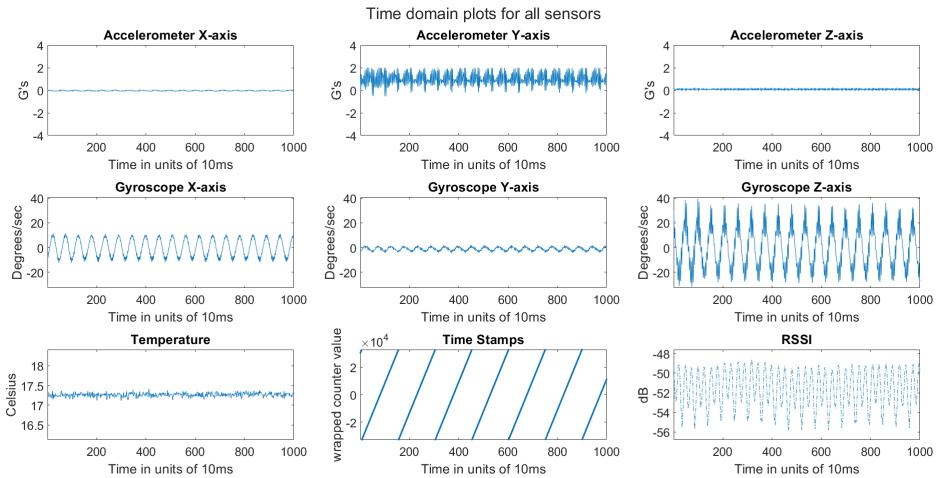

Figure 26: Sensor Data - Motor induced oscillations with bad jitter (time domain)

Figure 26 illustrates a scenario characterized by bad jitter in the system, leading to an exceptionally high frequency of vibration in the sensor data. Although strong jitters are not likely to occur, minor jitter due to inherent noise is more common. The model for estimating antenna movements should be designed to be robust in the face of such sensor data irregularities. An extreme version of this scenario can exhibit a strong high-frequency component (> 10 Hz), alongside a moderate-frequency component, in the gyroscope data (e.g. gyroscope Z-axis). This occurrence could arise when mast structures possess multiple weak joints.

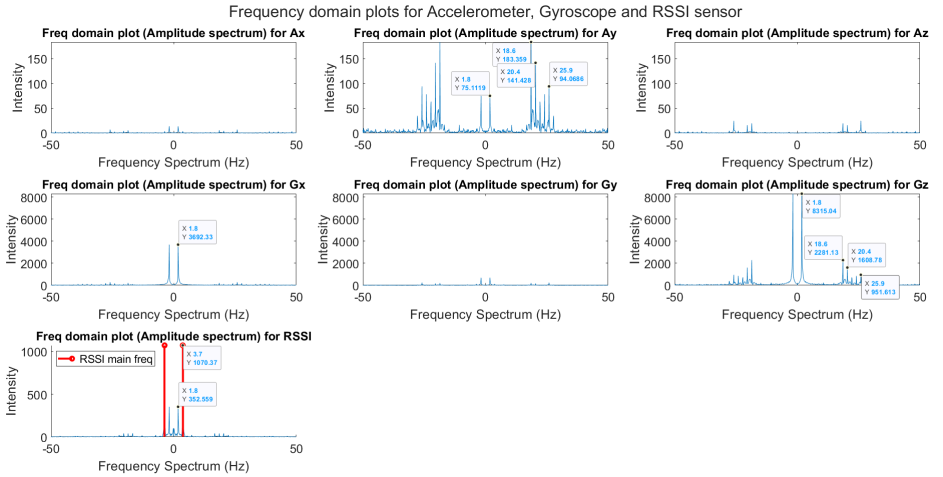

Figure 27: Sensor Data - Motor induced oscillations with bad jitter (frequency domain)

In addition to the primary oscillation frequency observed in the IMU sensor data at 1.8 Hz, several other significant components are present, notably at 18.6 Hz, 20.4 Hz, and 25.9 Hz, among others. To effectively address the issue of undesirable jitter, it is recommended to implement a filtering mechanism that attenuates frequency components exceeding 10 Hz. This filtering method is explained in more detail in Section 6.2 and will contribute to mitigating the adverse effects caused by these high-frequency oscillations.

5.8 Case8: Motor Induced Oscillations with Null Crossings

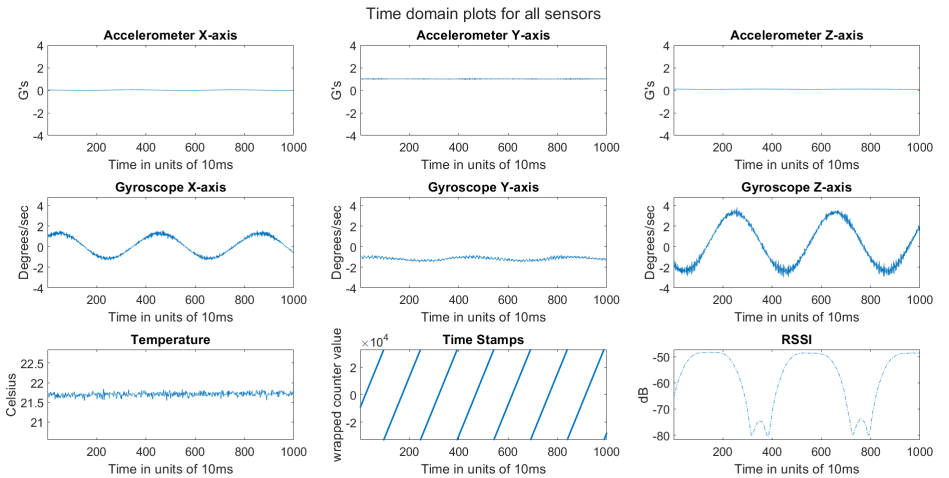

Figure 28: Sensor Data - Motor induced oscillations, with nulls (time domain)

Figure 28 presents an instance in which the antenna transitions into null points within the radiation pattern as depicted in Figure 63. This situation can arise when the antenna undergoes pronounced one-sided oscillations with respect to the optimal oritentation and hence never crosses the optimal orientation. This can lead to extreme non-linearities and discontinuities in RSSI fluctuations making it difficult to model such behaviors. Due to challenges in using Gain-Angle relationship (described in Section 7.2), modeling this case will not be addressed within this thesis. For the proposed model aimed at estimating antenna movements, it's imperative that the antenna passes through the optimal orientation during oscillations.

5.9 Case9: Motor Induced Oscillations with Multiple Strong Frequency Components

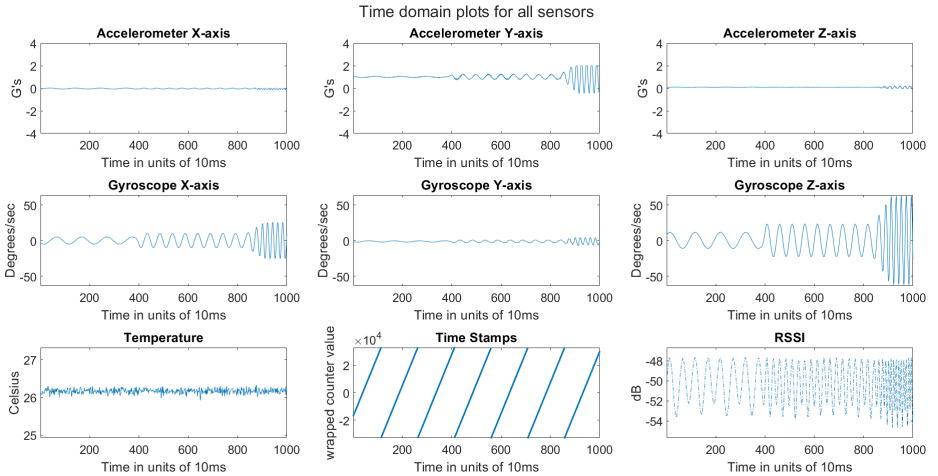

Figure 29: Sensor Data - Motor induced oscillations, 3 strong frequency components (time domain)

Figure 29 portrays an oscillation induced by a motor, featuring three pronounced frequency components. Although multiple strong frequency components can arise through motor controls, such occurrences are not typically observed in actual mast swaying behaviors due to the tendency of physical systems to converge to a resonant frequency. Furthermore, wind intensity and direction are not expected to undergo drastic changes. Due to challenges in filtering out non-essential components via IIR filtering after doubling IMU sensor data frequency (described in Section 6.1), this case will not be addressed within this thesis. The proposed model for estimating antenna movements relies on oscillations characterized by a single dominant frequency component and is designed to tolerate multiple weaker frequency components.

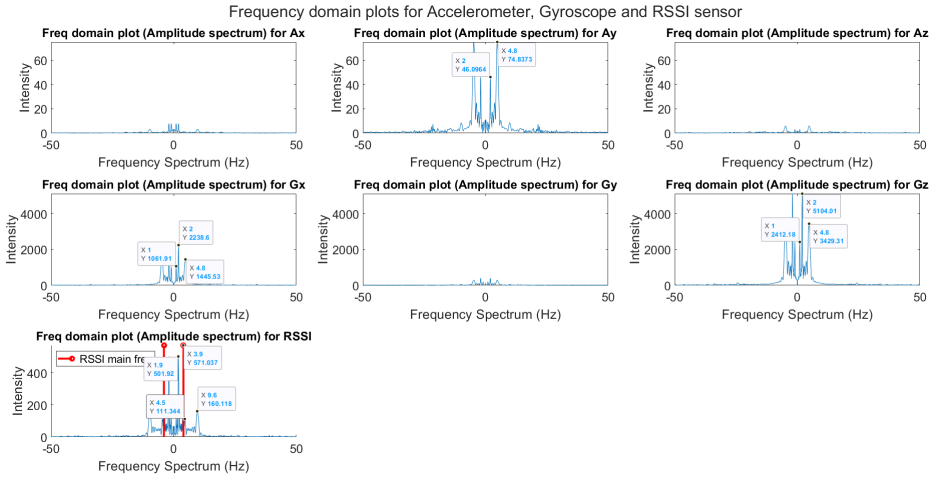

Figure 30: Sensor Data - Motor induced oscillations, 3 strong frequency components (frequency domain)

In the context of mast swaying behaviors, the presence of multiple robust frequency components is not observed and presents a complex challenge for accurate modeling.

5.10 Summary of the Presented Scenarios

The nine cases previously discussed offer a concise overview of the potential RSSI signal patterns when exposing the antenna-radio system to mast sway behavior. Through in-depth time and frequency domain analyses of various oscillation types, valuable properties have been identified such as peak frequency components, bias errors, relationships between RSSI and IMU sensor frequency components, filtering requirements, and more.

Oscillation types characterized as balanced, almost-balanced, partially-balanced, and almost-unbalanced oscillations have been considered as potential cases for constructing the estimation model. Frequency components ranging from 0.5 Hz to 5 Hz for IMU data and from 0.5 Hz to 10 Hz for RSSI data are regarded as valid frequency ranges observed in mast swaying scenarios. Bias error and variance are critical parameters in our model and can be estimated from stationary data. While we have covered certain challenging scenarios (null crossing, multiple strong frequency componenets, and unbalanced oscillation) for educational purposes, these scenarios will not be included in the construction of the final model.

6 Correlation Between the Gyroscope and RSSI Sensor Value

A straightforward approach to validate the relationship between antenna movements and RSSI fluctuations is to examine the (cross-)correlation between signals representing antenna motion and the RSSI signal value. As explained earlier, the dominant frequency component in the RSSI signal can range from the frequency of gyroscope/accelerometer oscillations (unbalanced oscillation) to twice the frequency (balanced oscillation). When the oscillation frequencies of two signals are similar, their cross-correlation result will exhibit a strong peak. Conversely, if two signals have frequencies such that the higher frequency is an exact integer multiple of the lower frequency, then the two signals are orthogonal. For such signals, the cross-correlation result will be close to zero[9]. To address the challenge of dealing with orthogonal frequencies, a solution involves upconverting the sensor frequencies before conducting the cross-correlation analysis against RSSI. To achieve this, a simple technique of doubling[10] the gyroscope/accelerometer frequency is employed, as elaborated in Section 6.1.

Signal filtering will be necessary to reduce high-frequency signal components and very low-frequency signal components that don't hold much significance. IIR filter was used and its design is described in Section 6.2. Filtering will help achieve better cross-correlation results, with multiple cases described in Section 6.3. Since the oscillation type can vary between a balance oscillation and an unbalanced oscillation, performing cross-correlation on two datasets will be necessary. The first dataset is the cross-correlation of the original IMU sensor data (gyroscope and accelerometer) with the RSSI data; and the other is the cross-correlation after performing frequency shift on the IMU data. The best of both results (highest cross-correlation value) can be concluded as the final cross-correlation value.

The section is concluded by plotting results for the IMU data collected over the entire day (or most of the day). Two cases are covered - one without motor induced oscillation and one with motor induced oscillation.

[9]This property is leveraged in Orthogonal Frequency Division Multiplexing (OFDM), a modulation scheme utilized in 4G and 5G cellular systems [24].

[10]Doubling the frequency implies shifting all the frequency components to double the frequency value, and not doubling the intensity of each frequency component.

6.1 Doubling IMU Sensor Data Frequency

Let us describe a signal characterized by sinusoidal properties, serving as a representation of oscillations. This signal embodies one predominant frequency component of significant strength, accompanied by a handful of weaker components. In totality, this signal encompasses N distinct frequency components, contributing to its overall dynamic behavior.

$$S(t) = \sum_{i=1}^{N} A_i \sin(2\pi f_i t + \phi_i) + n(t)$$

where $n(t)$ is Additive White Gaussian Noise (AWGN) noise

f_i is frequency of the i^{th} component

ϕ_i is the phase of the signal at $t = 0$ for frequency component i

$A_1 >> A_2 > A_3 \ \cdots \ A_{N-1} > A_N$ (components are listed in decreasing order of strength)

Due to the discrete nature of signal processing in discrete time, our capabilities are confined by the resolution determined by the sampling rate. Consequently, when performing DFT, there could be a minor discrepancy between the frequency components that can be measured and the true value of the frequency components. To address this, the frequency component value f_i is redefined, as outlined in the next equation, by expressing it as the sum of the measurable frequency F_i and the deviation from the true value, which is denoted as δf_i. This revision captures the nuanced relationship between the measurable components and the true frequency values, accounting for the limitations imposed by the discrete time framework and sampling rate.

$$S(t) = \sum_{i=1}^{N} A_i \sin(2\pi(F_i + \delta f_i)t + \phi_i) + n(t)$$

where $f_i = F_i + \delta f_i$

Given that the frequency F_1 can be ascertained through the results of Discrete Fourier Transform (DFT), it's possible to explore an approach involving multiplication of the signal with a synthesized sine wave that share the same frequency F_1.

$$
\begin{aligned}
S_{F_1}(t) &= S(t) \cdot \sin(2\pi F_1 t) \\
&= \left(\sum_{i=1}^{N} A_i \sin\left(2\pi(F_i + \delta f_i)t + \phi_i\right) + n(t) \right) \cdot \sin(2\pi F_1 t)
\end{aligned}
$$

Using simple trignometry equations [11],

$$
\begin{aligned}
S_{F_1}(t) = \;& \left.\begin{aligned}
&\frac{A_1}{2}\cos(2\pi(2 \cdot F_1 + \delta f_1)t + \phi_1) \\
&+\frac{A_2}{2}\cos(2\pi(F_2 + F_1 + \delta f_2)t + \phi_2) \\
&+\frac{A_2}{2}\cos(2\pi(F_3 + F_1 + \delta f_3)t + \phi_3) \\
&+\cdots
\end{aligned}\right\} \text{shifted to higher frequency (High Freq Components)} \\
& \left.\begin{aligned}
&+\frac{A_1}{2}\cos(2\pi(\delta f_1)t + \phi_1) \\
&+\frac{A_2}{2}\cos(2\pi(F_2 - F_1 + \delta f_2)t + \phi_2) \\
&+\frac{A_2}{2}\cos(2\pi(F_3 - F_1 + \delta f_3)t + \phi_3) \\
&+\cdots
\end{aligned}\right\} \text{shifted to lower frequency (Low Freq Components)} \\
& + n(t) \cdot \sin(2\pi F_1 t)
\end{aligned}
$$

[11] $\sin(A) \cdot \sin(B) = \frac{1}{2}(\cos(A + B) + \cos(A - B))$

Our specific focus pertains to isolating the term that incorporates twice the primary frequency component ($2 \cdot F_1$ term in green). Given that A_1 is significantly larger magnitude than $A_2, A_3, \cdots, A_N$, our priority is to eliminate all terms involving A_1 except for the $2 \cdot F_1$ component. There exist another term featuring a frequency close to zero (δf_1 term in red). Employing a high-pass filter allows us to effectively eliminate this term.

Furthermore, to curtail the impact of the remaining components, filtering strategies can be employed to remove frequencies exceeding 10 Hz and those below 1 Hz. However, it's important to acknowledge that complete elimination of all non-relevant components is unfeasible, as the signal amplitude attenuation from filtering cannot be $-\infty$. Consequently, this prompts the consideration of adopting a cross-correlation threshold below 1, a topic that will be explored in greater detail in subsequent sections.

The proposed method is inspired from the working principle of the superheterodyne receiver [25] used in radio systems. While delving into the matter of filter selection, the potential viability of both Infinite Impulse Response (IIR) and Finite Impulse Response (FIR) filters are assessed. This analysis is elaborated upon in the forthcoming section, providing insights into the optimal filtering approach for our context.

6.2 IIR Filter Design

IIR filters possess the capacity to offer sharp and narrow transition region surrounding the cutoff frequency; lower ripples in the pass band and/or stop band and with less complexity (lower number of filter coefficients/taps). However the primary drawback associated with IIR filters is the introduction of non-linear phase distortion. This manifests as a situation where individual frequency components may experience different phase shifts after filtering. Conversely, FIR filter requires a lot more taps (higher complexity) to achieve the same sharp transition region but suffers from higher ripples at the pass and stop band. FIR filters, in contrast, do not introduce non-linear phase distortion. This implies that each frequency component undergoes a uniform phase shift after the filtering process.

To recapitulate the challenge at hand, the received sensor data within a 10-second window is characterized by a singular dominant frequency component. The objective is to ascertain the peak cross-correlation value between this frequency component and the RSSI data. Notably, the phase of the signal does not exert any influence on the peak cross-correlation value. In light of this, an IIR filter has been chosen as the preferred filter type, as it serves to reduce extraneous frequency components that are not of interest. The characteristics of an IIR filter are primarily defined by the placement of its poles and zeros. In MATLAB, these values are determined using parameters such as the cutoff frequency and other relevant factors, which will be discussed in greater detail on the following page.

Despite the filtering process, a handful of unwanted frequency components with low intensity persist in the signal. Unfortunately, these components cannot be reduced due to the specified frequency region of interest falling between 1 Hz and 10 Hz. However, it remains feasible to effectively reduce the impact of low-frequency components that are below 1 Hz and those exceeding 10 Hz through appropriate filtering strategies.

The Chebyshev Type II filter was chosen based on its optimal balance between passband flatness and the ability to achieve a sharp transition from the passband to the stopband. This performance comparison was made against other widely used IIR filters, including Chebyshev Type I, Butterworth, and Elliptic filters. A sample comparative plot is presented in Figure 31. Figure 32 illustrates the frequency response of the IIR filter utilized in this context.

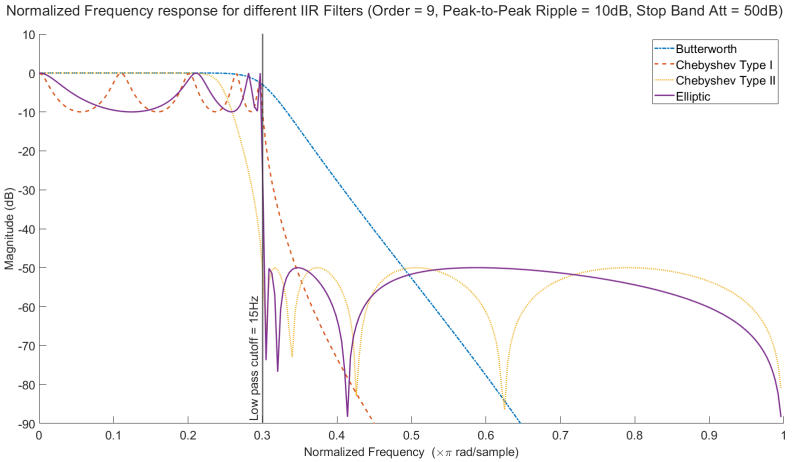

Figure 31: Comparing filter responses for different filter types

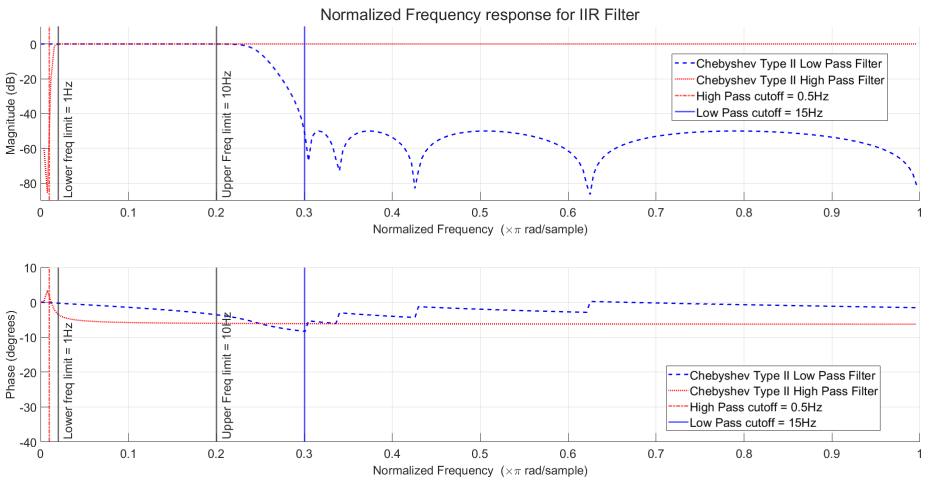

Figure 32: IIR filter response

A combination of low-pass and high-pass filter is employed as part of the filtering process. This filtering step is applied after the cross-correlation process and serves to reduce undesired frequency components from the data.

Filter Configuration (Filter 1):

- Filter type : Low pass filter
- IIR type : Chebyshev Type II filter
- Filter order : 9
- Stopband attenutation : 50 dB
- Sampling rate : 100 Hz
- Cutoff frequency[12] : 15 Hz

Filter Configuration (Filter 2):

- Filter type : High pass filter
- IIR type : Chebyshev Type II filter
- Filter order : 7
- Stopband attenutation : 50 dB
- Sampling rate : 100 Hz
- Cutoff frequency[12]: 0.5 Hz

[12]To use *cheby2* function from MATLAB, Stopband edge frequency W_s needs to be provided, which equates to 2/Sampling rate × Cutoff frequency

6.3 Cross Correlation Results

To verify the correctness of the filter design and threshold criteria, a few cases of real measurement data are covered in subsequent subsections. For all the cases, the following data/results are provided

- Original IMU sensor data and RSSI measurements
- Frequency domain filtering results for gyroscope Z-axis sensor data (strongest sensor data)
- Time domain filtering results for all sensor and RSSI data
- Cross-correlation results between RSSI and all IMU sensor data without frequency doubling.
- Cross-correlation results between RSSI and all IMU sensor data after frequency doubling.
- Conclusion

Cross-correlation between two signals $f(n)$ and $g(n)$ in discrete domain :

$$h(n) = f(n) * g(n) = \sum_{i=-\infty}^{+\infty} f(i)g(i-n)$$

Two types of cross-correlation methods are employed: one is the standard cross-correlation method as described by the formula listed above, and the other is a normalized version. In the normalized version, the result obtained above is divided by the maximum absolute value of $h(n)$ to ensure that the maximum absolute value does not exceed 1. In this section, we employ normalized cross-correlation, whereas in Section 7.6, we utilize the standard cross-correlation method.

To address the presence of other non-relevant frequency components that cannot be easily filtered out, a normalized correlation threshold of 0.7 has been chosen. If the normalized cross-correlation results for either the original sensor data or the frequency doubled data indicate a value above 0.7 for even one of the sensor outputs, the corresponding dataset is flagged as having a strong correlation between RSSI variations and the antenna-radio system movements. In the event of strong cross-correlation, it becomes less likely that the observed RSSI variations are due to other factors such as issues with power control, obstructions in the LoS path, malfunctioning receivers, and so on. The last two subsection (6.3.2, 6.3.2) contains cross-correlation results for the entire day.

6.3.1 Single Session Logs - 10 Seconds Each

Case1 : Partially Balance oscillation with bad jitter

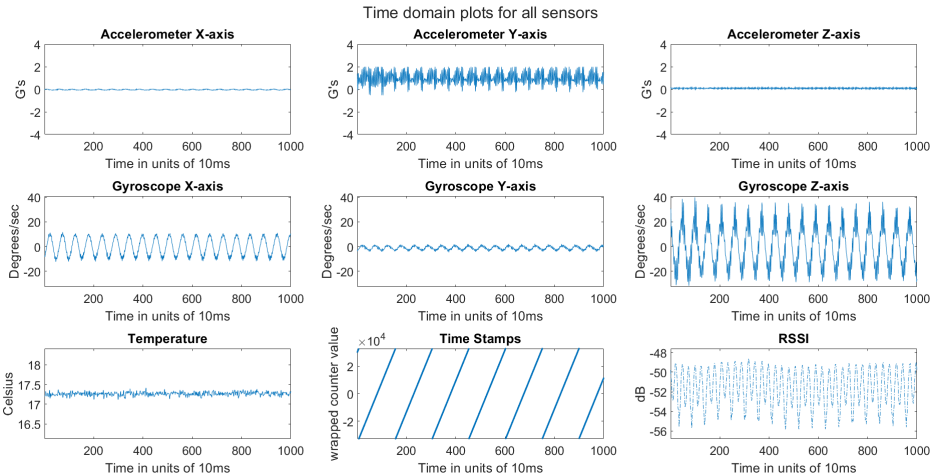

Figure 33: Case1 - All sensor plots with bad jitter

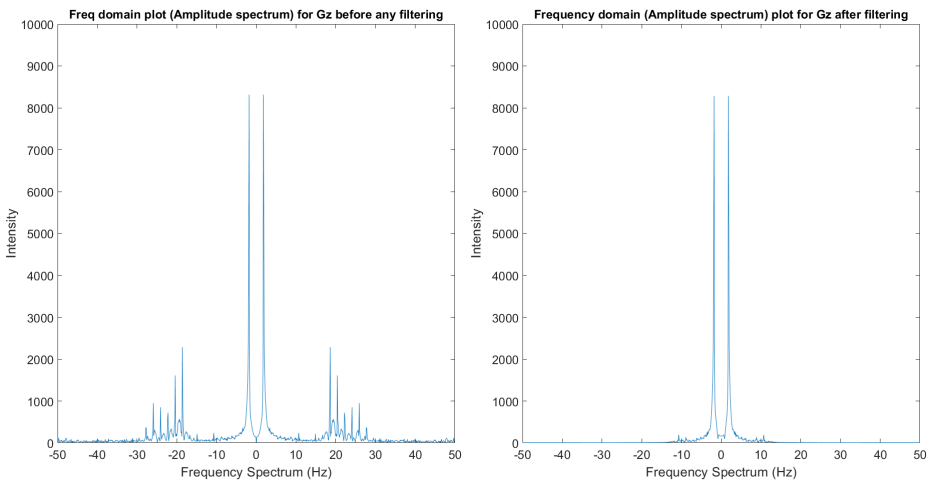

Figure 34: Case1 - IIR filtering results for sensor gyroscope Z-axis

As depicted in the right plot of Figure 34, it's evident that all frequency components exceeding 10 Hz have been substantially attenuated due to IIR filtering.

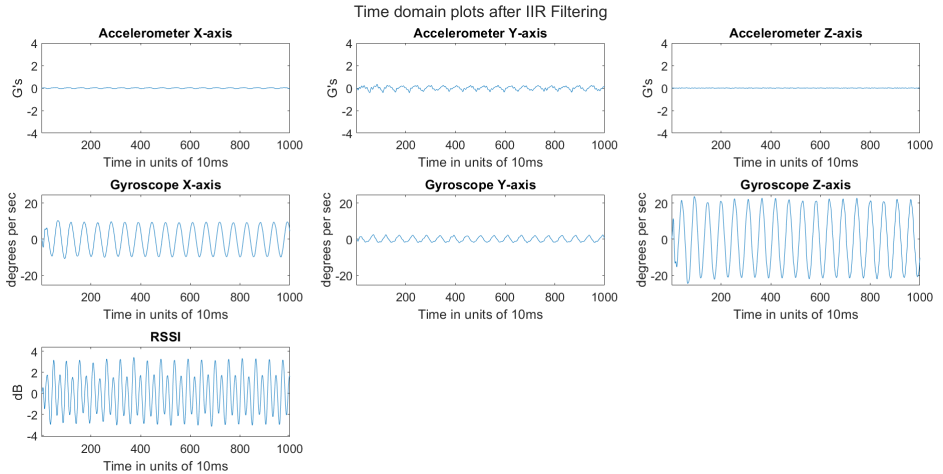

Figure 35: Case1 - All sensor plots after IIR filtering

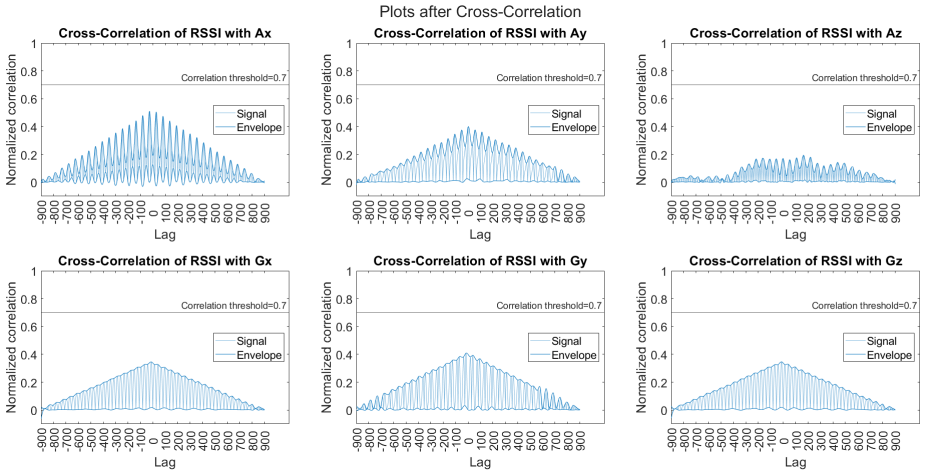

Figure 36: Case1 - Cross-correlation results after IIR filtering

Because of the characteristics of partially balanced oscillations, which lead to the presence of two prominent frequency components—one matching the gyroscope frequency and the other being twice the gyroscope frequency—it is noticeable that the energy associated with the RSSI frequency component, corresponding to the gyroscope frequency, is relatively diminished, resulting in lower cross-correlation peaks. This observation is exemplified in Figure 36, where none of the cross-correlation results surpass 0.7.

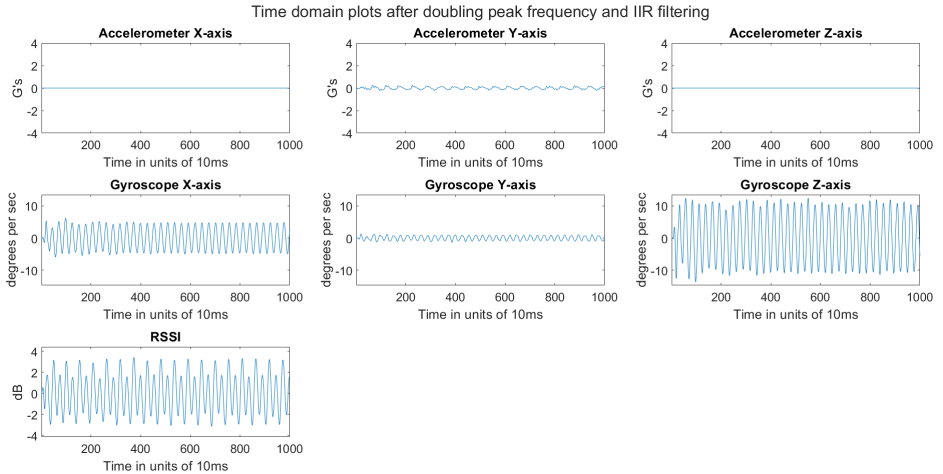

Figure 37: Case1 - All sensor plots after peak frequency doubling and IIR filtering

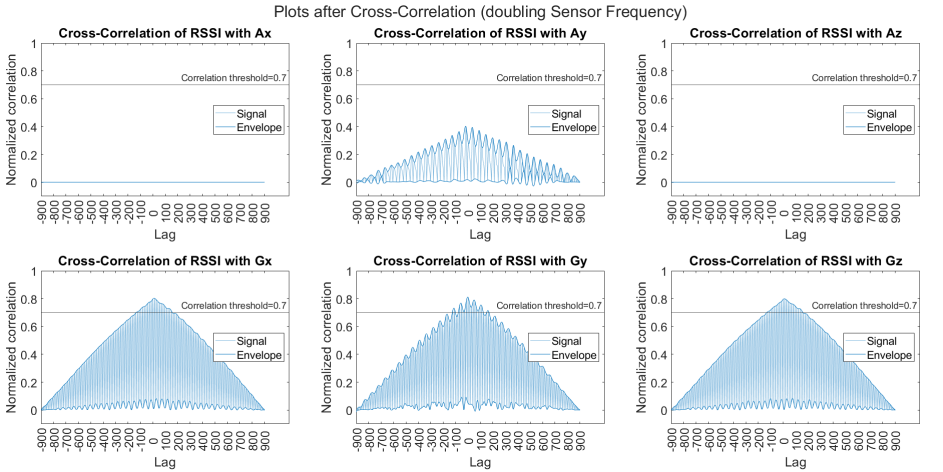

Figure 38: Case1 - Cross-correlation results after peak frequency doubling and IIR filtering

Conclusion : Upon doubling the frequency component of the sensor data before conducting cross-correlation, the gyroscope X-axis, gyroscope Y-axis, and gyroscope Z-axis datasets all meet the established threshold of 0.7, as visualized in Figure 38. This observation strongly suggests that fluctuations in RSSI exhibit a robust correlation with variations in the gyroscope, underscoring a significant relationship between RSSI fluctuations and antenna movements.

Case2 : Balanced Oscillation with Short Deep Fade

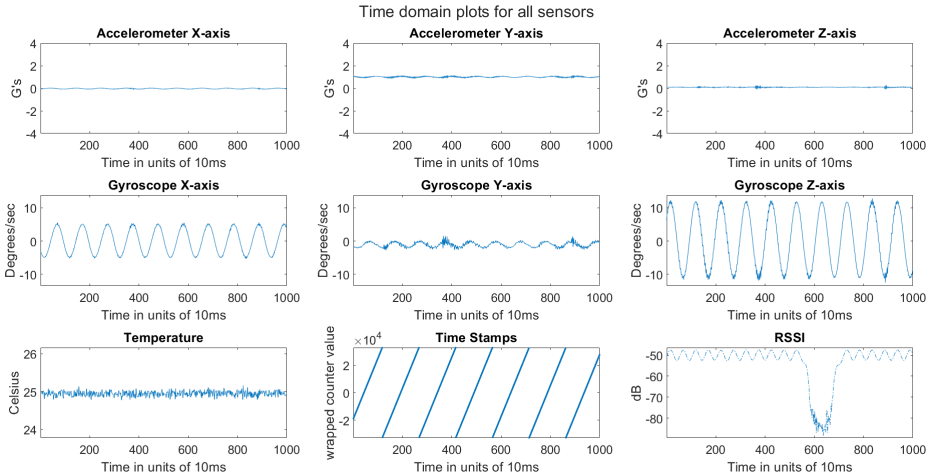

Figure 39: Case2 - All sensor plots with deep fade

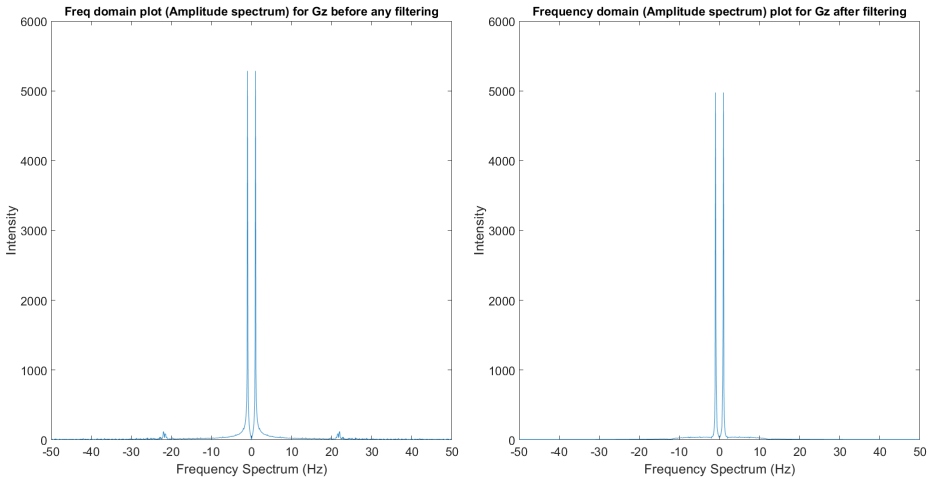

Figure 40: Case2 - IIR filtering results for sensor gyroscope Z-axis

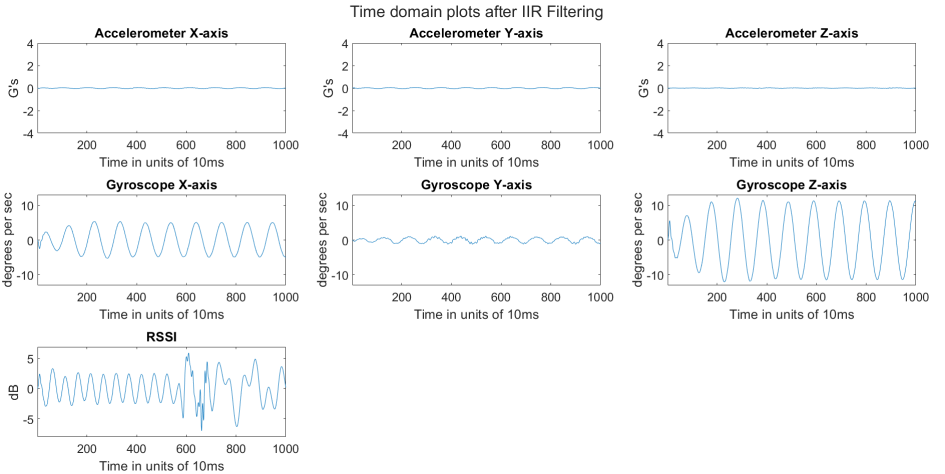

Figure 41: Case2 - All sensor plots after IIR filtering

There is distortion present in the oscillation pattern within the RSSI subplot in Figure 41 following the application of IIR filtering. This distortion subsequently leads to unsatisfactory cross-correlation results, as evidenced in Figure 42. A similar observation can be made when doubling the peak frequency of the IMU sensor data, as illustrated in Figure 44. This instance serves as an example of suboptimal correlation between the RSSI fluctuations and IMU sensor data.

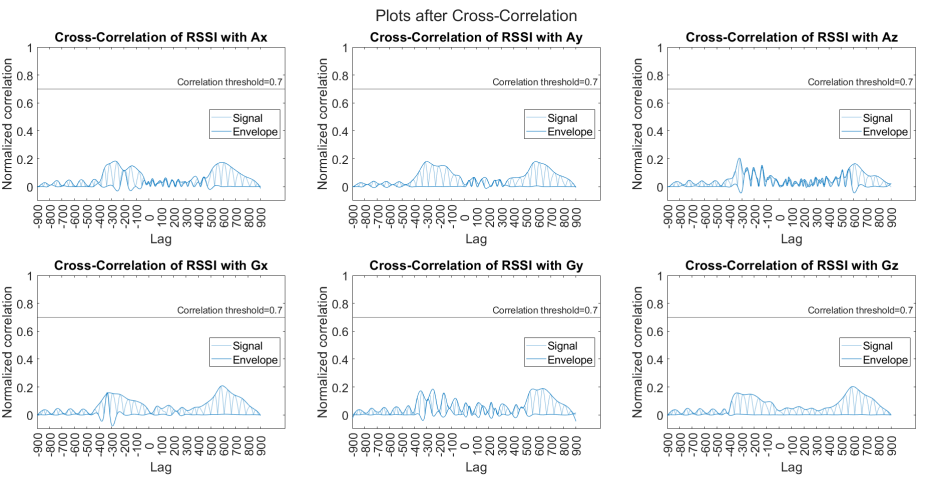

Figure 42: Case2 - Cross-correlation results after IIR filtering

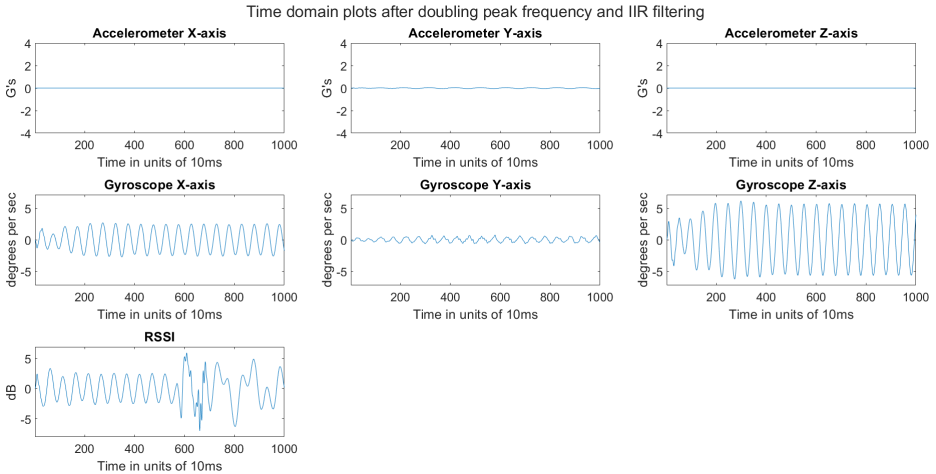

Figure 43: Case2 - All sensor plots after peak frequency doubling and IIR filtering

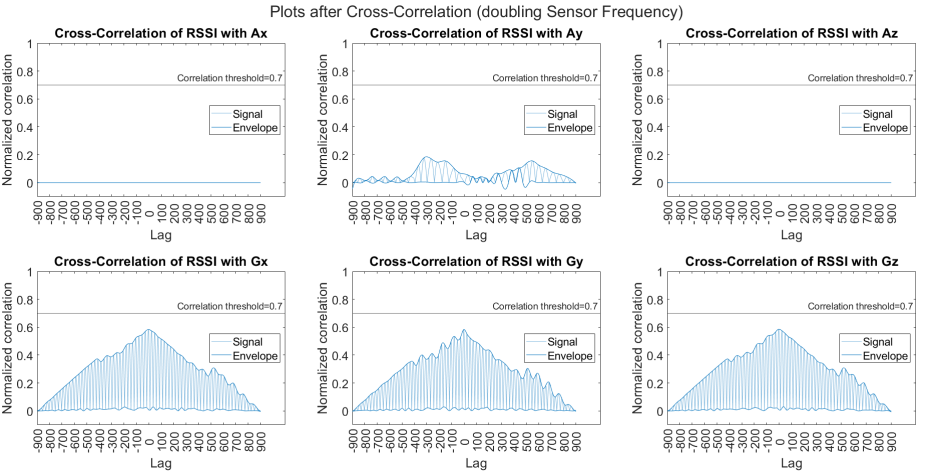

Figure 44: Case2 - Cross-correlation results after peak frequency doubling and IIR filtering

Conclusion: None of the sensors meet the cross-correlation threshold (0.7), which is expected due to the deep fade impacting the RSSI measurements. If deep fade didn't occur, the cross-correlation peak would likely be around 0.9.

Case3 : Almost Unbalanced Oscillation

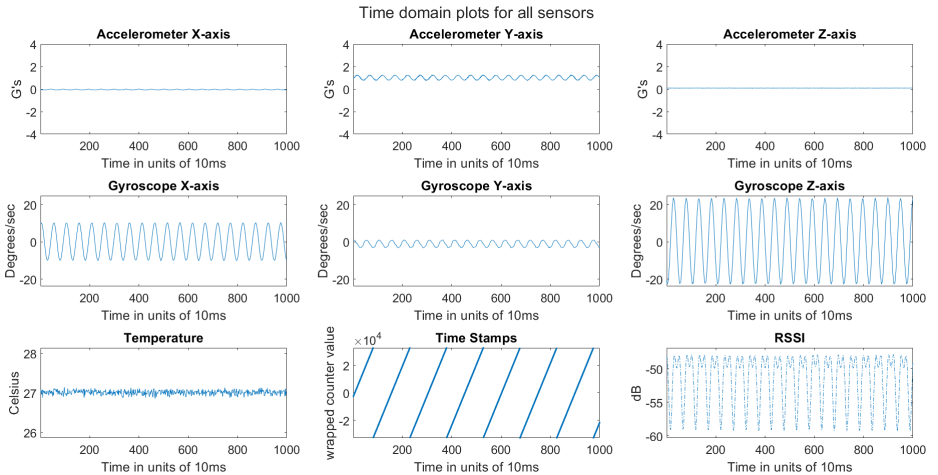

Figure 45: Case3 - All sensor plots with unbalanced case

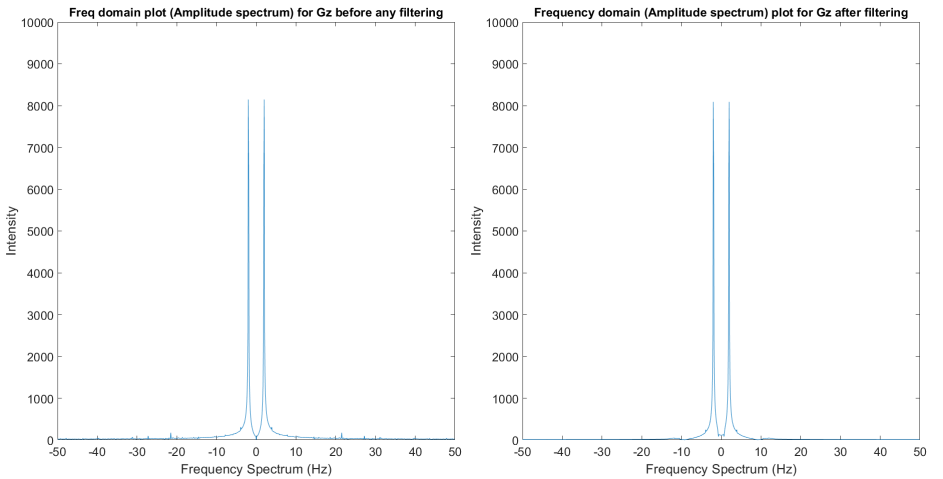

Figure 46: Case3 - IIR filtering results for sensor gyroscope Z-axis

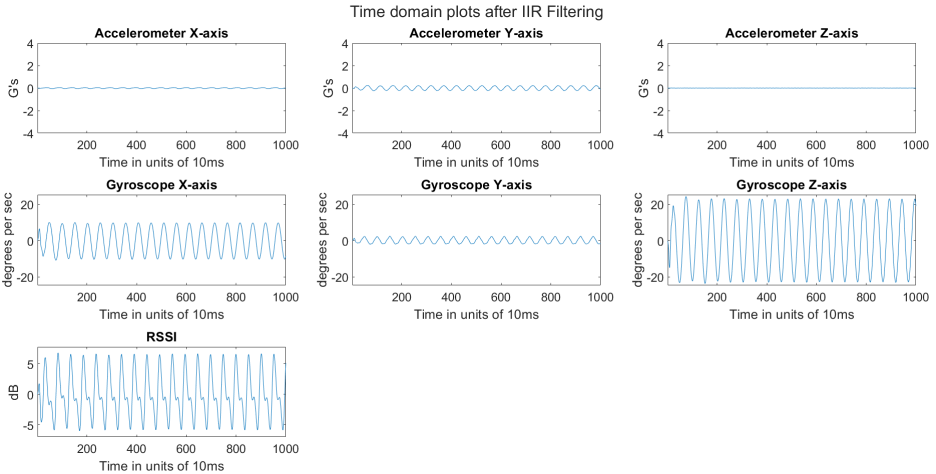

Figure 47: Case3 - All sensor plots after IIR filtering

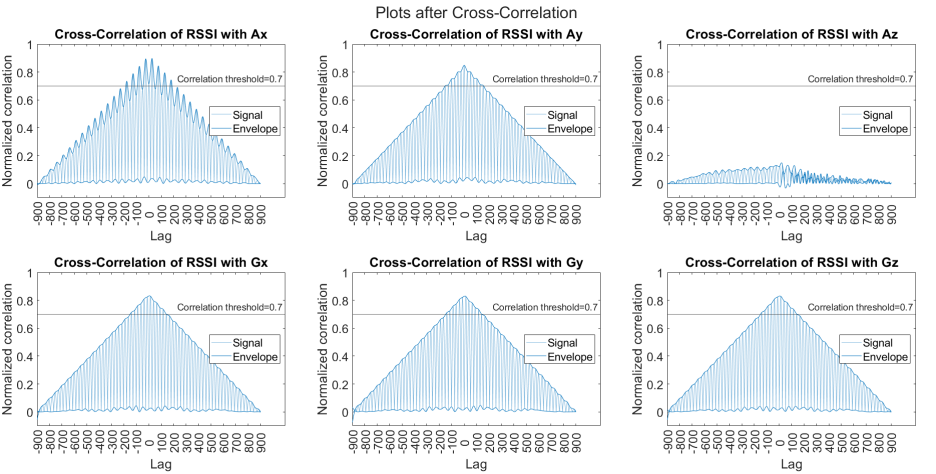

Figure 48: Case3 - Cross-correlation results after IIR filtering

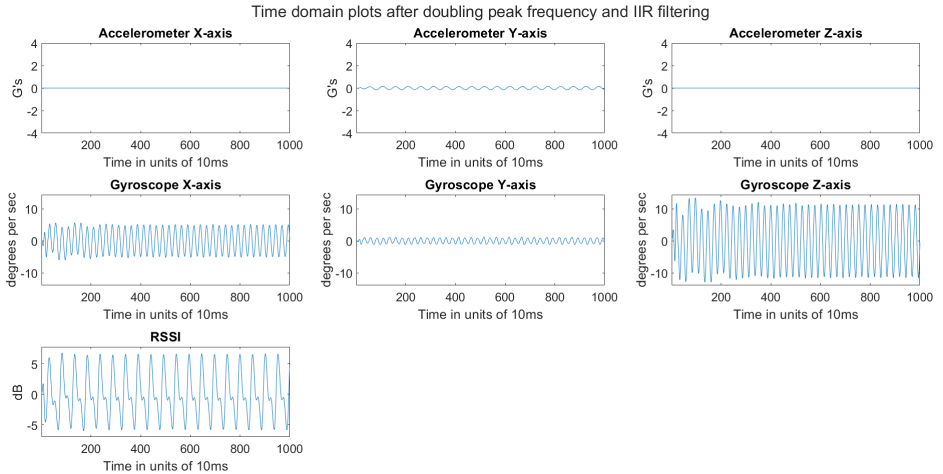

Figure 49: Case3 - All sensor plots after peak frequency doubling and IIR filtering

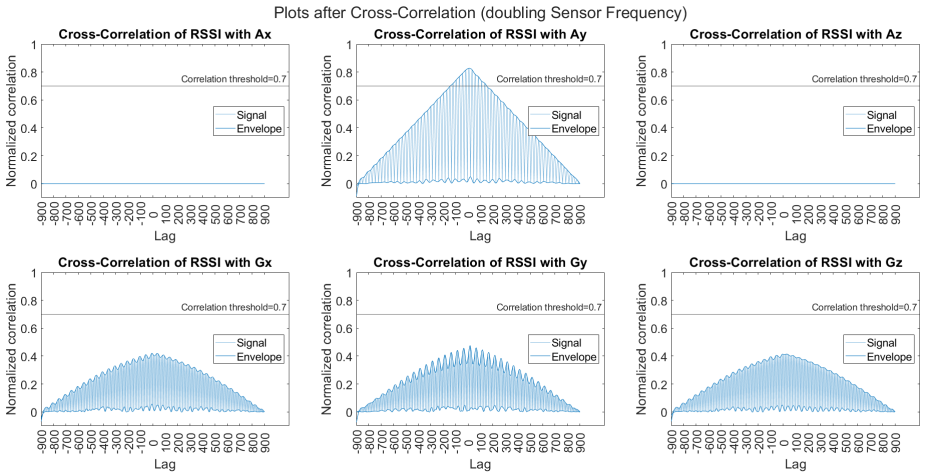

Figure 50: Case3 - Cross-correlation results after peak frequency doubling and IIR filtering

Conclusion : Since the RSSI oscillation was almost one-sided (almost unbalanced), there are significant cross-correlation result exceeding the threshold of 0.7 without the need for frequency doubling, as shown in Figure 48.

6.3.2 All Day Cross-Correlation Plots

To validate the accuracy of the proposed methods for identifying strong correlations between RSSI variations and movements, two daily plots are summarized in the following subsections. Each plot instance in the sensor data plot represents an approximate minimum and maximum value derived from a 10-second log, as opposed to each sensor sample instance every 10 ms in the previous plots. Given the inherent variance in sensor data and the presence of outliers, it becomes necessary to mitigate these issues. This is achieved through a moving average process (for the variance issue) and mean of the maximas/minimas (for outliers). The calculation of the optimal window size for the moving average process is explained in Appendix H. Additionally, we calculate the mean of five local maximas and minimas from each 10-second log. The rationale behind selecting five points is that, for a minimum oscillation frequency of 0.5 Hz, there will be at least five local maxima or minima in a 10-second window. For higher frequencies ($>$ 0.5 Hz and $<$ 10 Hz), there will be an increased occurrence of local maxima and minima, ensuring the averaging technique is still applicable.

The cross-correlation plots display the maximum cross-correlation value observed between the RSSI and each of the IMU sensors (gyroscope/accelerometer). In each plot instance, a single value represents the maximum cross-correlation result for each sensor and axis obtained from a 10-second log. A total of 6 different values are plotted for each plot instance, namely accelerometer X-axis, accelerometer Y-axis, accelerometer Z-axis, gyroscope X-axis, gyroscope Y-axis and gyroscope Z-axis. A cross-correlation value exceeding 0.7 indicates a strong cross-correlation between the RSSI variations and the antenna movements. To simplify the evaluation criterion, a single peak cross-correlation value obtained from both the accelerometer and gyroscope sensors, considering all available axes, is considered and compare against the threshold of 0.7.

By rescaling the data on the time axis, it becomes possible to visualize the entire day's data within a single plot window. This approach facilitates the assessment of the mast system's reliability throughout the day.

Case1 : No motor induced oscillation

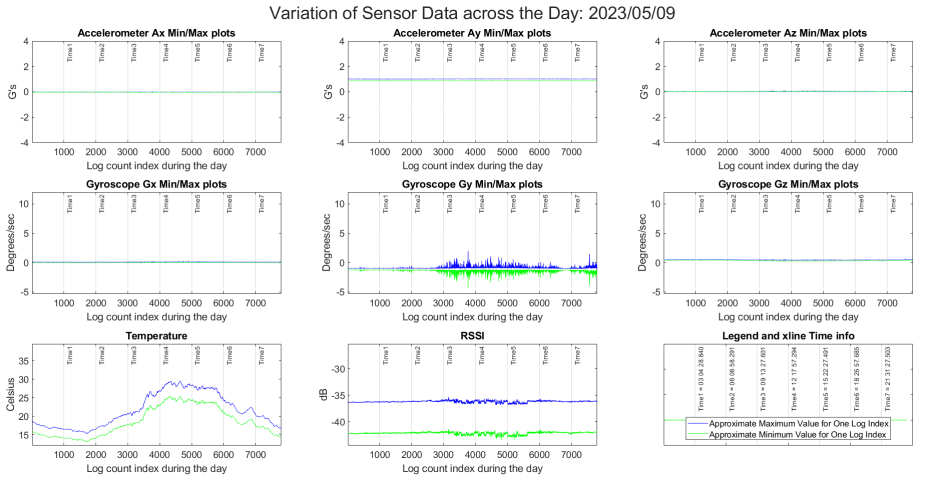

Figure 51: Sensor info - No motor induced oscillation

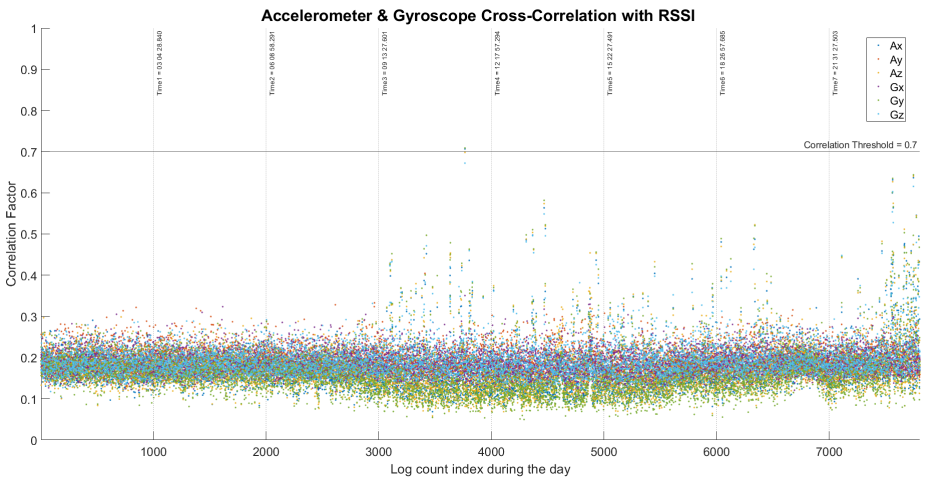

Figure 52: Correlation without frequency doubling - No motor induced oscillation

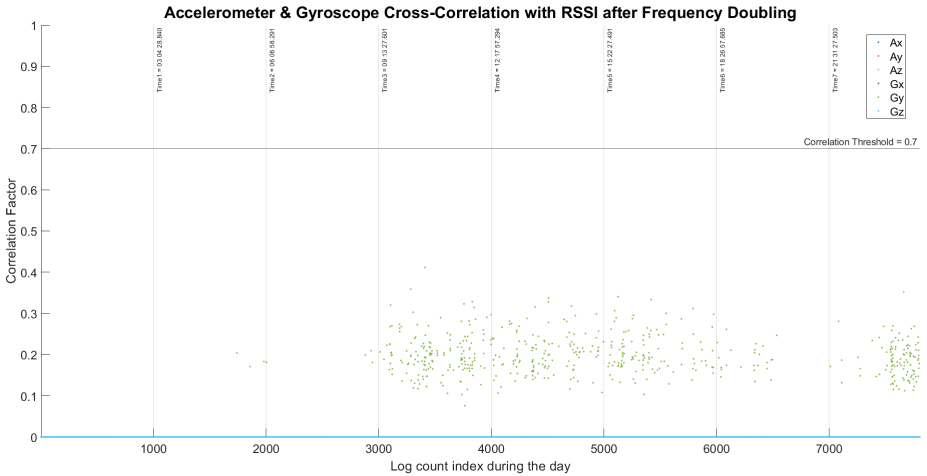

Figure 53: Correlation with frequency doubling - No motor induced oscillation

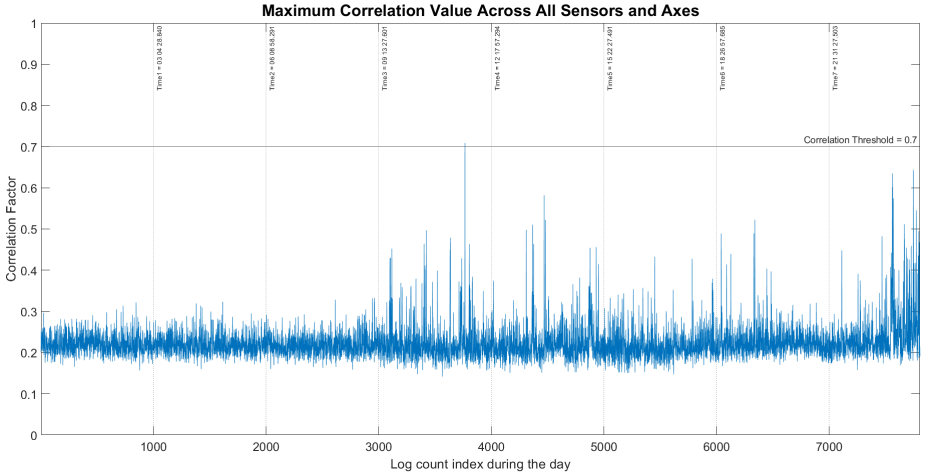

Figure 54: Maximum correlation considering all sensors and axes - No motor induced oscillation

As expected, there is poor correlation between the IMU sensor data and RSSI data in both results (with and without frequency doubling), except for one instance in Figure 54 (a single point in the plot that crosses 0.7 correlation factor at around log count index 3800). This isolated correlation could be due to potentially strong wind that induced minor oscillation on the gyroscope Y-axis, which happened to correlate well with the one-sided RSSI oscillation.

Case2 : Motor induced oscillation

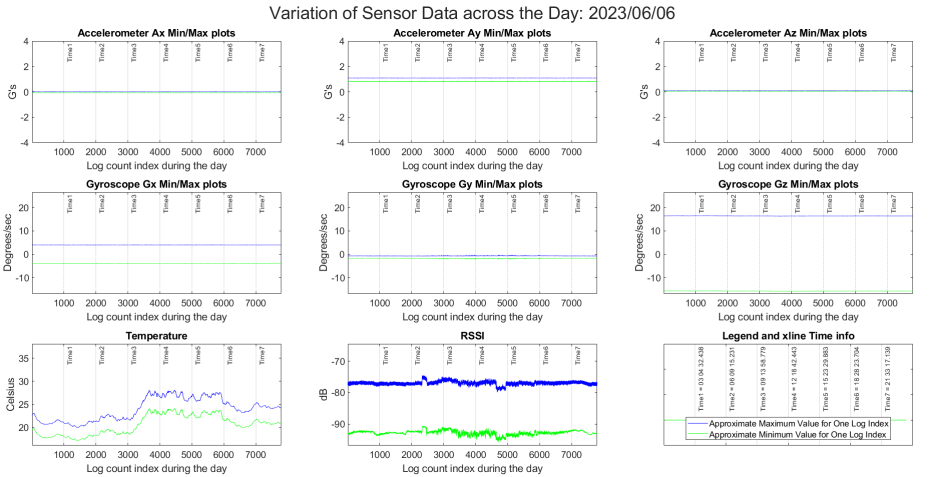

Figure 55: Sensor info - Motor induced oscillation

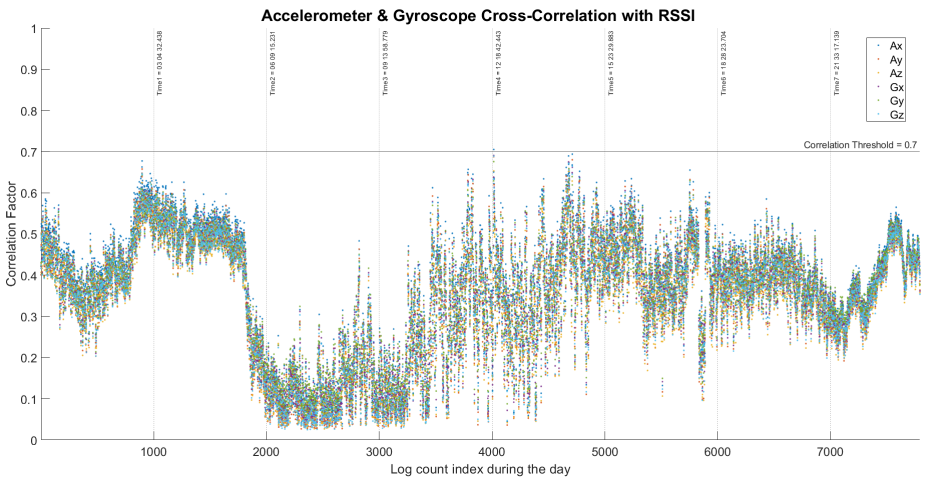

Figure 56: Correlation without frequency doubling - Motor induced oscillation

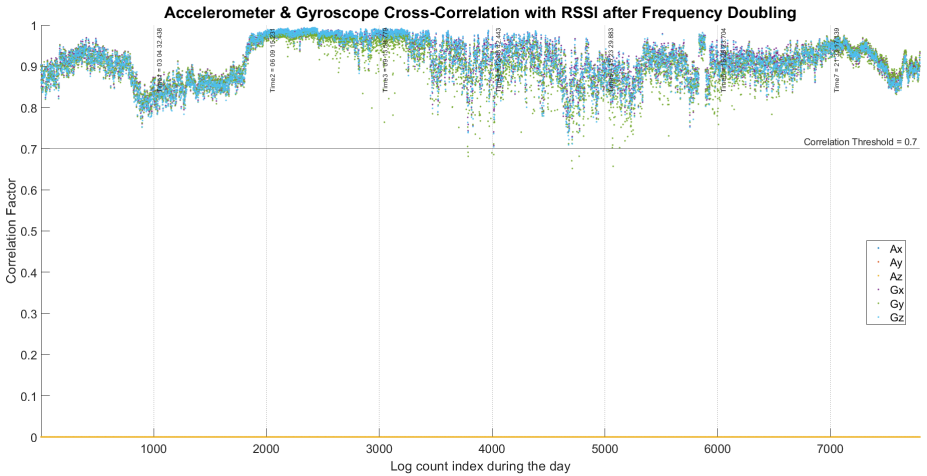

Figure 57: Correlation with frequency doubling - Motor induced oscillation

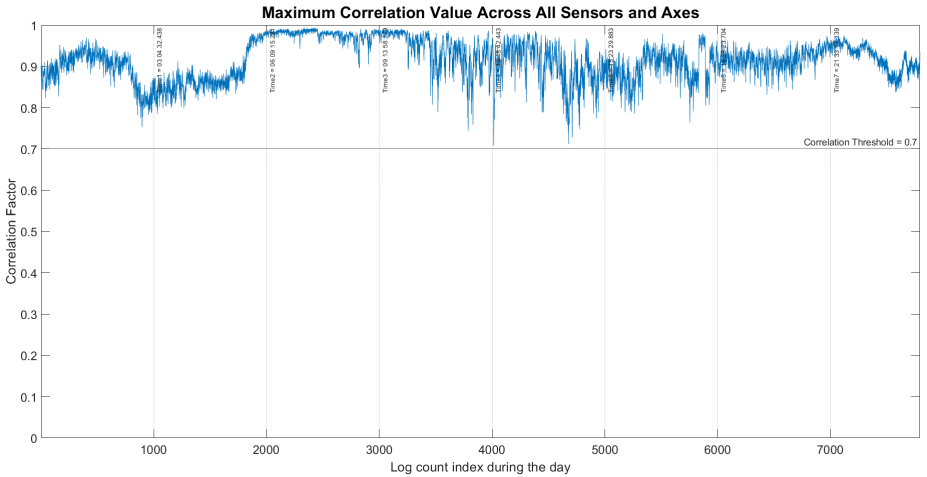

Figure 58: Maximum correlation considering all sensors and axes - Motor induced oscillation

As anticipated, a strong correlation between the RSSI and IMU data can be observed for most instances throughout the day, as shown in Figure 58.

7 Kalman Filter Model

Having discussed the basic correlation properties between RSSI data and IMU sensor data, this section will focus on constructing a model to predict the antenna deviation from its optimal alignment. The ability to anticipate deviations from the peak enables the implementation of corrective measures aimed at minimizing the adverse effects of antenna movements on the reliability of data transmission (Section 9). Due to the intricate nature of the problem at hand, it is essential to employ certain approximations and assumptions to simplify its complexity and facilitate a solution.

The unknown system properties can be summarized as follows:

- Relative frame of reference between the antenna and the IMU on the radio
- Type of movement/mast swaying
- Weather impacts to the signal strength (RSSI)
- Adaptive Power Control (APC) settings
- Degree of rotation for linearly polarized wave

The desired goal is to estimate the deviations of the antenna orientation from optimal alignment, considering both the horizontal and vertical axes independently. However, the limitation lies in having only a single RSSI value, rendering the system underdetermined [26] (the number of equations is less than the number of unknowns). As a workaround, the problem is redefined to ascertain a solitary alignment deviation, albeit in any direction.

The subsequent sections can be summarized as follows:

- Section 7.1 provides a concise overview of the essential approximations and prerequisites employed to streamline the complexity of the problem.
- Section 7.2 outlines the methodology of curve fitting used to establish the mathematical relationship between changes in RSSI value and deviations of the antenna from its optimal orientation.
- Section 7.3 explains the utilization of a variant of Kalman Filter, namely the Extended Kalman Filter (EKF) model to estimate the antenna's deviation from its optimal alignment. To ensure the model's effectiveness, certain parameters within the model must be estimated using historical data.
- Section 7.4 identifies several valuable features that can be derived from historical data. These features play a crucial role in identifying specific parameters within the EKF model, aiding its accuracy and performance.

- Section 7.5 explains the application of a FIR filter to eliminate high-frequency noise components, subsequently enhancing the capability to extract features from historical data.
- Section 7.6 elaborates on the process of selecting the gyroscope sensor axis that exhibits the highest cross-correlation with RSSI data.
- Section 7.7 elaborates on the filtering procedure, and outlines the synchronization technique used to align zero crossings. This synchronization aims to obtain RSSI values at the peaks of antenna oscillations.
- Section 7.8 presents the results attained from estimating deviations from peaks through illustrative examples. Additionally, it introduces a weighted average formula employed to give precedence to more recent samples over older ones, enhancing the accuracy of the estimation process.
- Section 7.9 explains the methodology utilized to determine the gyroscope scaling factor, crucial in accurately representing gyroscope values in relation to antenna oscillations.
- Section 7.10 demonstrates the outcomes of the EKF model subsequent to the incorporation of updated estimated parameters into the EKF model.

To ensure the EKF model's robustness to a variety of mast swaying types, three logs are selected that differ in both the type of oscillation and the frequency of oscillation:

- Almost-balanced oscillation, approximate oscillation frequency of 3 Hz.
- Partially-balanced oscillation, approximate oscillation frequency of 1 Hz.
- Almost-unbalanced oscillation, approximate oscillation frequency of 2 Hz.

Unfortunately, owing to the restrictions on using the mast sway generator, a significant portion of the oscillations tend to stimulate the IMU sensors in a comparable manner. Gyroscope Z-axis is always the strongest and correlates the best with RSSI data. Section 8 delves into the scenario of manually inducing mast sway with the aim of inducing motion in two distinct gyroscope axes, thereby serving as a validation of the model's performance.

7.1 Approximations and System Requirements

Several approximations and requirements have been put forth to address the intricate task of developing a model capable of accurately estimating antenna movements across a range of antenna-radio configurations, as well as various scenarios involving mast swaying. These approximations have been carefully tailored to account for both the available equipment constraints pertinent to this thesis and the necessity for the proposed model to function within a predefined level of confidence. The subsequent sections will delve into a comprehensive breakdown of these approximations and requirements, offering a succinct overview outlined below.

Approximations:

- Floating body approximation
- Circular radiation pattern approximation

System requirements:

- Negligible impact due to antenna feed positional change
- No impact due to polarization rotation
- APC is disabled
- Antenna passes through or near the optimal orientation during oscillations
- Antenna oscllates only within radiation pattern main lobe limits
- Negligible small-scale fading
- No shadow fading but possibility of a short deep fade
- Model tolerance against precipitation based fading
- Antenna-radio system experiences movements around a single focal point at any given time
- Antenna movement on either the transmitter or the receiver side of the communication link

All the requirements mentioned above, except for the last one, are well within reasonable expectations.

7.1.1 Unknown Focal Point

As explained in Section 2.2, even in the case of a rigid body, multiple potential motions arise from movements around distinct focal points. All the motions detailed can be deconstructed as a combination of pure antenna rotation (alteration in antenna orientation) and lateral movement of the receiving point in space (changes in antenna feed position). Both these types of motions are illustrated in Figure 59.

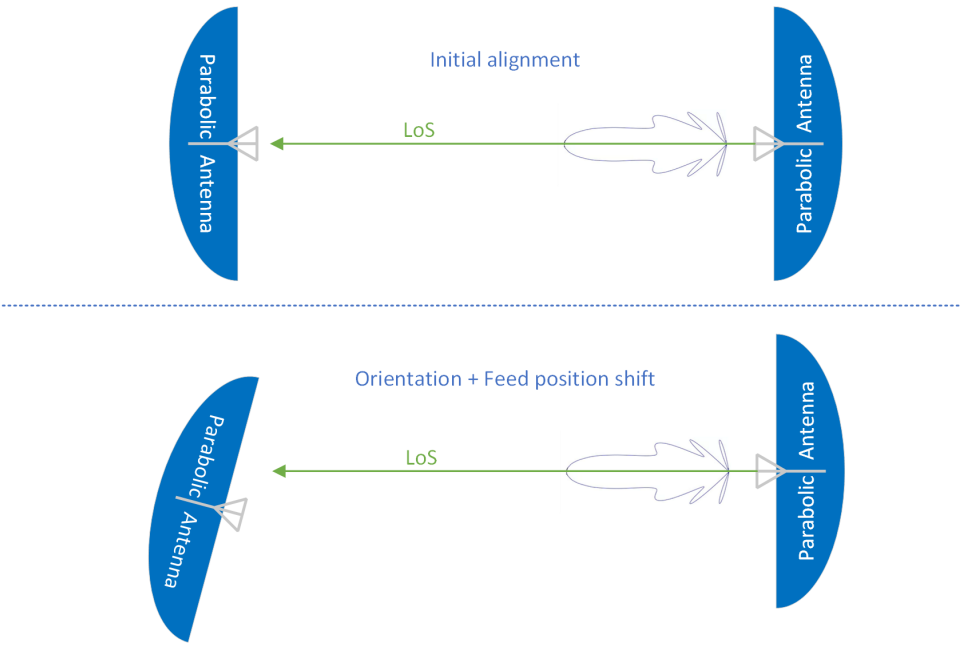

Figure 59: Misalignment outcomes

With a few exceptions (detailed in Appendix A), a positional shift of the antenna feed do not contribute to the substantial variations in received signal strength. The RSSI variations are primarily influenced by changes in orientation, and for the purpose of simplification, all movements may be treated as pure rotational motions. This approximation is termed the "Floating body approximation" where the angular rotation of the IMU is proportional to the angular rotation of the antenna. The constraint on the relationship is the **proportionality**, and a method to estimate the constant of proportinality (K_{gyro}) is covered in Section 7.9. In the scenario where the focal point precisely lies between the IMU sensor and the antenna, and their reference frame axes are parallel, the value of K_{gyro} should be 1.

The IMU sensor supplies data regarding linear acceleration and angular velocity, serving to characterize its motion. However, owing to the absence in the knowledge about the focal point, the utilization of linear acceleration to estimate angular rotation isn't viable, since both the radius of rotation (distance from the focal point to the IMU) and the direction of rotation are essential [17]. Instead, reliance is placed on angular velocity. Despite this, it remains crucial to account for the disparity between the IMU sensor's frame and the frame of the antenna. This is precisely why the term "K_{gyro}" is introduced to address this discrepancy and factor it into the EKF model.

7.1.2 Using Gain vs Angle Model

In the context of all analyzed oscillations, a fundamental assumption is that the antenna invariably traverses through the optimal or almost optimal orientation. This assumption is crucial as it enables the utilization of the antenna radiation pattern specification to estimate the relationship elucidated in Section 7.2. Figure 60 depicts a selection of potential antenna oscillations, utilizing concentric ellipses to signify the extent of the antenna orientation deviation from the optimal alignment. Notably, the red plots represent scenarios in which the model proposed in this thesis will encounter challenges, leading to inaccurate predictions of the antenna motion. The green plots, conversely, are anticipated to function with a reasonable degree of accuracy. A state of (perfectly) unbalanced oscillation poses challenges in estimating K_{gyro} and deviation angle from optimal alignment using the proposed algorithms in this thesis. There may exist a potential solution but this scenario falls beyond the scope of the thesis. All oscillations types from almost unbalanced to balanced oscillation are within the scope of the thesis.

The concept of peak crossing isn't limited to an absolute singular point. Rather, considering the antenna's specification in Figure 62, the crossing lies within a 0.5° circular radius around the optimal orientation. This angle corresponds to a Loss < 0.1 dB, or the first non-zero attenuation row as per the specification table in Figure 62. Furthermore, owing to pronounced non-linearities and the inability to establish the Gain-Angle relationship using simple expressions, instances involving extreme oscillations where the antenna orientation aligns with null points (Figure 28) will be omitted from consideration. It is important to note that all oscillations are presumed to fall within the confines of the main lobe's boundaries.

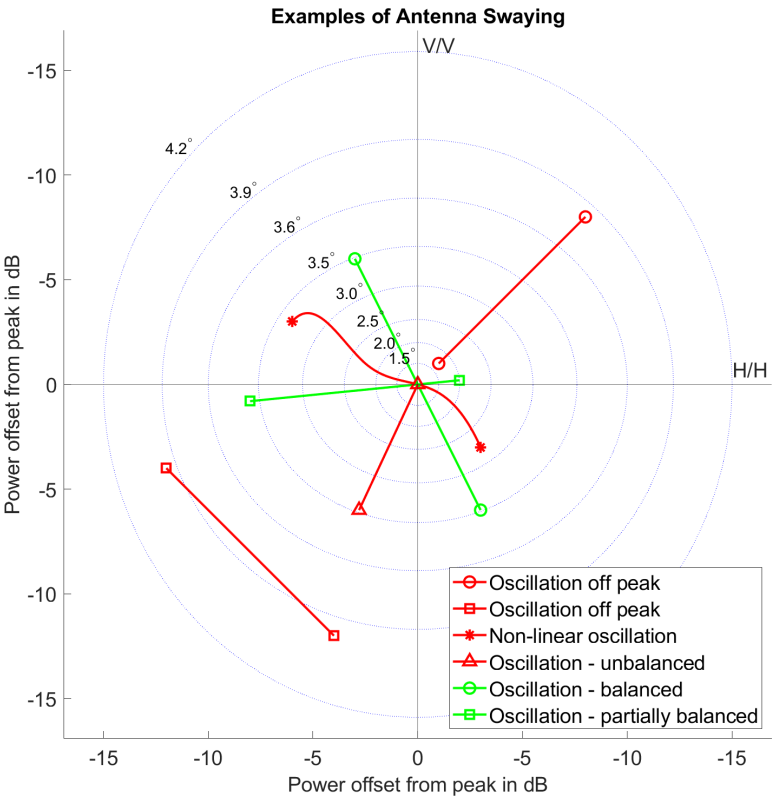

Figure 60: Various oscillation types

7.1.3 Polarization Angle Ambiguity

When an electromagnetic wave traverses a medium, a linearly polarized wave can undergoes rotation if it encounters water particles [27] or any object capable of inducing rotation. The motion described in Figure 11 induces a relative polarization rotation. Consequently, the polarization angle of the received (Rx) signal may deviate from alignment with the horizontal (H/H) or vertical (V/V) axis, as well as the polarization angle of the transmitted (Tx) signal. The provided antenna-radio system is designed to capture a single RSSI value during each sampling interval, aligned with the polarization angle. As a result, regardless of any shifts in the polarization angle during the signal's propagation from the transmitter to the receiver, the RSSI measurement will consistently correspond to the best polarization direction/angle. This situation leads to an inherent ambiguity in determining the actual polarization angle, as the RSSI value remains the same regardless of the polarization angle's variation. To effectively assess the effects of polarization rotation, it becomes necessary for the radio system to measure RSSI across two orthogonal axes. However, the current apparatus lacks this capability. It is recommended to consider the implications of polarization rotation, particularly when implementing XPIC. Addressing the consequences of polarization rotation lies beyond the scope of this thesis.

Given the challenge posed by the inability to determine the polarization angle accurately, a pragmatic approach involves simplifying the problem by assuming identical antenna specifications for both horizontal (H/H) and vertical (V/V) polarizations. This simplification is referred to as the "circular radiation pattern approximation", in contrast to the actual antenna specification which exhibits an elliptical radiation pattern (Figure 60). To establish a mathematical correlation between the Gain and Angle (Section 7.2), the column exhibiting higher attenuation will be used to ensure a more conservative estimate. This corresponds to V/V column (Figure 63) or the vertical axis. Within the main lobe region (From Section 7.2.3, 4.2°), the maximum disparity between H/H and V/V values for the same angle remains limited to 1 dB. Although this discrepancy introduces some degree of estimation error into the final proposed model, it remains modest enough not to render the model ineffective. Furthermore, it's important to note that for small angles (Figure 63, Angle <= 2°), both V/V and H/H polarizations adhere to the same radiation pattern, enhancing the validity of the circular radiation pattern approximation.

In summary, the following observations can be drawn from the aforementioned statements: No impact due to polarization rotation and Circular radiation pattern approximation ($H/H = V/V$).

7.1.4 Missing APC Info

Adaptive Power Control (APC) is a common feature in most wireless systems, enabling adjustments in response to transmission needs and changes in channel characteristics. The methods proposed in this thesis hold applicability for systems incorporating APC, given that the transmitter's configured power is ascertainable at the receiver's end. However, the provided apparatus cannot record Tx power and APC settings simultaneously with sensor and RSSI data samples at the receiver in precise timing alignment. Consequently, during the collection of actual data, APC remains disabled. Nonetheless, if APC is configured and power adjustments due to APC are known, a simple formula can be employed to calculate the RSSI values intended for utilization within the EKF procedures (as well as cross-correlation computations outlined in the preceding section).

$$R(t) = R_{rx}(t) - \Delta R_{tx}(t) - \Delta P_{APC}(t) \tag{1}$$

R : RSSI value for EKF and Cross-correlation

R_{rx} : Measured RSSI value from the radio receiver. This is known at the receiver side for both APC and non-APC cases

ΔR_{tx} : Increase in baseband Tx power with respect to Tx power in the beginning of EKF process. This can vary due to several factors, encompassing elements such as changes in the modulation scheme, changes in signal bandwidth, changes in the multiplexed information between the data and control channels, among others [28].

ΔP_{APC} : Increase in power due to APC settings. This can vary due to several factors, such as closed-loop power control [28] and adjustments based on channel estimation, among others.

For accurate application of APC adjustments before providing the RSSI value to the EKF process, it's essential that both ΔR_{tx} and ΔP_{APC} are known at the receiver side for each individual sample instance.

7.1.5 Small Scale Fading

Small scale fading is composed of two main components: doppler spread and multipath fading [29]. Doppler spread emerges when either the transmitter or the receiver is in motion. In the context of mast swaying-induced antenna movements, the predominantly oscillatory nature and frequency (less than 5 Hz) imply that the effect of Doppler spread can be reasonably considered negligible. However, precautions are necessary to ensure that multipath fading remains minimal. This is especially crucial due to its potential to distort the antenna radiation pattern.

Directional antennas, such as the dish antenna employed in this thesis, can experience an intriguing phenomenon with multipath signals. These multipath signals, arriving at specific angles relative to the antenna, can lead to signal amplification or attenuation based on their phase in relation to the LoS signal's phase. This phenomenon, in turn, has the potential to disrupt the expected behavior of the radiation pattern, introducing inaccuracies to the proposed model. It's worth noting that the signal amplification or attenuation caused by a robust multipath is not an abrupt occurrence, but rather a gradual process influenced by the antenna's swaying motion. A useful guideline for minimizing the influence of strong multipath involves ensuring that no obstacles are present within the Fresnel Zone radius [29]. This principle aims to mitigate the impact of multipath interference and maintain signal integrity.

Because the antenna used in the thesis is not of the omnidirectional or widebeam variety, the Fresnel Zone radius calculated based on standard references may not be accurate due to its narrow beam characteristics. Despite the narrower Fresnel Zone radius, a critical requirement remains: ensuring that no obstructions are present within the immediate frontal view of the antenna, encompassing all swaying angles under analysis. As depicted in Figure 95a, even if the object isn't precisely in the LoS path, it can lead to pronounced multipath effects owing to signal diffraction around the object. To delve further into the verification of low impact from multipath on the antenna radiation pattern, refer to Appendix C for comprehensive insights.

In summary, small-scale fading can be regarded as negligible, granted that the antenna setup is carefully engineered to mitigate the influence of multipaths.

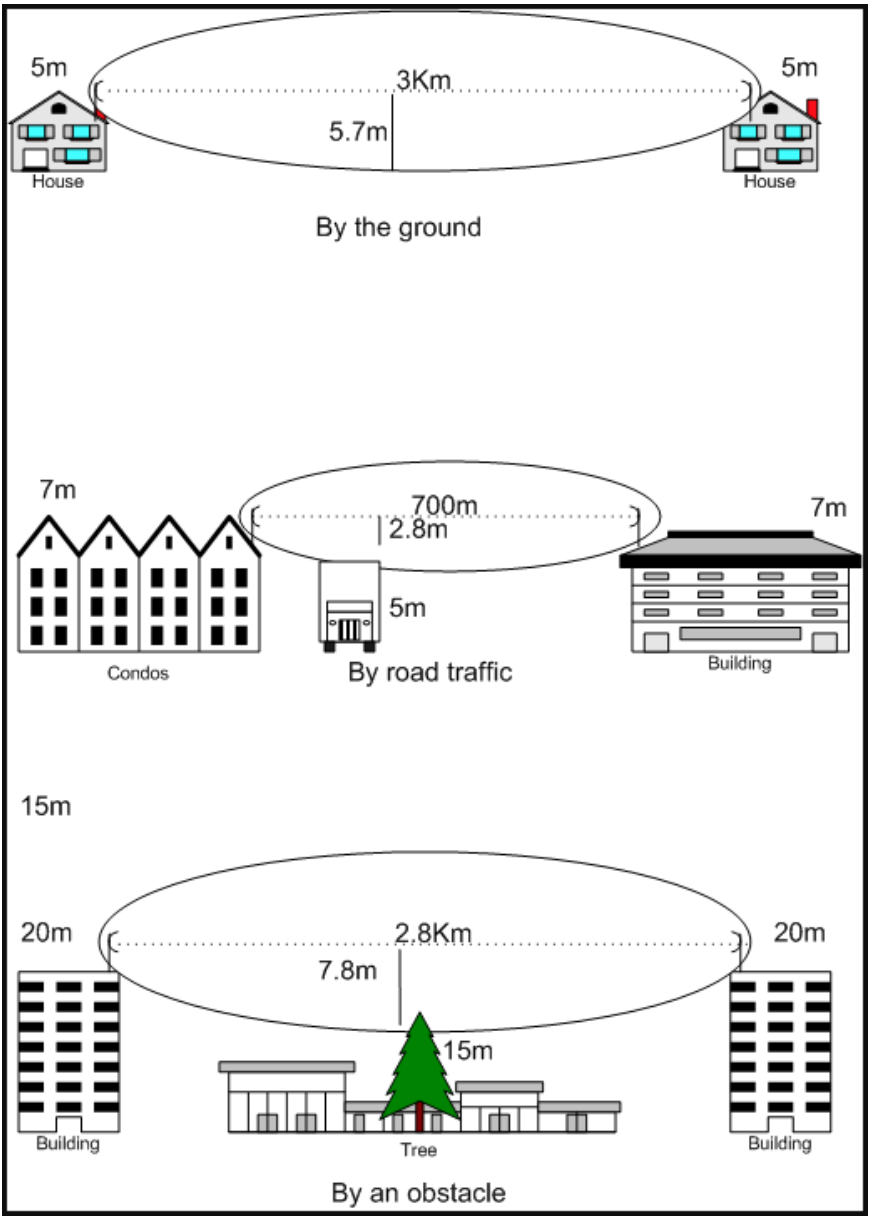

Figure 61: Examples of fresnel zone obstructions [4]

7.1.6 Large Scale Fading

Large-scale fading encompasses path loss and shadowing. Path loss, inherent to signal propagation through free space, cannot be circumvented. However, this doesn't influence the model, since the model employs the RSSI value at the optimal orientation as the reference or peak power level. For the employed microwave backhaul system, the LoS path between the Tx and Rx are expected to remain unobstructed. Additionally, since both the Tx and Rx are stationary except for the oscillatory motion, the risk of moving into a shadowing region is minimal. While transient obstructions by flying objects could cause short, deep fades (Figure 23) in the LoS path, long-lasting shadow fading is not anticipated.

7.1.7 Precipitation Based Fading

Rain and humidity within the transmission medium between the Tx and Rx can induce fading (high variance in RSSI data seen in Figure 24). This fading can manifest as either gradual changes due to alterations in humidity and water absorption or as rapid, small-amplitude, high frequency variations caused by rain. A potential strategy to address the impact of precipitation-induced fading involves employing filtering techniques and leveraging insights gained over several seconds of historical data. This approach may hold the promise of mitigating the influence of fading caused by rain and humidity by effectively smoothing out the effects and reducing their impact on signal quality.

7.1.8 Antenna Movements on the Other Side of the Link

RSSI variations at the receiver can also arise exclusively from movements of the transmitter antenna. The model can be adapted to anticipate these transmitter antenna movements without relying on the gyroscope data at the receiver side. This adjusted model will be effective for predicting deviations by utilizing properties of the 2nd order differential equations. Moreover, there's potential for both the receiver and transmitter antennas to experience movement. In such cases, the model may be able to estimate the relative motion. However, due to the increased complexity and testing requirements, the thesis will primarily concentrate on antenna movements on the receiver side of the link. The receiver side, which is equipped with IMU sensor data, provides a more manageable and comprehensive approach for the scope of the study. Appendix G delves into a situation where gyroscope data is disabled while running the EKF model to mimic movement on the transmitter antenna. However, conducting more extensive investigations into this scenario and enhancing model estimation accuracy lie outside the scope of the thesis.

7.2 Establishing Gain-Angle Relationship

Establishing a mathematical relationship between the "Angle of azimuth relative to the main beam axis" (referred to as **Angle**) and the "Gain relative to the main beam (dB)" (referred to as **Gain**) using specification documents will prove instrumental in modeling the filter or estimating the antenna deviation from its optimal orientation. Figure 62 illustrates the specifications for the given antenna (ANTC HPX 30).

7.2.1 Antenna Specification

1.5.17 ANT3 C 0.3 15 HP/HPX

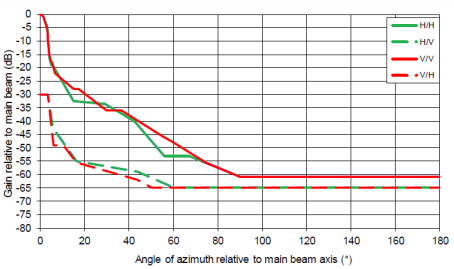

Angle (°)	H/H (dB)	Angle (°)	H/V (dB)	Angle (°)	V/V (dB)	Angle (°)	V/H (dB)
0.00	0.00	0.00	-30.00	0.00	0.00	0.00	-30.00
0.50	-0.10	3.60	-30.00	0.50	-0.10	3.60	-30.00
1.00	-0.30	5.60	-42.30	1.00	-0.30	6.00	-49.00
1.50	-1.00	6.90	-44.00	1.50	-1.00	10.50	-49.00
2.00	-2.00	16.20	-55.00	2.00	-2.00	16.20	-55.40
2.50	-3.10	44.00	-59.00	2.50	-3.50	43.70	-62.00
3.00	-4.70	60.00	-65.00	3.00	-5.50	50.00	-65.00
3.50	-6.60	180.00	-65.00	3.50	-7.60	180.00	-65.00
3.60	-8.90			3.60	-10.00		
3.90	-11.70			3.90	-12.20		
4.20	-15.90			4.20	-15.00		
5.10	-19.00			5.10	-18.00		
5.60	-19.00			5.30	-18.00		
15.00	-32.50			6.60	-22.20		
29.10	-33.70			15.00	-28.00		
42.30	-40.00			17.40	-28.00		
56.00	-53.00			30.00	-36.00		
67.30	-53.00			36.60	-36.00		
90.00	-61.00			55.00	-45.50		
180.00	-61.00			60.00	-48.00		
				74.70	-55.50		
				90.00	-61.00		
				180.00	-61.00		

Figure 62: Antenna specification

Given the requirement to establish a relationship (equation) between a single variable as a function of another single variable, a common approach is to employ a polynomial regression. This involves expressing the Gain (g) as a function of increasing powers of Angle (θ), as outlined in Equation (2).

$$g(\theta) = \sum_{i=0}^{\infty} a_i \cdot \theta^i \tag{2}$$

where $a_0, a_1, a_2, \cdots$ are coefficients for each polynomial term.

7.2.2 Simplifying Polynomial Regression Equation

Analyzing a sample radiation pattern allows us to make observations that will facilitate the simplification of Equation (2).

- In many specification documents, the exact location of side lobes isn't indicated. Instead, they often specify the peak power of these side lobes, making it challenging to determine the positions of nulls. To enhance the reliability of the estimated model, focusing on the main lobe and avoiding extreme non-linearities due to nulls is beneficial. One method to identify the transition to a side lobe involves assessing the slope of the differential Gain between adjacent Angle points, as expressed in Equation (5). If the slope decreases rather than increases, it indicates that the envelope is shifting from the main lobe to a side lobe.

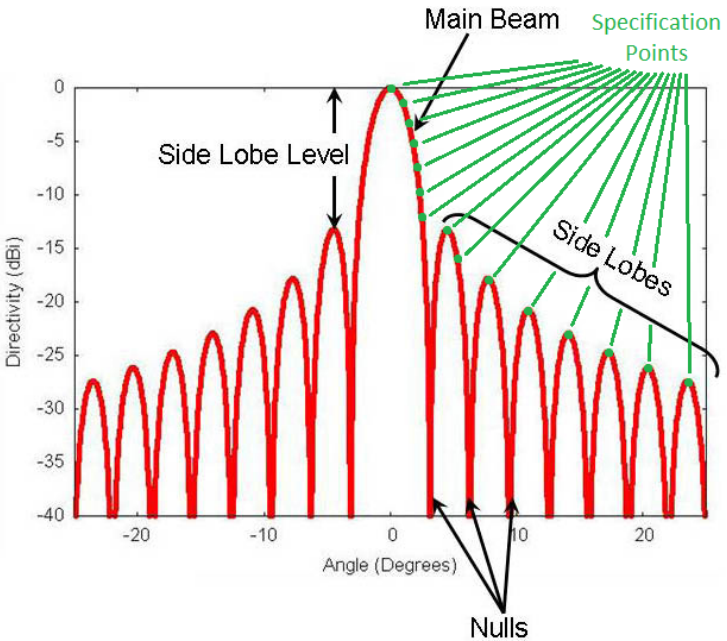

Figure 63: Example of an antenna pattern [13] [13]

- The fact that the Gain value in the specification remains consistent on either side of the main beam axis suggests that odd powers of θ cannot be employed in the equation. This is due to the potential disparity between the results obtained from positive and negative values of θ.

  $i \neq 1, 3, 5, \cdots$

[13] The figure is just an example and does not correspond to the antenna specification provided in Figure 62.

- At Angle 0, the Gain is 0 dB (first row of the antenna specification table in Figure 62), implying that coefficient a_0 should be zero.

  $a_0 = 0$

- To prevent utilization of an overfitted and intricate equation, a prudent approach involves commencing with a lower order equation and progressively increasing its order until a satisfactory fit against the specification is achieved.

  $i << \infty$

Rewriting Equation (2) (Non-zero even powers of θ)

$$g(\theta) = \sum_{i=2}^{2 \cdot n} a_i \cdot \theta^i \quad \forall \quad 1 \leq n << \infty \tag{3}$$

7.2.3 Estimating Maximum Angle Limit for Polynomial Regression

To exclusively account for specification points within the main lobe, it's crucial to determine the number of rows from the specification table that should be treated as data points for the polynomial regression. In order to identify the row index within the specification table corresponding to the side lobe, a methodology involves calculating the differential slope using adjacent sets of Angle points provided in the specification.

$$\Delta g_j = g_{j+1} - g_j \tag{4}$$

where g_j is the Gain relative to main beam listed in row/index j in the specification table (Figure 62).

$$m_j = \frac{\Delta g_{j+1} - \Delta g_j}{\Delta g_{j+1}} \tag{5}$$

where m_j is the change in the differential slope using adjacent points.

Tracing the radiation pattern plot towards the first null, it's anticipated that the slope will generally increase. Conversely, a decrease in slope could signify transition to a side lobe. While this observation holds true, minor deviations may occur due to factors such as antenna imperfections, material characteristics, measurement inaccuracies, quantization errors, and more. These can potentially result in semi-ideal radiation pattern, where the differential gain of the main lobe is not strictly increasing upto first null point. To account for these factors, a threshold of 0.1 or a 10% change will be employed to discern the shift from the main lobe to a side lobe. This threshold will serve as a useful criterion for accurately identifying these transitions.

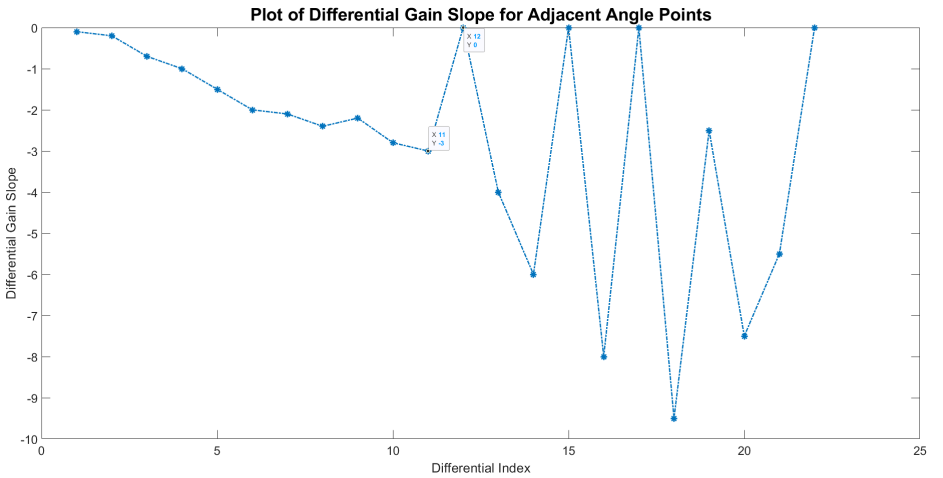

Figure 64: Slopes of differential gain

Referring to Figure 64, it's evident that Index 12 exhibits a notable decline in the slope (-3 to 0), which signifies a transition to a side lobe. In the case of Index 9, there's a reduction in slope, albeit not as pronounced. This subtle reduction can likely be attributed to the inherent characteristics of real antenna systems with semi-ideal radiation patterns. Of note is Index 11, corresponding to an angle of $4.2°$ or ~ 0.0733 radians. When attempting to fit the equation to the specification, it's pertinent to consider the data points upto this angle, subsequently referred to as the "Limit for equation fit" in subsequent plots.

7.2.4 Estimating Equation from Polynomial Regression Results

Employing the 11 data points extracted from the specification table (Figure 62), a series of trials involving various polynomial orders will be conducted. The aim is to identify the lowest order that yields a satisfactory fit against the data. Rewriting Equation (3) in matrix form, assuming order of N (even number):

$$\begin{bmatrix} g_1 \\ g_2 \\ g_3 \\ \vdots \\ g_{11} \end{bmatrix} = \begin{bmatrix} \theta_1^2 & \theta_1^4 & \theta_1^6 & \cdots & \theta_1^N \\ \theta_2^2 & \theta_2^4 & \theta_2^6 & \cdots & \theta_2^N \\ \theta_3^2 & \theta_3^4 & \theta_3^6 & \cdots & \theta_3^N \\ \vdots & \vdots & \vdots & \ddots & \vdots \\ \theta_{11}^2 & \theta_{11}^4 & \theta_{11}^6 & \cdots & \theta_{11}^N \end{bmatrix} \begin{bmatrix} a_2 \\ a_4 \\ a_6 \\ \vdots \\ a_N \end{bmatrix}$$

$$G = \Theta A$$

Solving for A

$$A = \Theta^{\dagger} G \tag{6}$$

where $\Theta^{\dagger}$ pseudo-inverse [30] of Θ.

$N = 2, 4, 6$ are attempted with the plots shown in Figure 65.

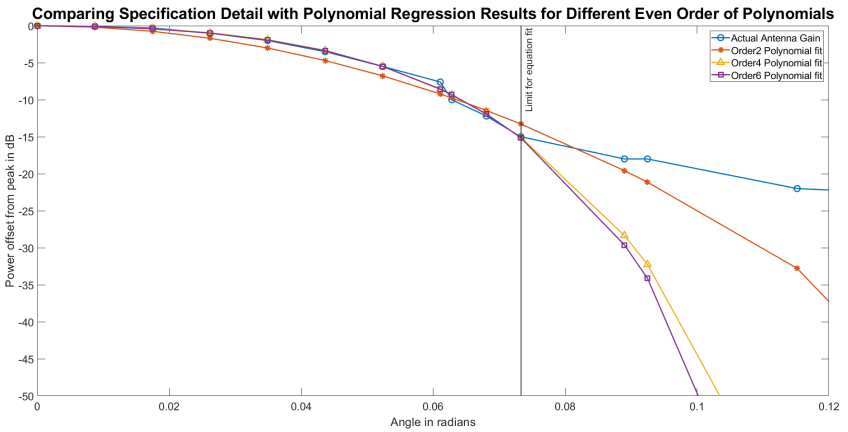

Figure 65: Polynomial regression for various even order of polynomials

It's apparent that Order2 ($N = 2$) doesn't align well with the theoretical antenna gain, displaying deviations from this gain before reaching the "Limit for equation fit". On the other hand, both Order4 ($N = 4$) and Order6 ($N = 6$) closely track the theoretical antenna gain. Order4 was chosen as the most suitable option, as it effectively captures the characteristics of the theoretical antenna gain. The coefficients for Order4 are provided in Equation (7).

$$g(\theta) = -3.0339 \times 10^5 \cdot \theta^4 - 1.1741 \times 10^3 \cdot \theta^2 \tag{7}$$

with $a_4 = -3.0339 \times 10^5$ and $a_2 = -1.1741 \times 10^3$ (approximated to 4 decimal places).

7.2.5 Alternative Methods for Estimating the Relationship

The micrawave radiation pattern can also be expressed as a function of the Bessel function (first kind with integral orders equal to 0) [31] or the same function in infinite series [32], both equations are listed below:

$$J_0(x) = \sum_{k=0}^{\infty} \frac{(-1)^k}{k!\Gamma(k+1)} \left(\frac{x}{2}\right)^{2k}$$

$$\text{where } \Gamma(k+1) = \int_0^{\infty} t^k e^{-t} dt$$

$$J_0(x) = 1 - \frac{1}{4}x^2 + \frac{1}{64}x^4 - \frac{1}{2304}x^6 + \cdots$$

While the equation presented will not be utilized due to the simplicity of the polynomial regression and the resultant Equation (7), it's worth noting the similarity between the expression of the radiation pattern as a sum of the even powers of x.

7.3 Dynamic Model

To formulate a model to estimate antenna movements, the state space variables must be identified. In this context, the hidden state to be estimated pertains to the angle of deviation from optimal antenna alignment (θ). Conversely, the known information or the output state is comprised of IMU gyroscope data and the RSSI measurements.

7.3.1 Model Description

As elaborated in Section 7.2, the angle of deviation from optimal alignment is constrained to fall within the bounds of the main lobe, with a maximum value of less than 4.2°. This threshold might vary depending on the specific antenna type. By encompassing all plausible microwave antenna configurations offered by Ericsson (Figure 4), it's evident that the maximum angle of the main lobe does not surpass 10°. In light of this, the small angle approximation [33] is deemed suitable within the confines of a 1% relative error. This approximation provides a practical means to simplify calculations while maintaining a satisfactory level of accuracy.

$$\sin\theta \approx \theta \text{ if } \theta \leq 10^\circ \tag{8}$$

Upon analyzing different oscillation types as detailed in Section 5, it's evident that the oscillatory behavior can be effectively modeled using a second-order differential equation. This equation bears a resemblance to those employed to describe mass-spring oscillators.

$$\ddot{\theta} + \alpha\dot{\theta} + \beta\theta = w_2 \tag{9}$$

Appendix F provides a comprehensive explanation of the meanings and significance of α, β and w_2, and the relationship to equations describing mass-spring oscillators.

As discussed in 7.1, only the gyroscope data from the IMU sensor will be utilized. Modeling two slowly varying offsets:

- b_1 = gyro bias [rad/s], with a small slow random walk drift $\dot{b}_1(t) = w_3(t)$
- b_2 = RSSI bias [dB], with a small slow random walk drift $\dot{b}_2(t) = w_4(t)$

Collecting the hidden state variables in a vector $x \in \mathbb{R}^4$,

$$\frac{d}{dt}\boldsymbol{x} = \frac{d}{dt}\begin{bmatrix} x_1 \\ x_2 \\ x_3 \\ x_4 \end{bmatrix} = \frac{d}{dt}\begin{bmatrix} \theta \\ \dot{\theta} \\ b_1 \\ b_2 \end{bmatrix} = \begin{bmatrix} 0 & 1 & 0 & 0 \\ -\beta & -\alpha & 0 & 0 \\ 0 & 0 & 0 & 0 \\ 0 & 0 & 0 & 0 \end{bmatrix}\begin{bmatrix} x_1 \\ x_2 \\ x_3 \\ x_4 \end{bmatrix} + \begin{bmatrix} w_1 \\ w_2 \\ w_3 \\ w_4 \end{bmatrix} \tag{10}$$

$$= A\boldsymbol{x} + \boldsymbol{w} \tag{11}$$

The gyroscope sensor and radio give us the measurements

$$\text{gyro}^{14} = \frac{1}{K_{gyro}}\,(\dot{\theta}) + b_1 + v_1 \quad [\text{rad/sec}] \tag{12}$$

$$\text{RSSI} = g(\theta) + b_2 + v_2 \quad [\text{dB}] \tag{13}$$

Derived in Section 7.2, the RSSI measurement function

$$g(\theta) = a_4\theta^4 + a_2\theta^2 = -3.0339 \times 10^5 \cdot \theta^4 - 1.1741 \times 10^3 \cdot \theta^2$$

After conversion of Equation (11) to discrete-time, with $\boldsymbol{x}_k = \boldsymbol{x}(kT)$, where T is the sample time (0.01s),

$$\boldsymbol{x}(k) = \exp(AT)\ \boldsymbol{x}(k-1) + \boldsymbol{w}(k) = \Phi\ \boldsymbol{x}(k-1) + \boldsymbol{w}(k)$$

Output states :

$$\boldsymbol{y}(k) = \begin{bmatrix} \text{gyro} \\ \text{RSSI} \end{bmatrix} = \begin{bmatrix} \frac{1}{K_{gyro}}\ \Big(x_2(k)\Big) + x_3(k) \\ g\Big(x_1(k)\Big) + x_4(k) \end{bmatrix} + \begin{bmatrix} v_1(k) \\ v_2(k) \end{bmatrix}$$

$$= h\Big(\boldsymbol{x}(k)\Big) + \boldsymbol{v}(k)$$

[14] For a detailed derivation of the equation, refer to Section 7.9.

Using Taylor series [34] expansion for Φ,

$$\Phi = \exp(AT) = I + AT + \frac{(AT)^2}{2!} + \frac{(AT)^3}{3!} + \cdots$$

When αT and βT are small, higher order terms (> 1) are negligible and the below approximation holds

$$\Phi = \exp(AT) \approx I + AT = \begin{bmatrix} 1 & T & 0 & 0 \\ -\beta T & 1 - \alpha T & 0 & 0 \\ 0 & 0 & 1 & 0 \\ 0 & 0 & 0 & 1 \end{bmatrix}$$

Given that the state space model is non-linear, the Extended Kalman Filter (EKF) [35], a derivative of the original Kalman Filter, will be employed. The EKF operates by linearizing a non-linear system around an estimation of the current mean and covariance of the states.

7.3.2 Extended Kalman Filter (EKF) Equations:

Time Update:

$$4 \times 1 : \hat{x}(k|k-1) = \Phi \hat{x}(k-1|k-1)$$

$$4 \times 4 : P_{k|k-1} = \Phi P_{k-1|k-1} \Phi^T + Q$$

To simplify matters, let's assume that the noise terms w_1 to w_4 are uncorrelated. This assumption results in a diagonal covariance matrix.

$$Q = \mathrm{Cov}(\boldsymbol{w}) = \mathrm{diag}(q_1, q_2, q_3, q_4)$$

Similarly, the noise terms v_1 and v_2 are uncorrelated,

$$R = \mathrm{Cov}(\boldsymbol{v}) = \mathrm{diag}(r_1, r_2)$$

Measurement Update:

$$2 \times 1 : \tilde{y}_k = \begin{bmatrix} \text{gyro} \\ \text{RSSI} \end{bmatrix} - \begin{bmatrix} \frac{1}{K_{gyro}} \Big(\hat{x}_2(k|k-1) \Big) + \hat{x}_3(k|k-1) \\ g\Big(\widehat{x}_1(k|k-1) \Big) + \widehat{x}_4(k|k-1) \end{bmatrix}$$

$$2 \times 2 : S_k = H_k P_{k|k-1} H_k^T + R$$

$$4 \times 2 : K_k = P_{k|k-1} H_k^T S_k^{-1}$$

$$4 \times 1 : \hat{x}(k|k) = \hat{x}(k|k-1) + K_k \tilde{y}_k$$

$$4 \times 4 : P_{k|k} = (I_4 - K_k \ H_k) P_{k|k-1}$$

where,

$$H_k = \left. \frac{\partial h}{\partial x} \right|_{\widehat{x}(k|k-1)} = \begin{bmatrix} 0 & \frac{1}{K_{gyro}} & 1 & 0 \\ g'\Big(\widehat{x}_1(k|k-1) \Big) & 0 & 0 & 1 \end{bmatrix}$$

$$g'(\theta) = \frac{\partial g(\theta)}{\partial \theta} = 4a_4\theta^3 + 2a_2\theta$$

7.3.3 EKF Model Parameter Summary

Certain parameters within the proposed model can be assessed by analyzing historical data samples, while others are set during the initial configuration based on properties derived from stationary data. Additionally, specific parameters require calibration following the observation of outcomes from real-world data. This section will provide a concise overview of the chosen methodology for configuring these model parameters.

- α : Setting this parameter to zero is an option. RSSI/gyroscope output state variables will govern the values of the hidden state variables.
- β : This parameter can also be initialized to zero. However, it necessitates configuration when none of the gyroscopes exhibit correlation with RSSI variations, which occurs in cases of movements on the transmitter (Tx) inducing RSSI fluctuations on the receiver (Rx) side. Further elaboration on this process is available in Appendix G.
- K_{gyro} : This parameter requires periodic configuration through the observation of historical data samples. This updates the model with the suitable scaling factor for accurate current and future state estimations. Further elaboration on this process is available in Section 7.9.
- q_1 : Requires calibration.
- q_2 : Requires calibration.
- q_3 : Equivalent to the Allan variance with angle random walk. The value is selected from the gyroscope exhibiting the highest correlation with RSSI values. Select gyroscope "Allan variance" value from Table 1.
- q_4 : Equivalent to the Allan variance with Bias Random Walk for the RSSI sensor. Given the challenges in estimating this value through "stationary data", the value is set to variance of peak values from historical data samples divided by sample duration.
- r_1 : Equivalent to the variance value of the gyroscope that exhibits the highest correlation with RSSI values. Select gyroscope "Variance" value from Table 1.
- r_2 : Equivalent to the RSSI variance obtained from stationary data. Select RSSI "Variance" value selected from Table 1.

To initiate the EKF process, the hidden state variables must be initialized with certain initial values.

- θ_0 : Set to 0. The filtering process will facilitate the convergence of the state value towards its actual value.
- $\dot{\theta}_0$: This can be configured to match the scaled value of the initial gyroscope reading, once the bias error has been eliminated. The following formula is used:
  $\dot{\theta}_0 = (\text{gyro}_0 - b_1) \times K_{gyro}$
- b_{1_0} : The value of the bias error corresponding to the gyroscope reading that exhibits the strongest correlation with the RSSI values is selected. Select gyroscope "Bias value" from Table 1.
- b_{2_0} : Corresponds to the RSSI value at optimal orientation and is configured based on observations from previous samples. It is essentially the maximum RSSI value derived from the preceding 10-second sample window following FIR filtering.

7.4 Feature Extraction Based on Oscillation Properties

The nature of the oscillations offers the opportunity to extract intriguing features. The EKF model encompasses numerous parameters that necessitate meticulous adjustment to minimize estimation errors. Certain parameters can be estimated by utilizing data from preceding time instances. Employing these parameters within the EKF model facilitates the estimation of current hidden state values, in addition to predicting future state values. This iterative process of parameter estimation and state prediction enhances the model's accuracy and predictive capabilities. A summary of useful features is provided in this section, with more details provided in subsequent sections.

Selecting the gyroscope that correlates the best with RSSI

Since the frame of reference between the IMU and antenna remains undisclosed, determining the gyroscope sensor that exhibits the strongest correlation with RSSI variations is pivotal in the feature extraction effort.

Estimating the angle between optimal alignment and extremes in an oscillation

Based on the assumptions delineated in the earlier section, particularly Section 7.1.2, it becomes feasible to estimate the deviation from optimal alignment. This can be achieved by examining the RSSI values at the oscillation peaks and dips as shown in Figure 66.

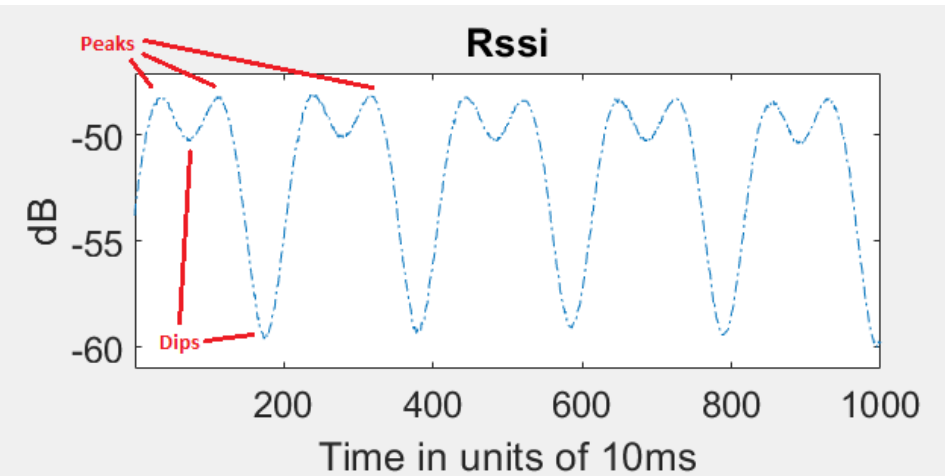

Figure 66: Example of peaks and dips for partially unbalanced case

Estimating the gyroscope scaling factor

Unless the focal point is precisely situated between the IMU (on the radio) and the antenna, the angular rotation of the antenna will not equate to the angular rotation derived from the gyroscope data. To reconcile this discrepancy, a gyroscope scaling factor can be introduced. This scaling factor is employed to ensure that the scaled gyroscope values accurately correspond to the rotation of the antenna. By incorporating this factor, alignment between the gyroscope-derived data and the actual antenna movement can be achieved, enhancing the accuracy of the antenna deviation estimation.

For the sake of simplicity, the feature extraction and EKF processes are carried out on the same dataset. In an actual implementation of the proposed solution, the feature extraction is intended to be conducted on the most recent 10-second window of sensor data. Subsequently, utilizing the extracted features, the parameters (most suitable gyroscope, K_{gyro}, q_3, q_4, r_1) of the EKF model are adjusted. Due to the substantial processing demands associated with feature extraction, this procedure can be executed offline (not on the radio). Once the parameters are determined, the EKF process can then be performed in real-time (on the radio). The process of feature extraction can be set to occur periodically, under the assumption that the oscillation's nature will not undergo significant changes within short intervals. For instance, the EKF, active at time t could be refreshed every 1 second, following processing on the dataset ranging from $t - 11$ seconds to $t - 1$ seconds, allowing for 1-second processing overhead time. On the contrary, the EKF is required to execute the sensor fusion process in real time, accommodating sensor data arriving every 10 ms. The EKF procedures encompass a series of matrix multiplication steps, and as such, the processing duration should not exceed 10 ms, even for a radio system with relatively modest processing capabilities. Section 8 delves into this approach in more detail using data from manually induced mast swaying.

Upcomming sections are summarized below

- Removing high frequency noise using FIR filter
- Selecting a suitable gyroscope sensor
- Estimating the positions of peaks and dips
- Estimating the angle deviation from optimal alignment
- Estimating the gyroscope scaling factor
- Estimating the value for noise variance of different states
- Running EKF using current samples

7.5 FIR Filter Design

To implement the approach discussed earlier, a precise time alignment between the sensor data and RSSI data is essential. However, challenges arise due to potential differences in frequencies between these two datasets—whether they are the same or distinct (as in the balanced vs. unbalanced case)—as well as the presence of high-frequency noise (> 10 Hz). The application of IIR filters is impractical due to the inherent non-linear phase distortion they introduce.

In lieu of IIR filters, a more suitable option is the use of FIR filters. FIR filters exhibit linear phase characteristics and provide a more suitable solution for time alignment while minimizing phase distortion. Figure 67 illustrates the frequency response of the FIR filter utilized in this context. This choice of filter facilitates effective time alignment between the sensor and RSSI data, enhancing the synchronization process for accurate analysis.

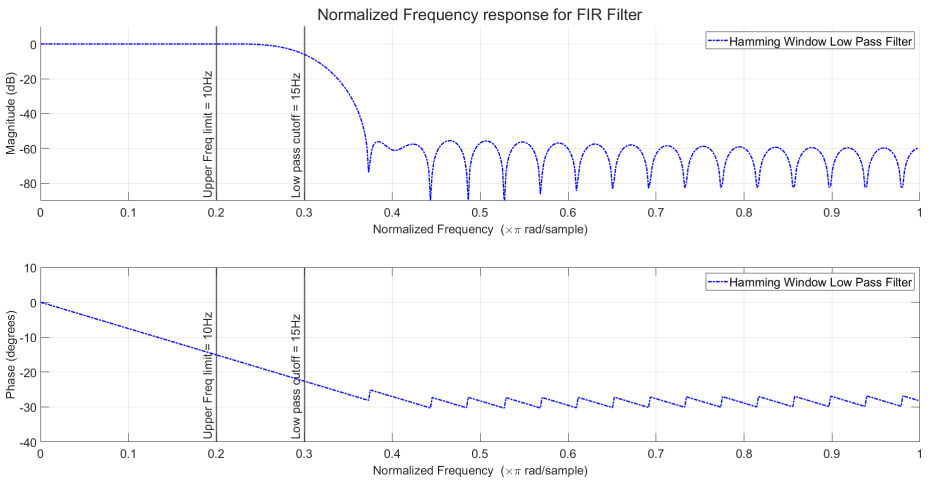

Figure 67: FIR filter response

Filter Configuration:

- Filter type : Low pass filter
- FIR window : Hamming window
- Filter order : 48
- Sampling rate : 100 Hz
- Cutoff frequency[15] : 15 Hz

[15]To use *fir1* function from MATLAB, Stopband edge frequency W_s needs to be provided, which equates to 2/Sampling rate × Cutoff frequency

7.6 Selecting Gyroscope Sensor that Correlates Best with RSSI

The approach used to establish cross-correlations in the preceding Section 6.3 is likewise employed to identify the gyroscope that yields the highest cross-correlation factor. An important difference to note is that this section employs standard cross-correlation, as opposed to the "normalized" cross-correlation utilized in Section 6.3. A normalized cross-correlation between two signals always has a maximum possible (absolute) value of 1. However, in a standard cross-correlation process, the resulting value can exceed 1, depending on the intensity of the signals being analyzed. This is done to highlight the emphasis that the model functions optimally with gyroscopes demonstrating strong normalized cross-correlation as well as high magnitudes. Higher magnitudes contribute to enhanced reliability in feature extraction. It's plausible that multiple gyroscopes could exhibit robust cross-correlations, potentially allowing for the fusion of information from various gyroscopes to estimate antenna movements. However, the scope of this thesis is to determine the antenna deviation from optimal alignment, albeit in any direction. The aspect of fusing information from multiple gyroscopes lies outside the scope of the thesis, and the approach will be limited to utilizing the most prominent cross-correlation among the three gyroscopes. This focused methodology simplifies the analysis while still providing valuable insights into antenna movements.

For all of the cases, the gyroscope Z-axis exhibits the highest cross-correlation value, as clearly demonstrated in Figures 69, 71 and 73. It is worth noting that a comparative analysis should be conducted between the performance of both cases: the cross-correlation with the original gyroscope signal and the cross-correlation with the gyroscope signal subsequent to doubling the peak frequency, with the objective of selecting the most suitable gyroscope signal.

7.6.1 Almost Balanced Oscillation

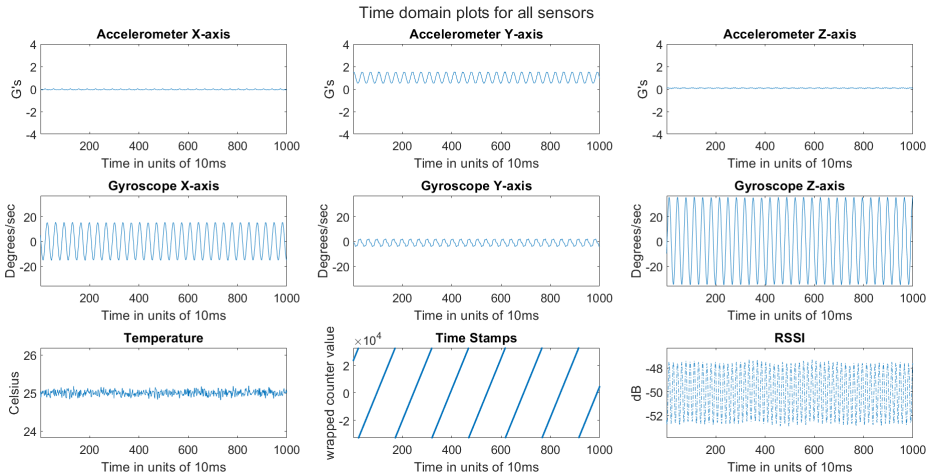

Figure 68: Example of almost balanced oscillation

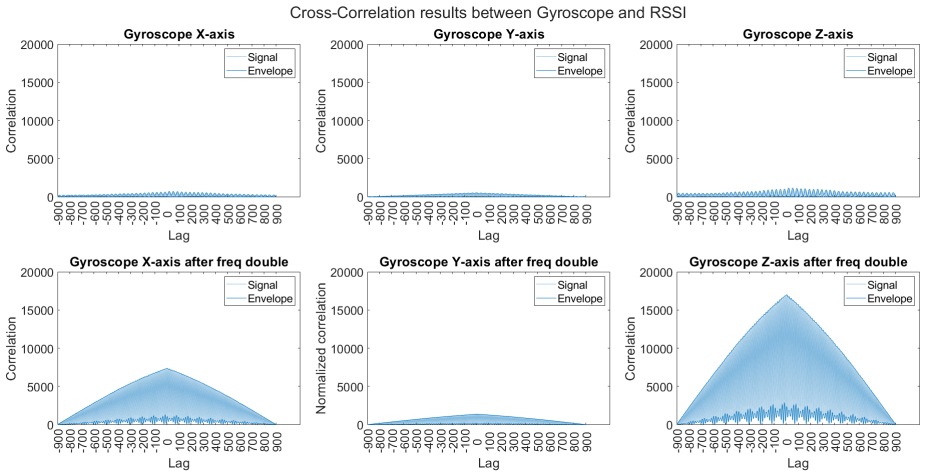

Figure 69: Comparison of cross-correlation results for all gyroscope axes - almost balanced oscillation

7.6.2 Partially Balanced Oscillation

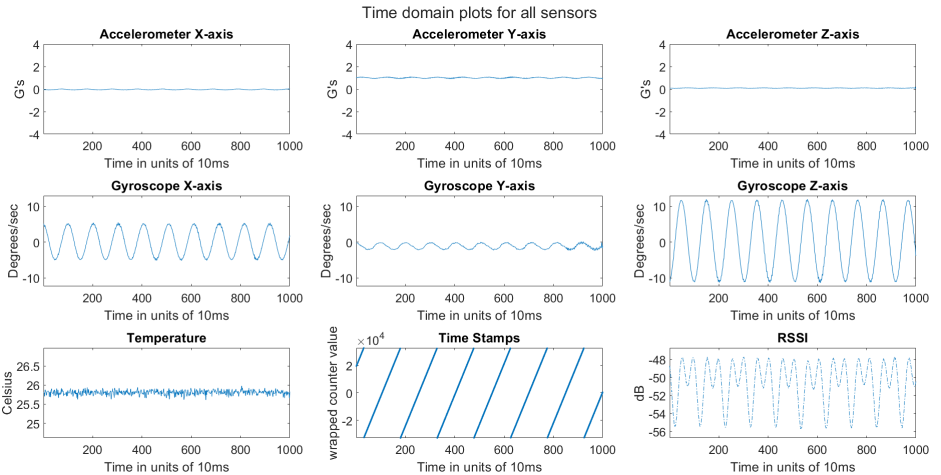

Figure 70: Example of partially balanced oscillation

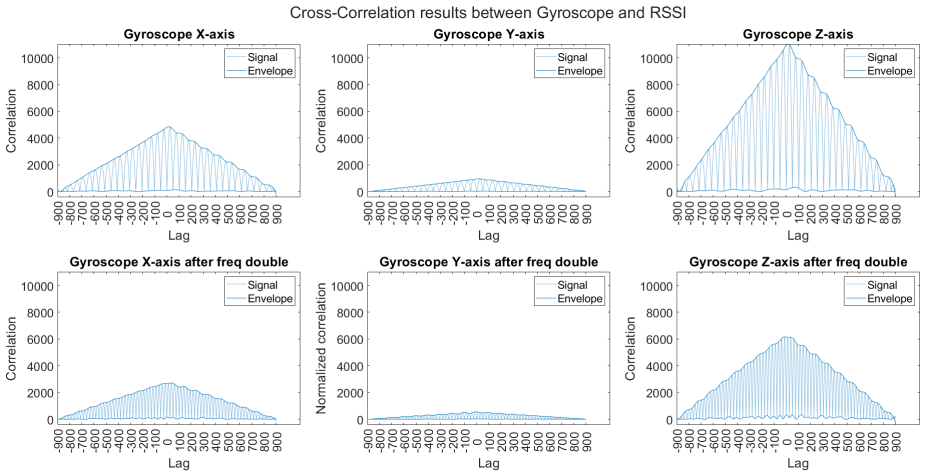

Figure 71: Comparison of cross-correlation results for all gyroscope axes - partially balanced oscillation

7.6.3 Almost Unbalanced Oscillation

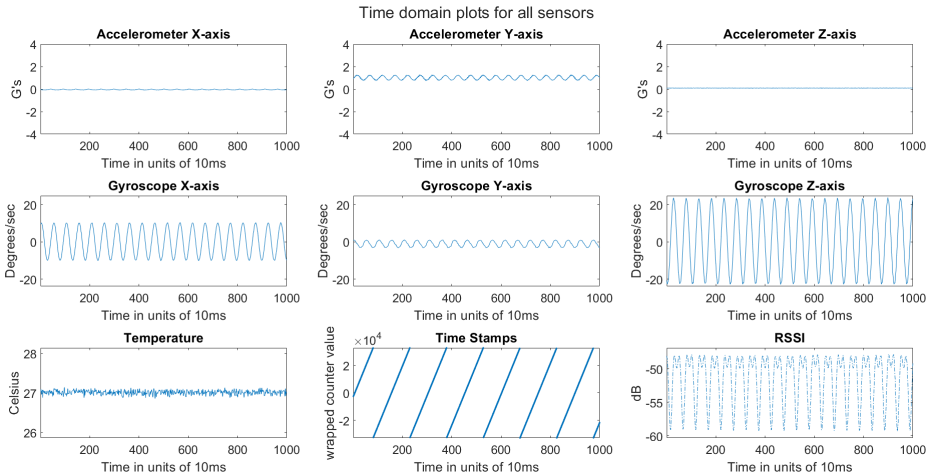

Figure 72: Example of almost unbalanced oscillation

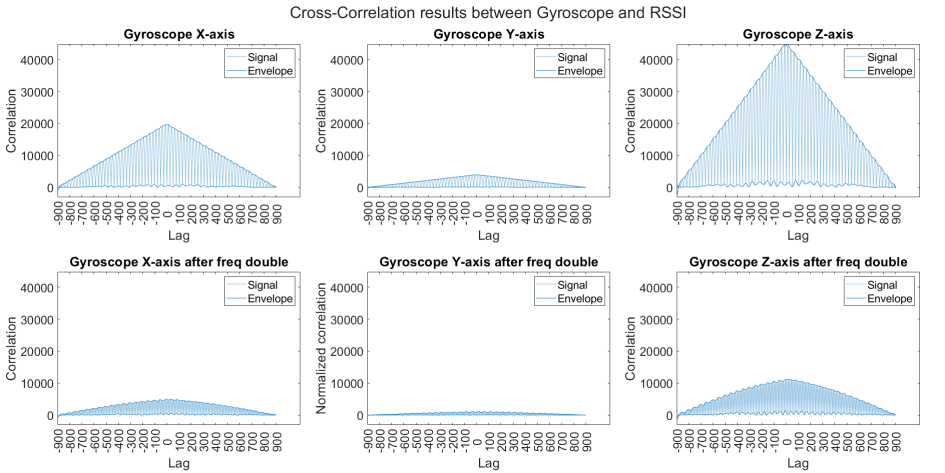

Figure 73: Comparison of cross-correlation results for all gyroscope axes - almost unbalanced oscillation

7.7 Filtering and Synchronization Between the Gyroscope and RSSI

Identification of triplets consisting of 2 dips and 1 peak will be necessary to estimate deviation angle from optimal alignment. Under ideal conditions of balanced oscillations, this angle will be zero. While the task of estimating peaks and dips in RSSI measurements can be as straightforward as detecting local minima and maxima, the received wireless signal is susceptible to various forms of noise, including thermal noise and fading due to factors such as rain or obstructions.

In order to mitigate the influence of noise, it's advantageous to rely on IMU sensor data, which remains less susceptible to such noise sources. When an object undergoes rotational oscillation between two extremes, the object is stationary for a brief duration at these extremes. Identifying the time instances when the gyroscope value is zero and time-aligning these instances with the RSSI data facilitates pinpointing the dips in the signal. For the peaks, the RSSI maxima between two dips is selected.

Upon the application of FIR filtering, the emergence of ripples at the initial moments can be expected for signals with non-zero starting values. This phenomenon occurs due to a rapid temporal transition, which is associated with the distribution of energy across all frequency components. Filtering serves to confine this energy to the pass band, resulting in the manifestation of high-frequency ripples during the transition from zero to a non-zero value. This may lead to additional zero crossings that do not represent the original signal. To counter this problem, the initial 1-second segment of the filtered output is excluded from feature extraction, and its omission has minimal impact on the results. Features extracted from the latter part of the 10-second window better capture the current signal characteristics and are more representative of its behavior.

While zero crossing points effectively represent the oscillation extremes, they can sometimes be misconstrued as minor ripples, especially when the antenna is in a nearly stationary condition (as illustrated in Figure 16). To differentiate between these scenarios, the following criteria are assessed after applying FIR filtering to eliminate high-frequency components (> 10 Hz).

- The separation between two consecutive zero crossings in the gyroscope data must align with the oscillation frequency of interest, which ranges from 0.5 Hz to 5 Hz. This requirement translates to a time interval between 1 second and 0.1 seconds[16].
- Zero-crossing points from the gyroscope data are considered after the initial 1-second period, to discard induced ripple effects from FIR filtering.
- Detect only one RSSI peak (local maximum) occurring between the two instances of zero crossing.
- The minimum angle estimated from any of the dips in the triplet must exceed the minimum non-zero angle specified in the antenna specifications, which, as depicted in Figure 62, corresponds to 0.5 degrees. This criterion is essential to prevent false detections of triplets caused by noise or rain-induced fading.

Pairs of zero crossings (those occurring outside the defined time limits or within the initial one-second period) and triplets (those with more than one local RSSI maxima or with estimated angle from the dips less than 0.5 degree) that do not satisfy the specified criteria are subject to rejection.

[16]To clarify, a cycle with a frequency of 1 Hz, corresponding to a 1-second duration, crosses zero points twice. This results in a zero-crossing interval of 0.5 seconds, which is half the duration of the full cycle.

7.7.1 Almost Balanced Oscillation

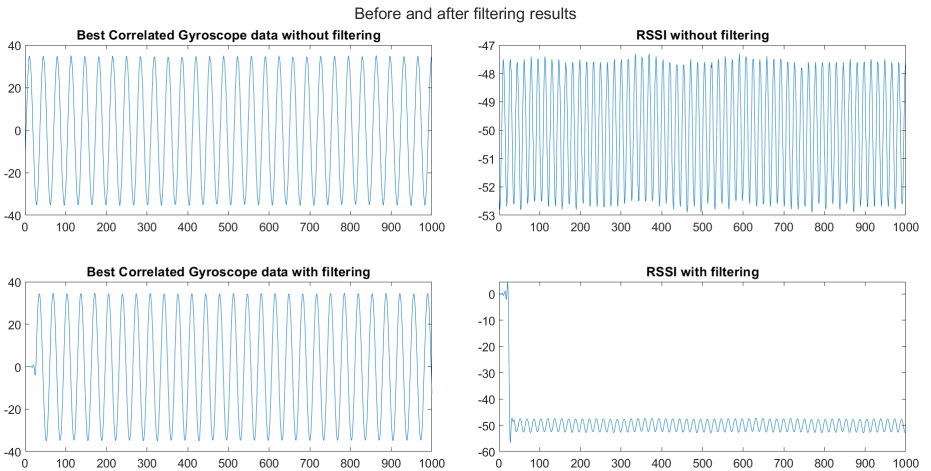

Figure 74: Gyroscope and RSSI after FIR filtering for almost balanced oscillation

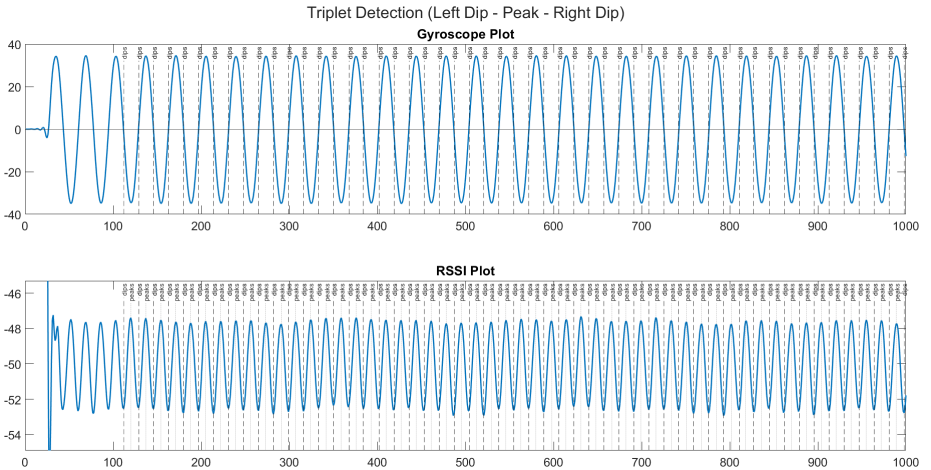

Figure 75: Detecting triplet sets for balanced oscillation (ignoring the first 1 second)

7.7.2 Partially Balanced Oscillation

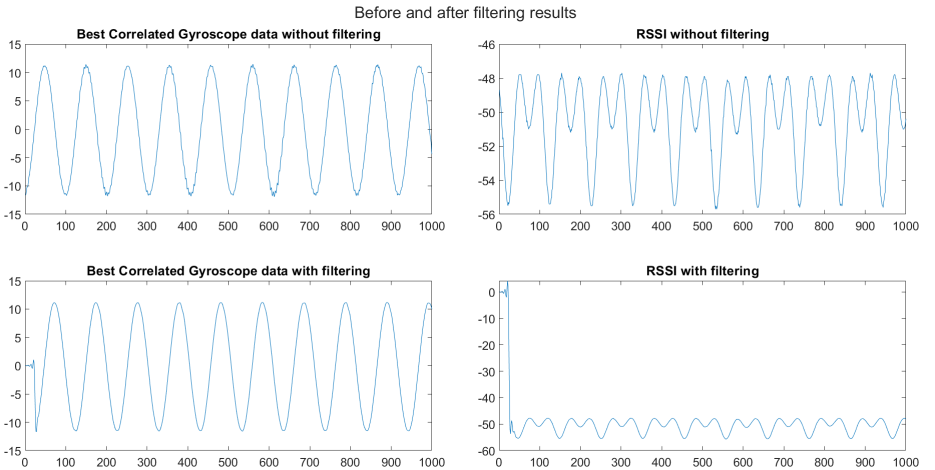

Figure 76: Gyroscope and RSSI after FIR filtering for partially balanced oscillation

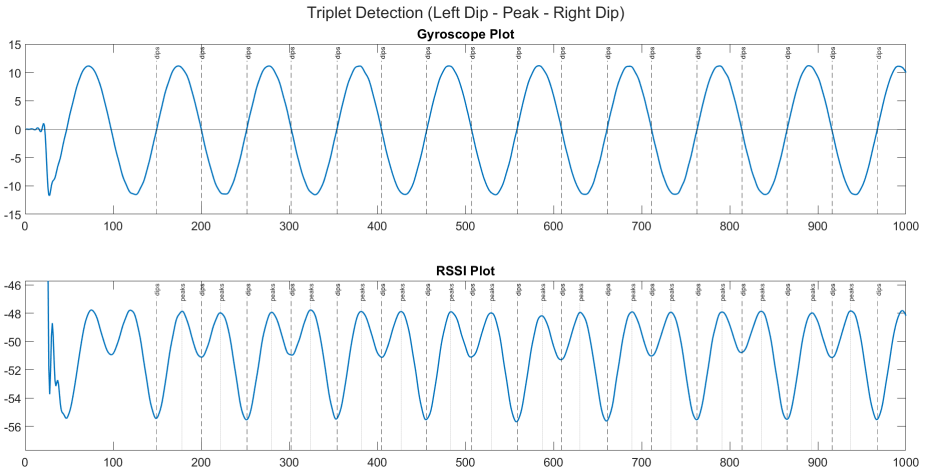

Figure 77: Detecting triplet sets for partially balanced oscillation (ignoring the first 1 second)

7.7.3 Almost Unbalanced Oscillation

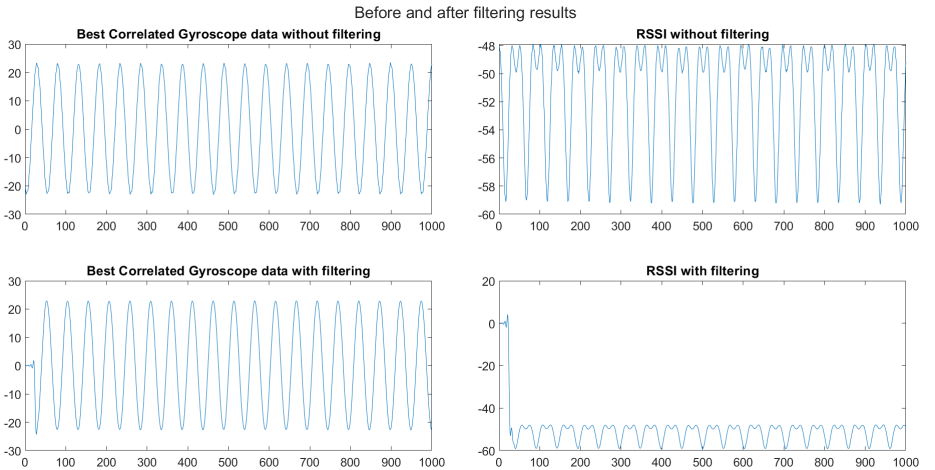

Figure 78: Gyroscope and RSSI after FIR filtering for almost unbalanced oscillation

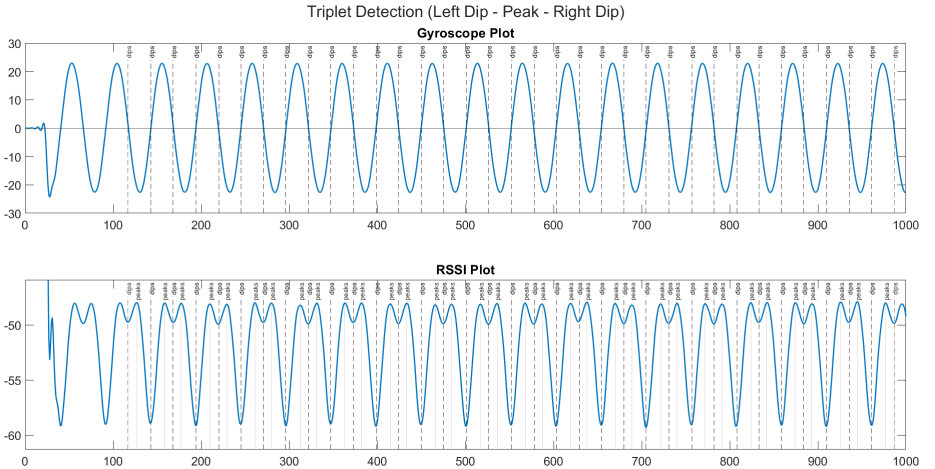

Figure 79: Detecting triplet sets for almost unbalanced oscillation (ignoring the first 1 second)

7.8 Estimating the Angle Deviation from Optimal Alignment

Given the knowledge of the RSSI value at the dips (R_d) and the peak RSSI value (R_p), the angle can be determined using Equation (7). By utilizing the difference in RSSI between dips and peaks, the angle on each side of optimal alignment can be calculated through the resolution of the following polynomial expression.

$$(R_d - R_p) = a_4 \cdot \theta^4 + a_2 \cdot \theta^2 \tag{14}$$

Based on Equation (7), a_2, a_4 is already known. Solving the aforementioned expression will yield four θ values, comprising two complex values and two real values. Among the real values, one will be positive, and the other will be negative, both with equal absolute magnitudes. The absolute value of the real solution will represent the angle value.

In an unbalanced scenario, the θ value will differ on either side of the optimal alignment. This will be denoted as θ_l and θ_r, corresponding to the left and right angles within a triplet. It is useful to determine the mid way position between two extremes in an oscillation, which will be termed as "offset-angle". For a stable oscillation, the offset-angle should be nearly consistent.

$$\theta_{dev} = \frac{\theta_l - \theta_r}{2} \tag{15}$$

Each point within the plots depicted in Figures 80, 81, and 82 corresponds to a θ_{dev} value for every set of triplets as identified in the Section 7.7. Although these values are not explicitly employed in the EKF model, they serve as a means to verify the accuracy of the estimation, which will be discussed in greater detail in Section 7.10.

Given the potential existence of multiple triplet instances within a single window, employing a weighted average approach could be beneficial in determining an approximate deviation value over the entire 10-second log. If there are M such triplet instances within a 10-second window and assigning greater weights to triplets more recent in time, the weighted average can be expressed as,

$$\widehat{\theta}_{dev} = \frac{\sum_{i=1}^{M} w_i \cdot \theta_{dev_i}}{\sum_{i=1}^{M} w_i} \tag{16}$$

where w_i represents the time within the 10-second window when the corresponding triplet was detected.

7.8.1 Almost Balanced Oscillation

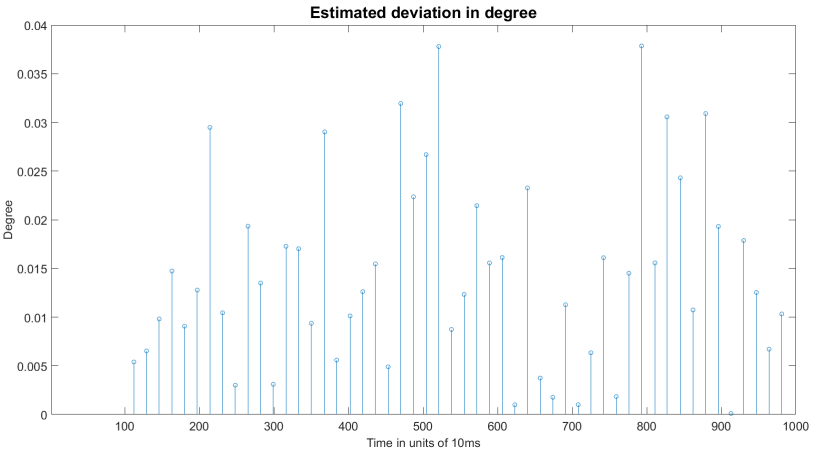

Figure 80: Estimated offset-angle using triplet information for almost balanced oscillation

As anticipated, in the case of almost balance oscillation, the offset-angle is minimal, with all values below 0.05 degrees.

7.8.2 Partially Balanced Oscillation

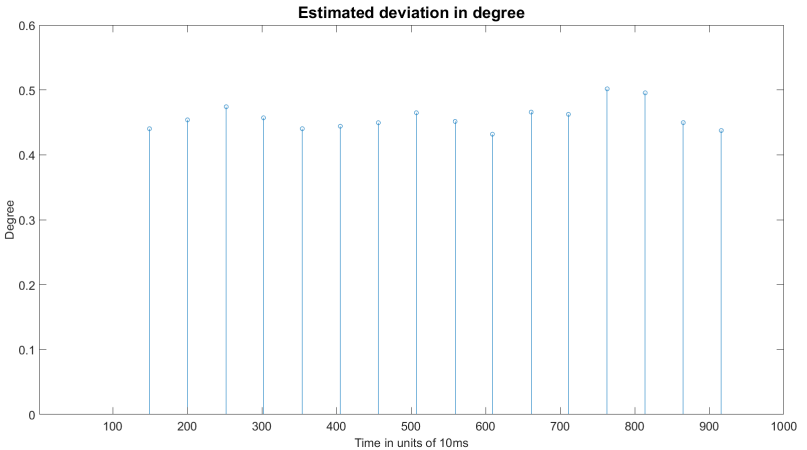

Figure 81: Estimated offset-angle using triplet information for partially balanced oscillation

In a partially balanced scenario, the offset-angle falls within the range of 0.4 to 0.5 degrees. These values should be higher than the estimates for balanced oscillation and lower for an unbalanced case.

7.8.3 Almost Unbalanced Oscillation

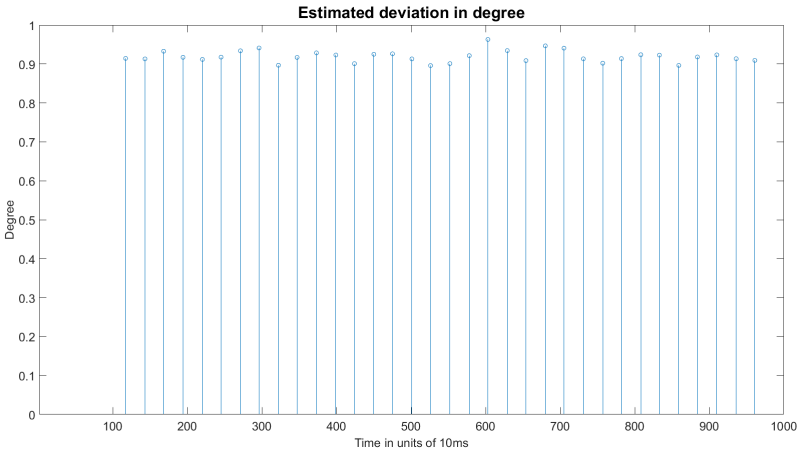

Figure 82: Estimated offset-angle using triplet information for almost unbalanced oscillation

As anticipated, the almost unbalanced oscillation exhibits the highest offset-angle in comparison to the other cases.

7.9 Estimating the Gyroscope Scaling Factor

Reiterating the observation from Section 7.1.1,

$$\text{gyro} \propto \dot{\theta}$$

The solution to estimating the gyroscope scaling factor is by solving the minimzing function. From the triplet data in the previous section, we have the two angles, (θ_l, θ_r) at time instance (t_l, t_r), where (l, r) represents left and right dips respectively.

The cumulative angle, derived from the gyroscope data in a scenario where the sensor precisely monitors antenna rotation, can be expressed as follows:

$$\theta_r = \theta_l + \int_{t=t_l}^{t_r} \dot{\theta}(t) \cdot dt \tag{17}$$

In reality, since the sensor is not measuring antenna movements but rather the radio movements, and the focal point of rotation can be anywhere in space; the gyroscope movements will not exactly reflect the antenna movements. Given the context of working with small degrees, the problem can be approximated to be linear.

Here, the scaling factor that ensures the gyroscope data reflects the antenna movements is denoted by a variable K_{gyro}. We define a function that determines the difference between the accumulated θ from gyroscope measurements and target angle θ_r, while multipling the scaling factor with gyroscope data. The below equation assumes the gyroscope has zero bias and noise.

$$F(K_{gyro}) = \theta_r - (\theta_l + \int_{t=t_l}^{t_r} \text{gyro}(t) \cdot K_{gyro} \cdot dt) \tag{18}$$

The K_{gyro} that minimizes the absolute value of the above function will be a good estimate of the scaling factor.

$$\widehat{K}_{gyro} = \underset{K_{gyro} \in \mathbb{R}}{\arg\min} \left| F(K_{gyro}) \right| \tag{19}$$

In discrete domain and assuming known gyroscope bias, the above equation can be rewritten as

$$\widehat{K}_{gyro} = \underset{K_{gyro}\in\mathbb{R}}{\arg\min} \left| \theta_r - \left(\theta_l + \sum_{t=t_l}^{t_r} \Big(\text{gyro}(t) - \text{bias}\Big) K_{gyro} T \right) \right| \quad (20)$$

where T is the sampling rate.

7.9.1 Almost Balanced Oscillation

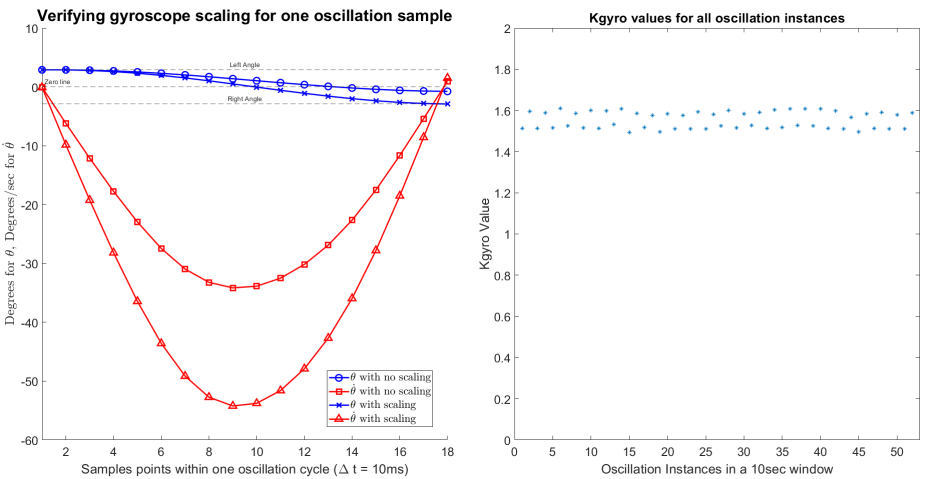

Figure 83: Estimated scaling factor for almost balanced oscillation

The oscillatory nature of the K_{gyro} estimate as seen on the right subplot for all three cases is due to the slight deviation of the actual bias error value in comparison to one derived from the stationary data. The mean value of all the K_{gyro} estimates within a 10-second window gives a better estimate of the actual K_{gyro} value.

7.9.2 Partially Balanced Oscillation

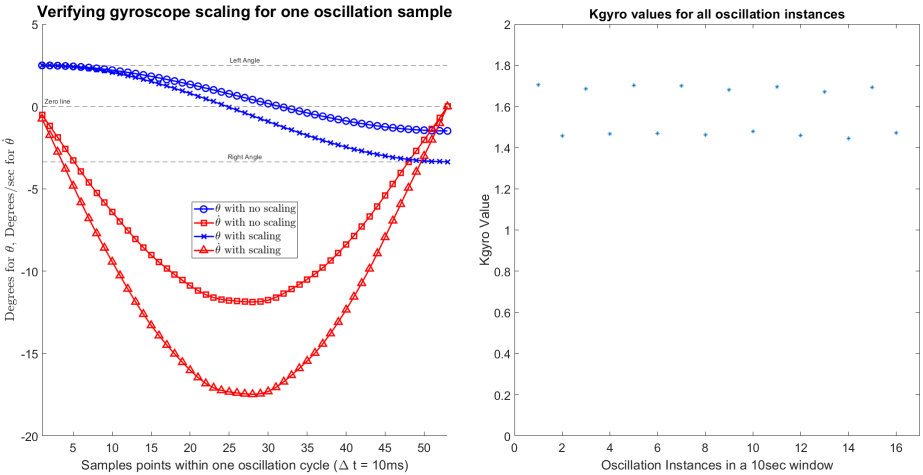

Figure 84: Estimated scaling factor for partially balanced oscillation

7.9.3 Almost Unbalanced Oscillation

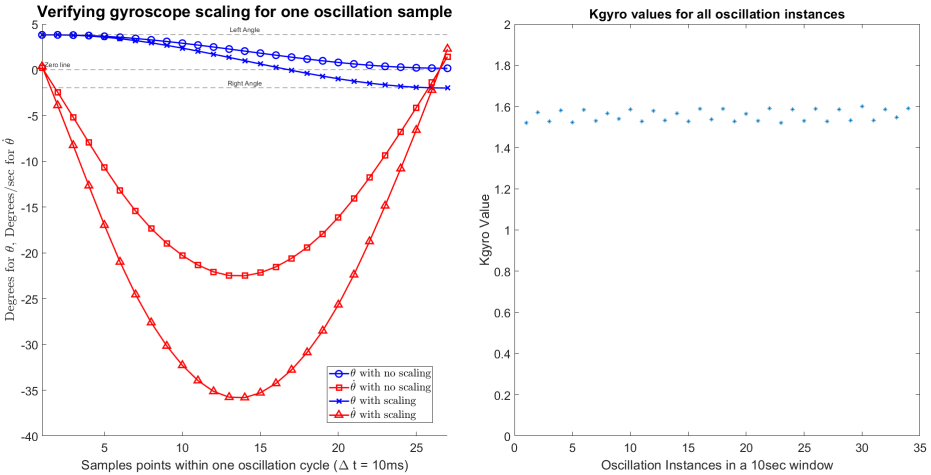

Figure 85: Estimated scaling factor for almost unbalanced oscillation

In all three scenarios, the mast sway generator system induced similar oscillation types, with the sole distinction lying in the offset-angle. The mean value of K_{gyro} serves as the periodically updated value supplied to the EKF model.

After estimating K_{gyro}, this parameter is then updated for the model, as described in Section 7.3. It's important to highlight that K_{gyro} is utilized in the expression where the hidden state variable θ is represented as a function of the gyroscope values. However, the goal is to find the inverse relationship, specifically the gyroscope value as a function of θ, which can be derived as follows:

Antenna Angular Velocity = (Scaling Factor) × (Gyroscope value - Bias error + Gyroscope noise)

Variable substitution...

$$\dot{\theta} = K_{gyro} \times (\text{gyro} - b_1 + v_1)$$

The sign of the stochastic noise v_1 is immaterial. Rearranging the terms yields Equation (12), which is restated below:

$$\text{gyro} = \frac{1}{K_{gyro}}(\dot{\theta}) + b_1 + v_1$$

7.10 EKF Results

After careful calibration of q_1, q_2 values to ensure the model is robust in estimating deviation from optimal alignment, the final selected values are 0.001 and 0.1 respectively. Because of the oscillatory nature of antenna movements, the EKF model incorporates equations that capture this specific type of motion (as seen in Equation 9). Consequently, the EKF model predicts angles that encompass both negative and positive values. However, since our goal is to ascertain the deviation from optimal alignment in any direction, the ultimate result is obtained by taking the absolute value of the EKF estimate. For Figures 86, 87, and 88, the subplots contain results from the EKF along with the absolute value for reference.

7.10.1 Almost Balanced Oscillation

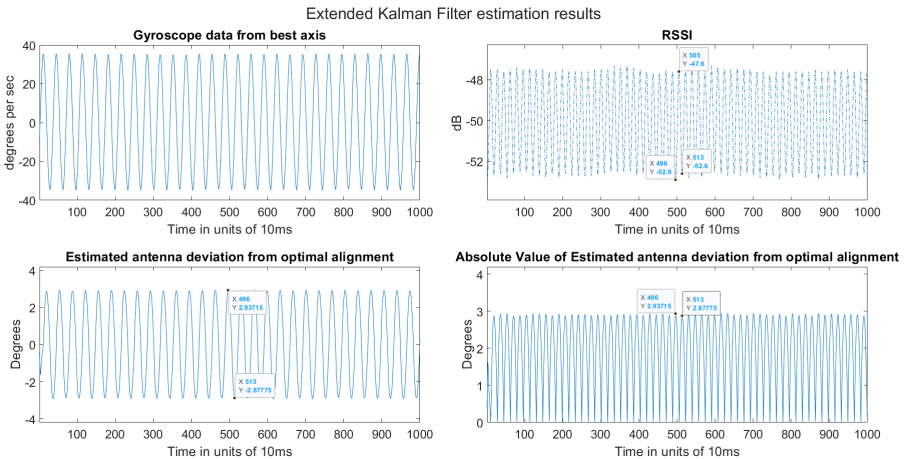

Figure 86: EKF results for almost balanced oscillation

7.10.2 Partially Balanced Oscillation

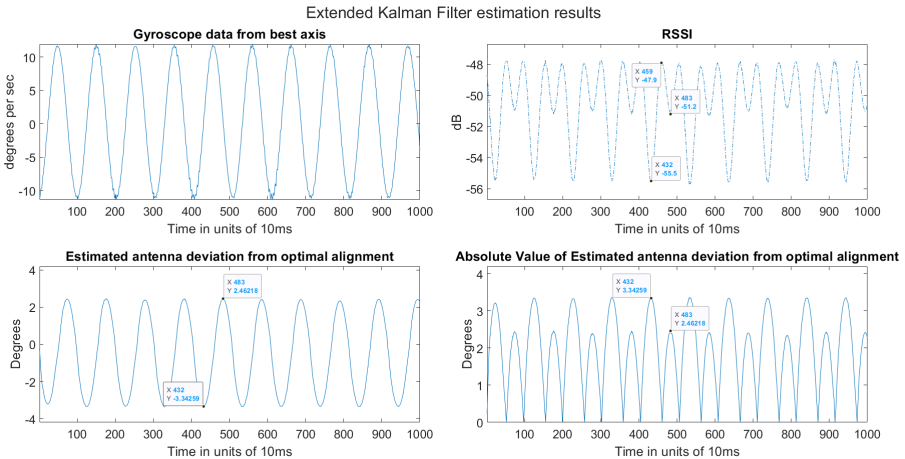

Figure 87: EKF results for partially balanced oscillation

7.10.3 Almost Unbalanced Oscillation

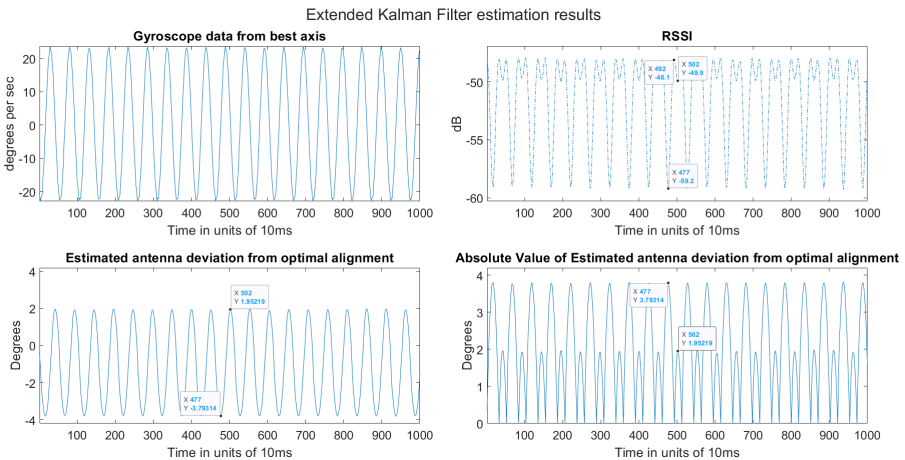

Figure 88: EKF results for almost unbalanced oscillation

Estimated vs Actual:

To obtain ground truth data for verifying the estimation accuracy, high precision equipment such as laser levels, very high-quality IMUs mounted on the antenna itself, high-quality digital leveling devices, and others are typically used. However, for the purposes of the thesis, a simpler method invovled manually determining the peaks, dips, and identifying the expected orientation of the antenna was employed. This manual approach (Section 7.8 describes how to obtain the θ from RSSI deviations) serves as a pragmatic substitute for more expensive and sophisticated measurement methods not feasible within the scope of the thesis.

Tabulating the results from plots and rounding the estimated antenna deviation to two decimal places,

Log Type	RSSI Left Dip	RSSI Peak	RSSI Right Dip	Estimated Angle	Expected Angle
Almost Balanced	-52.9	-47.6	-52.6	2.94 & 2.88	2.96 & 2.90
Partially Balanced	-55.5	-47.9	-51.2	3.34 & 2.46	3.36 & 2.49
Almost Unbalanced	-59.2	-48.1	-49.9	3.79 & 1.95	3.81 & 1.96

Table 2: Estimation results from EKF with the available gyroscope data

The largest error for the estimated angle in the above table (entry in red) is for a partially balanced scenario, RSSI Right Dip case (deviation of 0.03 degrees).

Maximum Percentage Error $= \frac{2.49-2.46}{2.46} \times 100 \approx 1.2\%$

Model performance results for the missing gyroscope data (Tx oscillation) is covered in Appendix G. The aforementioned results demonstrate exceptional accuracy with an error rate of less than 2%. However, both the model parameter estimation and the EKF were executed using the same log data. While these results are valuable for analysis purposes, they may not be practical in real-world scenarios. Parameter estimation typically requires historical data, whereas the EKF operates in real-time, utilizing live sensor data. The following section will demonstrate an attempt to mimic a practical scenario.

8 Model Parameter Estimation Using Historical Data

As mentioned earlier, it is essential to estimate the optimal model parameters from historical data. Figure 89 illustrates the sequence of steps involved in this process. When the EKF estimation is initiated, it lacks the optimal parameters for the first 11 seconds. Upon reaching the 10th second, the process for estimating the optimal EKF model parameters commences, with a designated processing time of 1 second allocated for the estimation and updating of the EKF model.

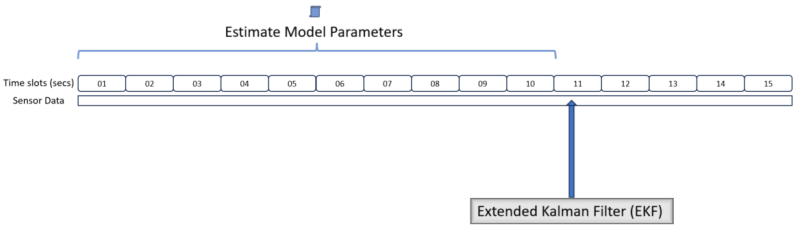

(a) Estimating EKF model parameter using samples from time = 1 to 10

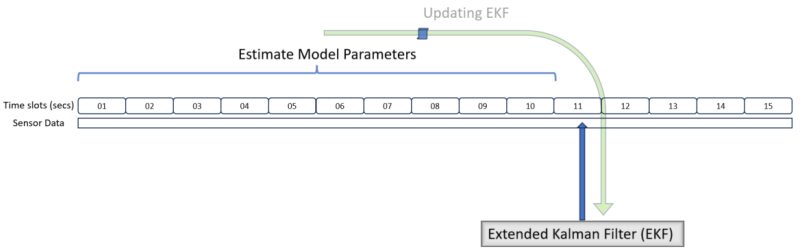

(b) Updating EKF model before t = 11

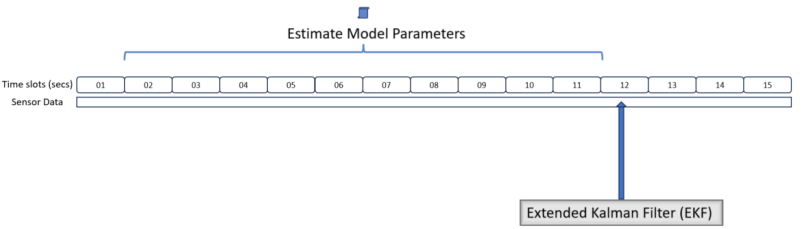

(c) New parameter estimate is initiated using samples from time = 2 to 11

Figure 89: Sliding window design

At the 11th second, the EKF incorporates all the model parameters and continues the estimation of the deviation from optimal alignment (θ). This periodic process of updating the EKF, which is currently at time $t = 11$ seconds repeats every 1 second based on estimations from $t-11$ to $t-1$ second and continues until the radio is deactivated. This continuous process of updating the EKF parameters ensures that the following parameters are periodically refined to their optimal values:

- Best correlated gyroscope selected
- K_{gyro} for optimal gyroscope scaling
- q_3 to update Allan variance for the appropriate gyroscope selected
- q_4 to update RSSI random walk variance from immediate past RSSI samples
- r_1 to update variance for the appropriate gyroscope selected
- b_1 to update bias for the appropriate gyroscope selected
- $\dot{\theta}$ to update hidden state value for the appropriate gyroscope selected

The parameters (q_1, q_2, r_2) are preserved since they remain unaffected by the gyroscope selection. Additionally, the values of the remaining hidden state variables (b_2, θ) are retained from the previous EKF estimate.

The recommended design suggests allocating one second for estimating optimal model parameters, but this duration can be shortened depending on the processing capabilities of the radio. Additionally, there's the option of processing the data externally, as historical data samples can be stored externally as well. This external processing provides the flexibility to utilize higher processing power, but it's important to consider the latency involved in transferring the estimated parameters back to the radio.

Fortunately, the transfer of only 7 model parameters should not incur significant time delays, especially when there is a dedicated link between the external processing unit and the radio.

Evaluating the model's performance in a scenario that closely resembles practical implementation provides a more insightful perspective on any potential limitations. In this context, the antenna-radio system was separated from the mast sway generator system and mounted on an independent pole, situated at a height of approximately 12 feet (Figure 90). The pole's stiffness was notably high, leading to minimal swaying due to natural wind forces. To induce swaying along two distinct axes, manual intervention was employed to induce mast swaying.

Figure 90: Mounting antenna-radio system on a pole

To elucidate the functioning of parameter estimation and EKF results, one instance of manually induced pole oscillation is examined in this section. In contrast to the previously discussed 10-second logs, this analysis encompasses a longer duration log spanning 100 seconds. As a consequence, the figure may appear compressed due to the increased number of data points presented within the same figure size.

In Figure 91, points signifying the commencement of manual pole excitation to induce oscillation have been marked. These excitations were manually initiated, resulting in a rapid increase in the oscillation amplitude. Subsequently, the pole was allowed to gradually dissipate energy and reduce oscillation amplitude. This cyclic process was repeated four times, with new excitations occurring at approximately 6 seconds, 28 seconds, 47 seconds, and 74 seconds from the start of logging, as indicated in the RSSI subplot.

Furthermore, the gyroscope plots reveal that the most significant excitation occurred along the Z-axis, X-axis, X-axis, and Z-axis sequentially, corresponding to the four excitation events. Intermediate plots including K_{gyro} estimation, filtering, synchronization, and other recurring processes have been omitted from this section since they occur at 1-second intervals. Instead, the final estimation plot (Figure 92), accompanied by its analysis, is presented for clarity and conciseness.

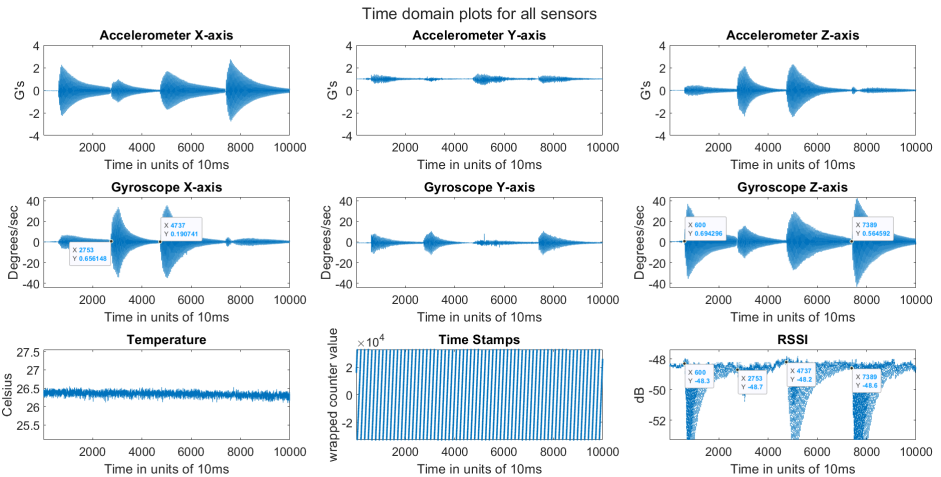

Figure 91: Sensor data with excitation on two axes

To initiate the filtering process, a default setting is required as the estimation of model parameters has not yet been performed. In this case, the default configuration selects the gyroscope X-axis for setting some of the initial parameters. The specific details are provided below:

- $K_{gyro} = 1$
- $b_1 = 0.1$ (Bias error value for gyroscope X-axis from stationary data)
- $b_2 = RSSI(1)$ (First value of RSSI)
- $\theta = 0$
- $\dot{\theta} = G(1) - b_1$ (First value of gyroscope X-axis without bias error)
- $q_1 = 0.001$ (Calibrated value)
- $q_2 = 0.1$ (Calibrated value)
- $q_3 = 6.76 \times 10^{-6}$ (Allan variance for gyroscope X-axis)
- $q_4 = q3$ (Setting to same value as q_3 due to lack of historical RSSI data)
- $r_1 = 6.9 \times 10^{-4}$ (Variance value for gyroscope X-axis from stationary data)
- $r_2 = 23.5 \times 10^{-4}$ (Variance value for RSSI from stationary data)

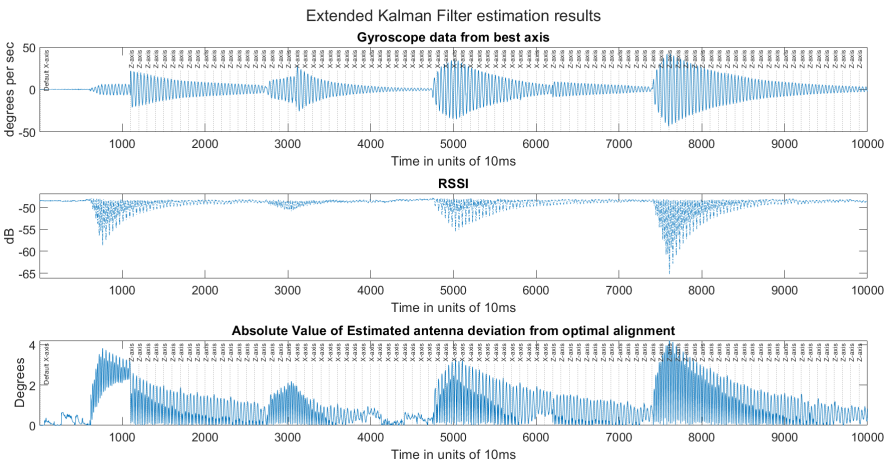

Figure 92: Estimation results from the EKF

As previously clarified, the initial 11 seconds of the data log lack any model parameter estimates. At the 11th second, the gyroscope Z-axis was identified as the best-correlated gyroscope with RSSI, and the relevant model parameters were updated (a list of these parameters is provided following Figure 89). The subsequently selected axis for each second is elaborated upon in the subplots of Figure 92. In this log, the primary focus will be on conducting a comprehensive analysis of the overall model performance, without delving into a comparison between the estimated θ and the expected θ.

Upon analyzing Figure 91, it becomes evident that a shift to a different axis (after the initial shift at 11th second) should have taken place after approximately 29 seconds, but it actually occurs at around 31 seconds when the model shifts to the X-axis. This can be attributed to the 1 second delay in processing and updating model parameters.

The subsequent shift was expected around 73 seconds but, surprisingly, occurs at 62 seconds instead. At approximately 47 seconds, both the X-axis and Z-axis experienced excitations, with the X-axis exhibiting a higher degree of excitation. However, the excitations on the X-axis dissipate more rapidly compared to those on the Z-axis. This discrepancy may be attributed to a possible lower degree of freedom or higher resistance at the focal point rotation along the X-axis as compared to the Z-axis.

Around the 40-second and 60-second marks, the excitations recorded from the gyroscope are notably low, which hinders the model's accuracy in estimating the hidden state values. This phenomenon can be attributed to the effects of drifting, especially when the data lacks significant oscillatory motion.

The analysis presented underscores a noteworthy observation: despite the rapid and dynamic changes in the direction of oscillation, the feature extraction process from historical data showcases the model's remarkable proficiency in selecting the most suitable axis and consistently updating the model parameters with the optimal estimates. This holds true as long as the system experiences reasonably significant excitations.

9 Predicting Future State Values

The last crucial component in ensuring the practicality of the research outcomes from this thesis involves the capability to predict θ in advance and implement proactive measures, such as adaptive control, to alleviate the effects of antenna misalignment variations. To successfully implement these proposed methods, it is imperative to transmit state information to the transmitter side.

These adaptive techniques may not completely eliminate the problem but instead temporarily reduce the required channel capacity for transmitting user data over that link. This reduction can be accomplished by decreasing the modulation order and/or introducing redundancy into data traffic. By reducing the necessary channel capacity, the radio system can prevent the need for retransmitting data packets that might otherwise fail during periods of lower received signal power during misalignment.

Lowering the required channel capacity can have an impact on performance during peak data traffic instances. However, it's worth considering that data traffic often exhibits a bursty nature, as highlighted in prior research [36]. With the application of time-series-based approaches, it may become feasible to schedule high-traffic periods during moments of near optimal alignment and delay or reduce the traffic during periods of misalignment, thereby optimizing system performance.

Additional methods encompass increasing transmitter power or rerouting traffic through alternative links. Due to unsatisfactory results from the thesis concerning the prediction of future state values, this section remains incomplete and offers an opportunity for further research and investigation.

10 Conclusion

The study was initiated by outlining the challenges inherent in backhaul systems utilizing parabolic antennas, primarily attributed to the narrower beams at higher frequencies. Notably, Ericsson has ongoing research studies involving the installation of IMU sensors directly on the antenna, and enabling the steering of the feed direction based on antenna movements. In contrast, this thesis delves into alternative and cost-effective approaches for estimating antenna movements. Instead of placing the IMU on the antenna, it is positioned on the radio equipment. However, the radio and antenna are intimately connected via the waveguide. The thesis has further delved into the challenges associated with this approach and provides insights into the processes involved in simplifying the problem for analysis and designing the EKF model.

Given the variability in the frame of reference between the antenna and the IMU mounted on the radio, an innovative approach has been adopted: utilizing cross-correlation between the RSSI data and the IMU sensor data. This approach facilitates the selection of the most suitable gyroscope for updating the model parameters. Section 7 commences by providing an overview of the Extended Kalman Filter (EKF) model, followed by an elaboration of the approximations and assumptions necessary to enable the model to estimate antenna movements accurately. The section then systematically guides through the estimation of various model parameters from sensor and RSSI data. The final outcomes of this process are consolidated in Table 2.

While the obtained results instill confidence in the design and implementation of the EKF model, addressing its practicality is the central focus of Section 8. This section illustrates how historical data can be effectively leveraged to periodically estimate the model parameters while the EKF operates in real-time using sensor and RSSI data. The analysis in this context is not centered around comparing the expected and estimated deviations from the optimal alignment. Instead, it focuses on the sliding window design and the model behavior when processing logs with excitations occurring on different gyroscope axes.

The proposed model demonstrates remarkable proficiency in accurately estimating antenna deviations from optimal alignment across a spectrum of frequencies and oscillation patterns, underscoring its inherent robustness. It's worth noting that compared to the utilization of an IMU sensor directly attached to the antenna, the primary tradeoff lies in the model's inability to precisely ascertain the specific orientation of antenna misalignment, be it horizontal or vertical.

While exercising caution, it is imperative to subject the model to rigorous testing employing authentic datasets, as opposed to relying solely on a mast sway generator or manually induced mast swaying. In the pursuit of transforming this concept into a production-ready solution, a logical progression entails incorporating IMU sensors into a greater number of radios, thereby amassing data from networks most susceptible to the effects of mast swaying. Through the utilization of the proposed methodologies for estimating anticipated deviations from peak and, potentially, through iterative refinement of the model, the prospect of a universally applicable solution becomes increasingly feasible.

Within the scope of this thesis, several areas were deliberately omitted, nevertheless, they remain ripe for prospective exploration. Chief among these is the imperative to validate the model under authentic real-world mast swaying circumstances, encompassing a diverse array of antenna types distinguished by varying frequencies and dimensions. Expanding this ambit further, there is potential to tackle scenarios where swaying impacts both ends of the communication link, occurring asynchronously. Such scenarios might necessitate additional model states to effectively accommodate heightened complexity. Additionally, the extension of the model to encompass XPIC-type antenna-radio systems would eventually become a requisite step, ensuring comprehensive coverage across all plausible antenna-radio configurations.

Ultimately, as the model's predictive capabilities continue to advance, it becomes conceivable to contemplate the expansion of research into the development of intelligent adaptive power control mechanisms or baseband coding strategies. These innovations could proactively address RSSI degradation resulting from the dynamic movement of antennas, thereby enhancing the efficiency of the communication link in the face of highly dynamic scenarios.

Appendix A The Impact of the Antenna Feed Shift on the Radiation Pattern

For narrow beam radiation pattern, antenna orientation change will have much larger impact on the radiation pattern as compared to antenna feed positional shift. It is important to keep in mind the limits of this assumption and two cases with numerical calculations are covered below. As shown in Figure 93, a rotation around a focal point located away from the antenna center will result in antenna feed positional change along with the orientation change.

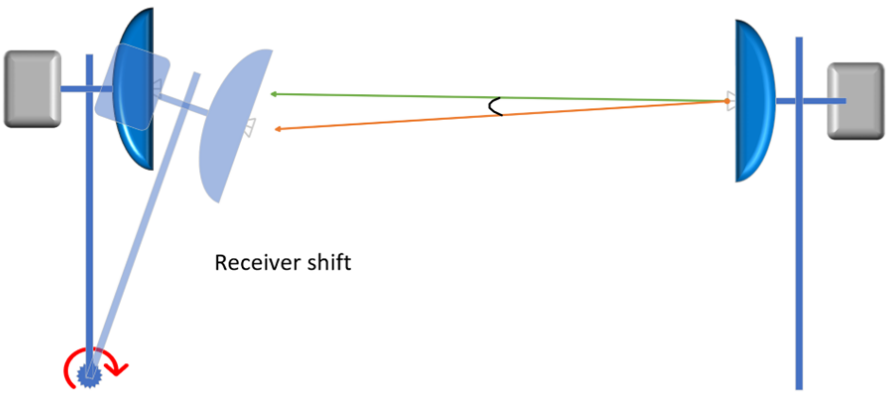

Figure 93: Antenna feed positional change due to rotational movements

Figure 93 can be simplified to Figure 94, where

H_M : Mast Height
Θ_M : Mast Rotation Angle
D_M : Distance between Tx and Rx Feed
a : Feed Height change due to rotation
b : Distance between Tx and Rx change due to rotation
Φ : Deviation from optimal LoS path due to feed positional change

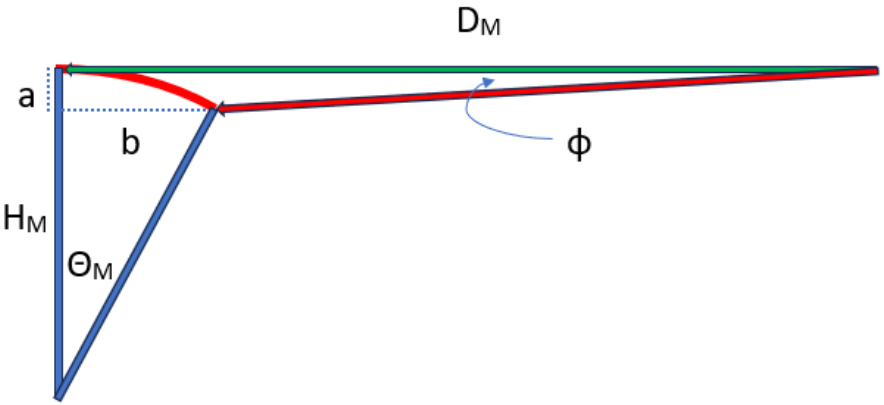

Figure 94: A simplified representation of Figure 93

Applying simple geometry,

$a = H_M - H_M \cos(\Theta_M)$

$b = H_M \sin(\Theta_M)$

$\Phi = \arctan(\frac{a}{D_M - b})$

Case 1: Short mast with large distance between Tx-Rx

$H_M = 5m, D_M = 2000m, \Theta_M = 5°$
$\Phi \approx 0.0005°$

Most cases including the current antenna-radio configuration will observe the similar outcome, and hence the impact due to antenna feed positional change can be ignored.

Case 2: Tall mast with short distance between Tx-Rx

$H_M = 20m, D_M = 100m, \Theta_M = 5°$

$\Phi \approx 0.044°$

A 60cm antenna operating at 80 GHz spectrum has very short range and a narrower beam. As per the antenna specifications for this antenna type, there is -6.35 dB relative gain for 0.25° angle. Approximate intrapolation gives us about -1 dB relative gain for 0.044° which is not negligible. The impact of this to the estimation accuracy of the proposed model is beyond the scope of the thesis, and will require a new antenna-radio system to perform the necessary data collection and model verification.

Appendix B Register Values and Settings

Register Name	Register Number (in Hex)	Read/Write	Register Value (in Binary)
WHO_AM_I	0x0F	Read	NA
CTRL1_XL	0x10	Write	0b01011000
OUTX_L_A	0x28	Read	NA
OUTY_L_A	0x2A	Read	NA
OUTZ_L_A	0x2C	Read	NA
CTRL2_G	0x11	Write	0b01010000
OUTX_L_G	0x28	Read	NA
OUTY_L_G	0x2A	Read	NA
OUTZ_L_G	0x2C	Read	NA
CTRL10_C	0x19	Write	0b00100000
OUT_TEMP_L	0x20	Read	NA
TIMESTAMP0	0x40	Read	NA

Table 3: IMU sensor register details

Note1 : The SAD[0]/SA0 pin was grounded for provided Ericsson radio.

Note2 : In the context of simulated mast sway at approximately 5 Hz, the accelerometer readings exhibit a variation within the range of ±1.5 G. Given that gravity itself contributes 1 G, the accelerometer can potentially register a maximum of 2.5 G. Consequently, it is essential to adjust the accelerometer's full-scale selection value to ±4 G, deviating from the default setting of ±2 G, to accommodate the expected range of motion.

Note3 : Gyroscope full-scale selection value is set to ± 250 dps (degrees per second) as opposed to the default value of ± 125 dps. Given a maximum frequency of sway at 5 Hz, the gyroscope measurements consistently stay below 70 dps. However, it's advisable to incorporate some additional margins for enhanced reliability and robustness.

Note4 : The process of collecting sensor data and consolidating it into a unified structure for transmission over USB occurs at a regular interval of 10 ms, corresponding to a frequency of 100 Hz. This process has been assigned the lowest priority, making it readily interruptible by any higher-priority scheduled processes with the radio. To ensure that a unique sensor reading is available every 10 ms while accounting for timing buffers, a sensor update rate of 208 Hz was chosen instead of 104 Hz.

Note5 : Register readings follow little endian format.

Appendix C Methodology to Verify Low Multipath Impact on the Antenna Radiation Pattern

(a) Obstruction in antenna view (b) No obstruction in antenna view

Figure 95: Antenna view for different positions

(a) Perspective view (b) Digital leveling device

Figure 96: Verifying radiation pattern accuracy

As depicted in Figure 96a, it's evident that the obstruction is not within the antenna's line of sight. To ensure the alignment of the antenna specification with the observed radiation pattern, measurements can be conducted using a digital leveling device, as illustrated in Figure 96b. This device has a margin of error of $\pm 0.2°$. Furthermore, Figure 97 highlights the potential impact of diffraction on the radiation pattern, as the signal strength increases or decreases when the antenna rotates toward a solid object that lies outside the line of sight path.

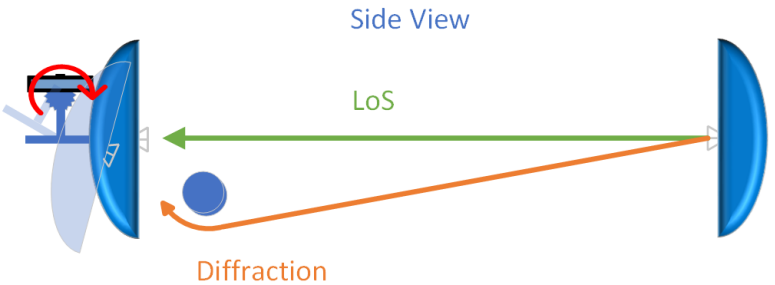

Figure 97: Diffraction of Tx signal around object

To fine-tune the antenna for a nearly balanced oscillation, RSSI variations are monitored over a 10-second window of logs. Necessary adjustments were then applied to achieve the desired balanced oscillation pattern, resembling what is depicted in Figure 19. It may require a few iterations to reach the optimal configuration for achieving this balanced oscillation. Once this configuration is established, key orientation points of interest are identified, such as the antenna's orientation during each dip and peak while subjecting the antenna to motor induced oscillation. To achieve this, real-time measurements must be meticulously observed, and the motor operation should be halted when nearing these critical points for accurate documentation.

These interruptions occurred at both the extremes of the oscillations, where the RSSI exhibited dips (as illustrated in Figure 66), corresponding to "Low Angle" and "High Angle". These orientations represent the local minima in the RSSI variation. Additionally, the motor was paused at the peaks of oscillation, corresponding to the "Mid Angle". An example of such an almost balanced oscillation case is provided in Table 4, which demonstrates approximately equal angle intervals from the peak to the dips. All measurements and calculations have been rounded to two decimal places, and all measurements are expressed in degrees.

Sr.No.	1	2	3	4	5	6	7	8	9	10
Low Angle	56.8	56.8	56.8	56.9	56.8	56.8	56.8	56.9	56.7	56.9
Mid Angle	59.2	58.8	58.6	59.3	58.8	58.8	59.0	59.0	58.7	59.0
High Angle	61.4	61.3	61.4	61.4	61.4	61.4	61.4	61.4	61.4	61.5
Sr.No.	**11**	**12**	**13**	**14**	**15**	**16**	**17**	**18**	**19**	**20**
Low Angle	56.9	56.8	56.8	56.9	56.9	56.8	56.8	56.7	56.8	56.8
Mid Angle	58.9	58.6	59.4	58.8	59.1	58.8	59.0	58.9	59.2	58.8
High Angle	61.4	61.4	61.3	61.3	61.4	61.3	61.2	61.4	61.3	61.4

Table 4: Table of manual angle measurements for almost balanced oscillation

Average Low Angle ≈ 56.82
Average Mid Angle ≈ 58.94
Average High Angle ≈ 61.37

Mid Angle to Low Angle $= 58.94 - 56.82 = 2.12$
High Angle to Mid Angle $= 61.37 - 58.94 = 2.43$

Peak Angle Deviation Error $= \frac{(2.43-2.12)}{2} = 0.16$

Estimated Peak Angle $\approx 58.94 + 0.16 = 59.1$. To further test the results, the antenna oritentation was adjust by 1.08 degrees, to achieve a partially balanced oscillation.

Sr.No.	1	2	3	4	5	6	7	8	9	10
Low Angle	55.9	55.8	55.8	55.8	55.9	55.8	55.9	55.8	55.8	55.9
Mid Angle	60.4	60.4	60.5	60.5	60.4	60.4	60.4	60.5	60.5	60.5

Table 5: Table of manual angle measurements for partially unbalanced oscillation

Average Low Angle ≈ 55.84
Average High Angle ≈ 60.45

Est. Mid Angle to Low Angle $= 59.10 - 55.84 = 3.26$
High Angle to Est. Mid Angle $= 60.45 - 59.10 = 1.35$

offset-angle ≈ 0.96 (actual value 1.08)

The results indicate that the antenna is following the radiation pattern within the limits of human error and the measuring device margin of error.

Appendix D Frame of Reference Between the IMU and the Antenna

The thesis operates on the premise that the frame of reference between the IMU and the antenna is not initially known. However, if there is a requirement to precisely ascertain this relationship, particularly for the implementation of a specific corrective solution tailored to a particular antenna-radio configuration, this section offers a description of how to establish the relationship for that specific configuration. Given that the IMU sensor is not physically situated on the antenna itself, a transformation matrix that defines the relationship between the IMU sensor's frame and the orientation of the antenna needs to be determined. In the context of the provided radio and antenna setup, the directional axes are clearly illustrated in Figure 98.

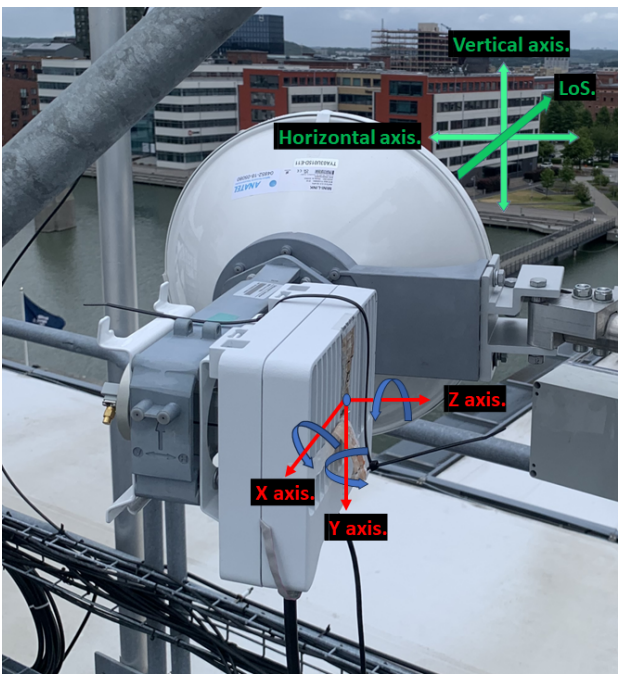

Figure 98: IMU accelerometer and gyroscope axis in relation to antenna axis

As evident from the figure, it's notable that the gyroscope's Z-axis aligns with the antenna's oscillation along the vertical axis, while the gyroscope's Y-axis corresponds to the antenna's oscillation along the horizontal axis. However, it's worth mentioning that the gyroscope's X-axis corresponds to polarization shift, a factor that will not be addressed within the scope of this thesis, as the radio can only measure a single RSSI value along the most prominent polarization angle.

Appendix E Bias and Variance From Stationary Data

Log	Gx Bias	Gy Bias	Gz Bias	Gx Var	Gy Var	Gz Var	RSSI Var
Log1	0.1047	-1.069	0.3124	8.42E-04	8.23E-04	0.0012	0.0025
Log2	0.1144	-1.0416	0.3444	7.32E-04	9.97E-04	7.46E-04	4.77E-04
Log3	0.1106	-1.0306	0.3342	0.0016	0.0014	6.18E-04	0.0022
Log4	0.0974	-1.1221	0.3319	7.55E-04	0.0031	0.0021	NA
Log5	0.1055	-1.0919	0.3572	6.73E-04	9.05E-04	6.14E-04	NA
Log6	0.1122	-1.0549	0.3564	6.75E-04	9.51E-04	6.25E-04	NA
Log7	0.0953	-1.2153	0.3013	6.77E-04	0.001	6.32E-04	NA
Log8	0.1027	-1.1298	0.3425	6.76E-04	0.0011	6.14E-04	NA
Log9	0.1011	-1.1635	0.3155	6.71E-04	8.97E-04	6.11E-04	NA

Table 6: Summary of stationary logs

Log information:
Log1 - Time Stamp : 05_17_13_20_57, Duration : 3000 seconds
Log2 - Time Stamp : 05_17_16_26_25, Duration : 3000 seconds
Log3 - Time Stamp : 05_17_15_24_43, Duration : 3000 seconds
Log4 - Time Stamp : 05_18_23_20_06, Duration : 15000 seconds
Log5 - Time Stamp : 05_19_15_40_45, Duration : 15000 seconds
Log6 - Time Stamp : 05_19_09_58_44, Duration : 15000 seconds
Log7 - Time Stamp : 05_20_19_52_54, Duration : 30000 seconds
Log8 - Time Stamp : 05_19_21_32_37, Duration : 30000 seconds
Log9 - Time Stamp : 05_20_10_02_46, Duration : 30000 seconds

Correcting bias in accelerometer data poses a challenge, primarily due to the influence of gravity and potential misalignment issues. Similarly, mitigating bias in RSSI data is a complex task, even when utilizing a direct signal feed from a signal generator, as it can be affected by cable and connector losses.

Since the accelerometer data is not utilized in the final model, it has been omitted from our analysis. The primary focus lies on the gyroscope data and the variance in RSSI. Our data was sampled at a rate of 100 Hz, and instances marked as "NA" for RSSI values indicate the absence of RSSI data in a particular stationary log. A log duration of 30000 seconds, sampled at 100 Hz, corresponds to a total of 3000000 data points.

After excluding outliers (indicated in red within Table 6), a final set of averaged values is calculated. For these values, the bias is rounded to two decimal places and the variance is represented using a negative fourth power.

- Gyroscope X-axis bias : 0.10
- Gyroscope Y-axis bias : -1.14
- Gyroscope Z-axis bias : 0.33
- Gyroscope X-axis variance : 6.9×10^{-4}
- Gyroscope Y-axis variance : 9.8×10^{-4}
- Gyroscope Z-axis variance : 6.2×10^{-4}
- RSSI variance : 23.5×10^{-4}

While it's important to note that RSSI variance can be influenced by the quality of the signal generator and might not always precisely reflect the receiver's inherent characteristics, these values will still be incorporated into the final EKF model.

Additionally, for the model's gyroscope bias random walk variance estimation, Allan variance [37] can be utilized and can be computed from the stationary data. The Allan deviation, extracted from the logs with the greatest number of samples and longest duration, is visually presented in Figure 99.

In the plots, the line denoted by σ_N represents a line passing through $\tau = 1$ and with a slope of 0.5, signifying the angle random walk. Across all three logs (05_20_10_02_46/05_19_21_32_37/05_20_19_52_54), the deviation values for the three gyroscopes are identical. The EKF model utilizes the Allan variance, calculated as the square of the Allan deviation. The numerical values extracted from the plots are as follows:

- Gyroscope X-axis Allan variance with angle random walk : 6.76×10^{-6}
- Gyroscope Y-axis Allan variance with angle random walk : 7.84×10^{-6}
- Gyroscope Z-axis Allan variance with angle random walk : 5.76×10^{-6}

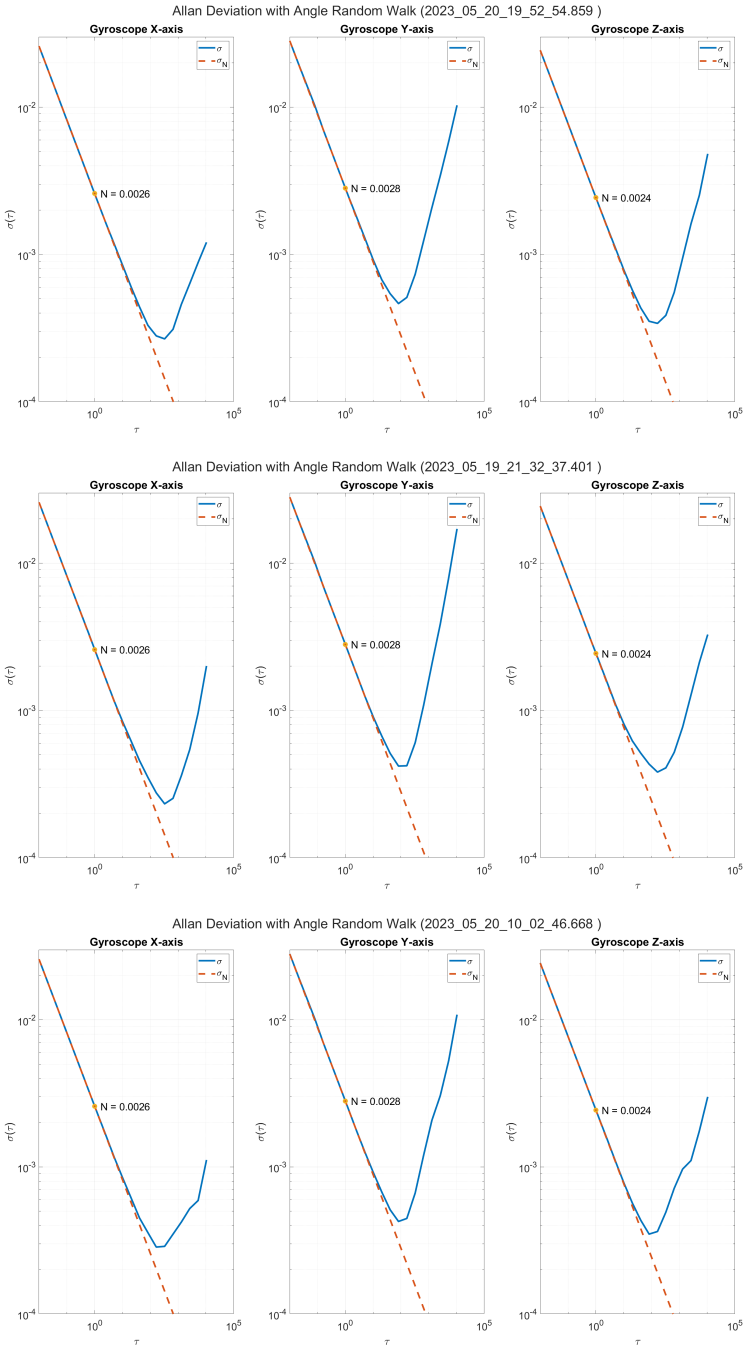

Figure 99: Allan deviation with angle random walk for multiple stationary logs

Appendix F Understanding 2nd Order Differential Equation

Numerous pieces of literature, such as [38] and [39], delve into the study of mechanical oscillations, offering various equations to capture their behaviors. Below is a selection of representations (as seen in Table 2-3 from [39]):

Rectilinear system

$$m\ddot{x} + c\dot{x} + kx = T(t)$$

Rotational system

$$J\ddot{\theta} + c\dot{\theta} + k\theta = F(t)$$

Equation (9), is similar to above equations except for the normalized mass ($m = 1$) or moment of inertial ($J = 1$)

Equation in terms of damping factor ζ and natural frequency ω, with external force or torque set to 0 (Equation (2-28) from [39]) :

$$\ddot{x} + 2\zeta\omega\dot{x} + \omega^2 x = 0 \tag{21}$$

where $\omega = 2\pi f$; f is the frequency of oscillation, and ζ is the damping ratio.

Upon direct comparison of Equation (9) with Equation (21), the following equalities can be established:

$$\alpha = 2\zeta\omega \tag{22}$$

$$\beta = \omega^2 \tag{23}$$

w_2 can be ascribed to an external force that will cause oscillations that are not balanced.

To elucidate each term within the proposed 2nd order differential equation, simulation results obtained using Julia [40] will be leveraged. In the forthcoming pages, three distinct cases, each characterized by a unique set of parameters $(\alpha, \beta, \mathrm{w}_2)$ will be elaborated upon.

Julia Source Code:

```
using OrdinaryDiffEq, Plots

#Parameters
α = 0
β = 10
w₂ = 0

#Initial Conditions
u₀ = [0,π]
tspan = [0.0,10.0]

#Define the problem
function harmonicoscillator(du,u,p,t)
    θ = u[1]
    dθ = u[2]
    du[1] = dθ
    du[2] = - α*dθ - β*θ + w₂
end

#Pass to solvers
prob = ODEProblem(harmonicoscillator, u₀, tspan)
sol = solve(prob, Tsit5(),saveat=0.01)
```

Summary of the above code:
The function *harmonicoscillator* defines the 2nd order differential problem, by defining two states namely $\dot{\theta}$ and θ represented as $u[1]$ and $u[2]$ respectively. $du[2]$, the derivative of $\dot{\theta}$ is same as the 2nd derivative of θ termed as $\ddot{\theta}$. Equation (9) is coded in the last line of the function (move all terms except $\ddot{\theta}$ to the right of $=$).

The initial value of the two states are specified as u_0 in the code, and are required as the starting values for the problem solver. The total duration of the simulation is 10 seconds (*tspan*) with a sampling period of 0.01 second (*saveat*). The kind of solver selected is not particularly important as the simulation is to understand the behaviors of 2nd order differential equations. To complete the description of the code, the type of problem solver selected is the Tsitouras 5/4 Runge-Kutta method [41] ($Tsit5()$).

Case1: Undamped balanced oscillation

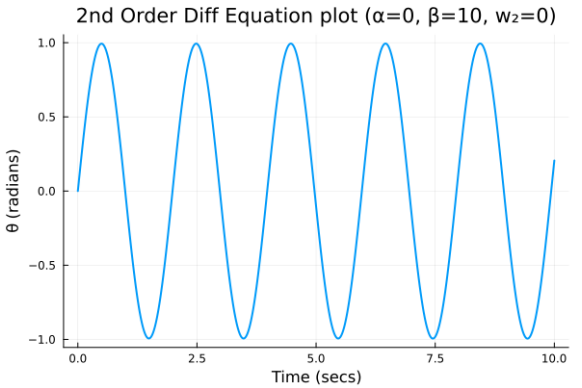

Figure 100: Simulation plot for balanced oscillation

If the frequency of oscillation is known, β can be determined (using Equation (23) and substituting ω).

$$\beta = (2\pi f)^2 \tag{24}$$

To validate the above relationship, two cases are simulated. As shown in Figure 100, the frequency of oscillation is a little higher than 0.5 which matches the theoretical value ($\frac{1}{2\pi}\sqrt{10} \approx 0.5033$) given $\beta = 10$. Another example (Figure 101), where $\beta = 20$, the frequency of oscillation a little over 0.7 and matches the threoretical value of ≈ 0.7118.

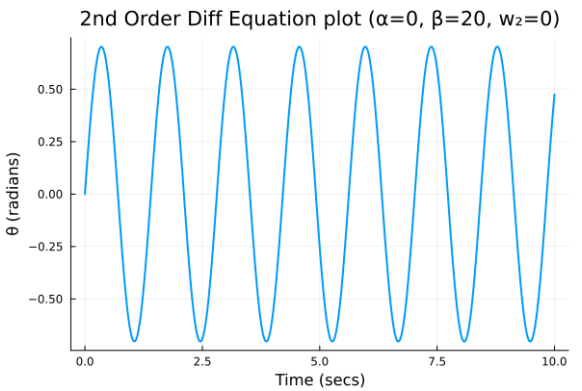

Figure 101: Simulation plot for balanced oscillation (doubling β)

Case2: Undamped unbalanced oscillation

By introducing a non-zero value for w_2, the center of oscillation is shifted away from zero. As depicted in Figure 103, the difference between the absolute values of the minimum and maximum points is approximately -2. This oscillation pattern resembles what is commonly referred to as a partially unbalanced oscillation, where the antenna's oscillations are not evenly distributed on both sides of the optimal orientation. This behavior can be mathematically expressed as follows:

$$MinMaxDiff = \frac{2 \times w_2}{\beta} \tag{25}$$

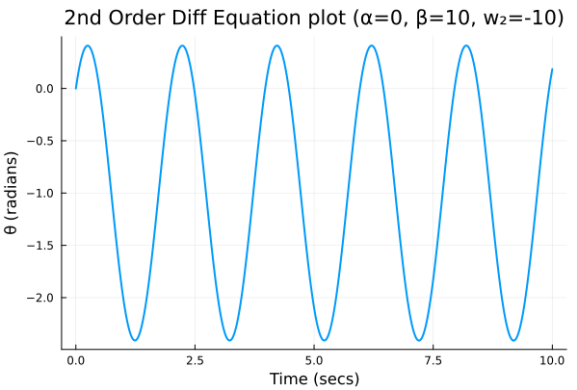

Figure 102: Simulation plot for balanced oscillation and non-zero mean

Since the mid-point or the difference between extremes for an unbalanced oscillation (Section 7.8) can be estimated, the value of w_2 can be determined from Equation (25), and expressed in degree scale. The MinMaxDiff is same as twice the offset-angle (ϕ).

$$w_2 = \beta \times \phi \tag{26}$$

Case3: Damped balanced oscillation

For a damped oscillation, α will be non-zero.

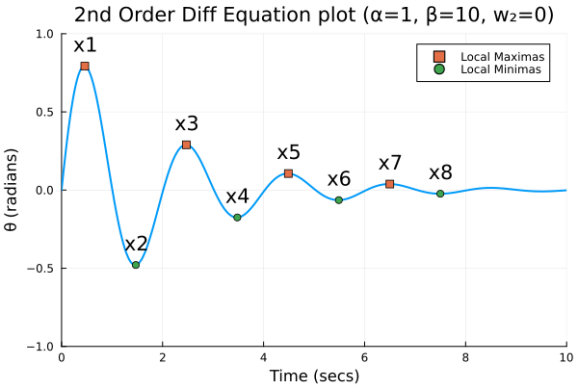

Figure 103: Simulation plot for balanced oscillation with decay

The local maximas or minimas can be used to determine the damping ratio (ζ) which in turn will give α. The equation for logarithmic decrement δ can be expressed in multiple ways, some listed below:

$$\delta = \underbrace{\log_e \frac{x_1}{x_3} = \ln \frac{x_3}{x_5} = \ln \frac{x_5}{x_7}}_{\text{log ratio of adjacent maximas}} \tag{27}$$

$$= \underbrace{\ln \frac{x_2}{x_4} = \ln \frac{x_4}{x_6} = \ln \frac{x_6}{x_8}}_{\text{log ratio of adjacent minimas}} \tag{28}$$

$$= \underbrace{\ln \frac{x_1 - x_2}{x_3 - x_4} = \ln \frac{x_3 - x_4}{x_5 - x_6} = \ln \frac{x_5 - x_6}{x_7 - x_8}}_{\text{log ratio of adjacent max-min differentials}} \tag{29}$$

The maximas/minimas can be determined by observing the RSSI oscillation data and selecting the maximum/minimum dip respectively. Having estimated δ, the damping factor ζ can be calculated (Equation (3-12) from [39]).

$$\zeta = \frac{\delta}{\sqrt{\delta^2 + (2\pi)^2}} \tag{30}$$

Having determined ζ, α can be determined using Equation (22)

Appendix G Model Performance When Tx Antenna Oscillates Instead of Rx

This section follows from understanding the model described in Section 7.3. Due to the unavailability of gyroscope data to represent Tx antenna movements and correlate with RSSI data, several steps in the model parameter estimation cannot be performed.

- Selecting the most suitable gyroscope
  In instances where gyroscope data is unavailable, the option to identify the gyroscope signal with the strongest correlation to the RSSI data is not viable. Consequently, parameter q_3 is configured to 0, while b_1 is assigned a non-zero small random value. Choosing a value of zero for b_1 results in a collapse in matrix multiplication, leading to a constant hidden state estimate of 0, irrespective of the RSSI value.

- Feature extraction
  The unavailability of gyroscope data renders it impossible to discern the extremes of the oscillation. The absence of the means to detect dips hampers the identification of triplets required for the feature extraction.

- Estimating the offset-angle
  In the absence of triplets, the determination of the offset-angle becomes unattainable. Fortunately, this aspect is not essential for the EKF model; it solely serves the purpose of validating estimation outcomes. Manual observation will be employed to verify the accuracy of the estimations.

- Estimating gyroscope scaling factor
  In the absence of zero-cross information from the gyroscope data, the calculation of the scaling factor becomes unfeasible. As a result, the parameter K_{gyro} is set to 1.

- β value
  In the absence of gyroscope data to guide the antenna deviations in a consistent cyclic pattern, adjusting the β value to correspond to a potential gyroscope frequency can enhance the model's resilience to the missing gyroscope data. To reiterate, the RSSI data encompasses two frequency components for all oscillations that aren't perfectly balanced. One possible component matches the gyroscope frequency, while the other, usually stronger component is twice the gyroscope frequency. In the case of a balanced oscillation, only the frequency component that is twice the gyroscope frequency exists. Through the utilization of DFT and selecting prominent peaks via outlier detection using a threshold based on percentiles, it's feasible to identify the RSSI frequency component without prior knowledge of the gyroscope frequency component. Leveraging this information, β can be computed.

In conjunction with the prescribed model parameter configurations outlined above, it's necessary to adjust r_1 to a high value (e.g. 10). This modification ensures that the model prioritizes adjusting the hidden state variables to coverge the model output variable values more closely to the RSSI values instead of the gyroscope values.

In summary, to simulate this scenario, all gyroscope sensor data can be set to zero, and the model parameter values should be adjusted as follows:

$$
\begin{aligned}
q_3 &= 0 \\
b_1 &= 1 \text{ (any small random value will work)} \\
K_{gyro} &= 1 \\
r_1 &= 10 \\
\beta &= (2\pi f)^2 \text{ where } f = \text{Half the RSSI frequency for balanced oscillation}
\end{aligned}
$$

All three scenarios, covered in Section 7.10 are repeated here with the exact same model parameter configuration except for β as it is a function of the RSSI frequency.

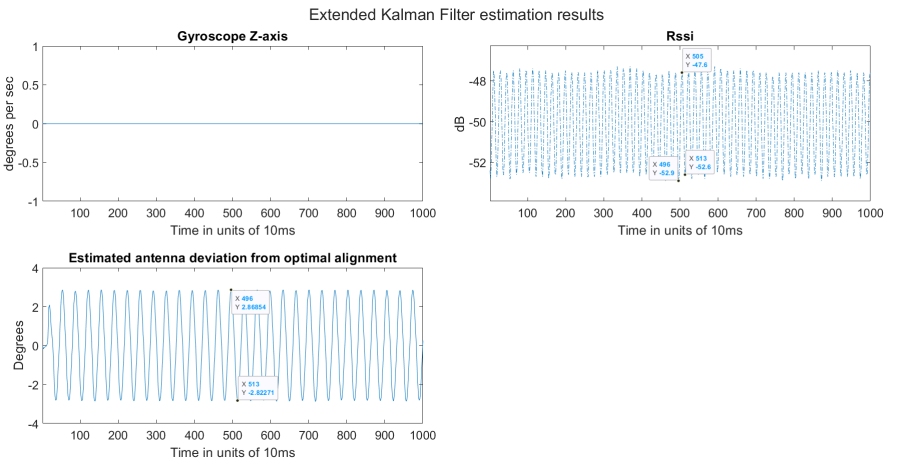

Figure 104: Kalman filtering results for almost balanced oscillation with no gyroscope data

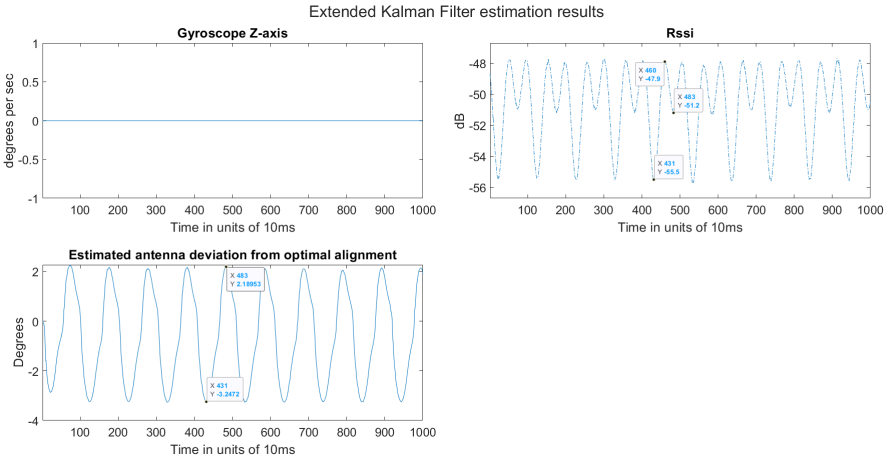

Figure 105: Kalman filtering results for partially balanced oscillation with no gyroscope data

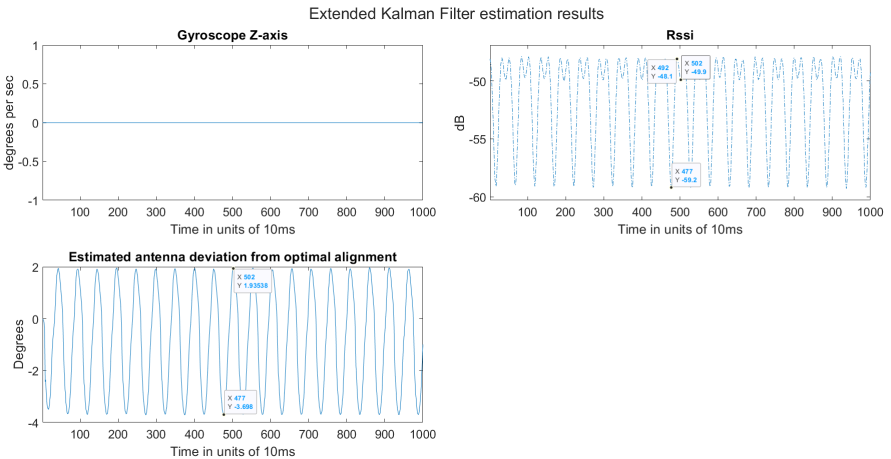

Figure 106: Kalman filtering results for almost unbalanced oscillation with no gyroscope data

Log Type	RSSI Left Dip	RSSI Peak	RSSI Right Dip	Estimated Angle	Expected Angle
Almost Balanced	-52.9	-47.6	-52.6	2.87 & 2.82	2.96 & 2.90
Partially Balanced	-55.5	-47.9	-51.2	3.25 & 2.19	3.36 & 2.49
Almost Unbalanced	-59.2	-48.1	-49.9	3.70 & 1.94	3.81 & 1.96

Table 7: Estimation results from EKF with no gyroscope data

Compared to the results shown in Table 2, the error is higher without the gyroscope data. The largest error in estimated angle from the above table (entry in red) is for the partially balanced scenario with the RSSI Right Dip case (deviation of 0.3 degrees).

$$\text{Maximum Percentage Error} = \frac{2.49-2.19}{2.19} \times 100 \approx 13.7\%$$

The higher percentage error can be attributed to the lack of gyroscope data (no K_{gyro}). Also, as shown in Figure 24 and 22, the energy is distributed between two fairly strong frequency component making it difficult to model the spring equation correctly (uncertainty in value of β). For almost balanced and almost unbalanced, the error is significantly lower as there is one strong frequency component as opposed to two in a partially balanced case.

Appendix H Identifying Window Size for a Moving Average Filter

To determine the ideal window size, it is valuable to consider its relationship with the cutoff frequency of a moving average filter. The continuous-time frequency response of a moving average filter [42] is expressed as:

$$H(f) = \frac{\sin(\pi f M)}{M \sin(\pi f)}$$

M : window size
f : frequency of signal

The cutoff frequency [42] is defined as the frequency of the half-power point where the power gain is half (also called -3 dB-point).

$$\begin{aligned} |H(f)|^2 = \frac{1}{2} \quad &\Rightarrow \quad \frac{\sin^2(\pi f M)}{M^2 \sin^2(\pi f)} = \frac{1}{2} \\ &\Rightarrow \quad \sin^2(\pi f M) - \frac{M^2}{2} \sin^2(\pi f) = 0 \end{aligned}$$

To transition from the continuous-time frequency domain to the discrete-time domain, the scaling $f \rightarrow f/f_s$ can be employed[17]. In the context of the sensor data, the highest frequency of interest is 10 Hz, while the sampling rate (f_s) is 100 Hz. To ensure sufficient margin between the cut-off frequency and highest frequency of interest, the cut-off frequency (f) can be set to 15 Hz. Applying this equation, we obtain $f = 0.15$.

$$\sin^2(\pi\ 0.15\ M) - \frac{M^2}{2} \sin^2(\pi\ 0.15) = 0 \tag{31}$$

Equation (31) presented earlier lacks an analytical solution for calculating M. To address this, numerical methods, specifically the Newton–Raphson method [43] can be employed. Considering the methodology employed and the subsequent results (detailed on the following page), it can be concluded that a window size of 3 samples aligns well with the specified requirements.

[17] A common textual description is "scaling by sample time", which is the same as dividing by sampling rate

The methodology can be summarized as follows:

- Identify the function $g(x)$ for which a solution is required $\big(g(x) = 0\big)$. Referring to Equation (31) and replacing M with x, the following equation is obtained:

$$g(x) = \sin^2(\pi 0.1x) - \frac{x^2}{2}\sin^2(\pi 0.1)$$

- Identify the iterative equation using Newton–Raphson method to solve the equation.

$$\begin{aligned} x_1 &= x_0 - \frac{g(x_0)}{g'(x_0)} \\ x_2 &= x_1 - \frac{g(x_1)}{g'(x_1)} \\ &\vdots \\ x_{n+1} &= x_n - \frac{g(x_n)}{g'(x_n)} \end{aligned}$$

$$\text{where } g'(x_i) = \left.\frac{\partial g(x)}{\partial x}\right|_{x=x_i}$$

- While setting $x = 0$ is an apparent solution, the objective here is to identify a non-zero solution. This can be accomplished by experimenting with different initial values of x until a non-zero solution is reached. The outcomes obtained through the MATLAB code are presented below:

$$\begin{aligned} x_0 = 1 \quad &\Rightarrow \quad x_n = 0 \\ x_0 = 2 \quad &\Rightarrow \quad x_n = 3.0955 \end{aligned}$$

- Because the Equation (31) contains even powers and a sin function of x, both positive and negative values of x will yield the same result. To account for this property, the absolute value is taken and rounded down[18] to the nearest integer value.

$$x_n = 3.0955 \quad \Rightarrow \quad M = 3$$

[18]By rounding down, the cut-off frequency either stays same or increases, which still aligns with the requirement of not impacting the frequency of interest.

References

[1] A. Ometov, D. Moltchanov, M. Komarov, S. V. Volvenko, and Y. Koucheryavy, "Packet Level Performance Assessment of mmWave Backhauling Technology for 3GPP NR Systems", *IEEE Access*, vol. 7, pp. 9860–9871, 2019.

[2] C. A. Balanis, *Antenna theory: Analysis and Design.* John Wiley and Sons, Incorporated, 4 ed., 2016.

[3] "High-capacity Microwave backhaul for all sites". `https://www.ericsson.com/49c940/assets/global/eridoc/405873/31-28701-FGB101004UEN.pdf`. Accessed: 07-August-2023.

[4] Wikipedia contributors, "Fresnel zone — Wikipedia, The Free Encyclopedia". `https://en.wikipedia.org/w/index.php?title=Fresnel_zone&oldid=1164418126`, 2023. Accessed: 07-August-2023.

[5] A. Solyman and K. Yahya, "Evolution of wireless communication networks: from 1G to 6G and future perspective", *International Journal of Electrical and Computer Engineering (IJECE)*, vol. 12, p. 3943, 08 2022.

[6] "Ericsson Microwave Outlook: Wind impact on E-band". `https://www.ericsson.com/4a8c50/assets/local/reports-papers/microwave-outlook/2021/microwave-report-2021-wind-impact-on-e-band.pdf`. Accessed: 11-September-2023.

[7] A. Shami, M. Maier, and C. Assi, *Adaptive Modulation and Coding (AMC)*, ch. 5.4, p. 99–100. Springer, 2010.

[8] "Wireless Backhaul Evolution Delivering next-generation connectivity". `https://www.gsma.com/spectrum/wp-content/uploads/2022/04/wireless-backhaul-spectrum.pdf`. Accessed: 08 July 2023.

[9] F. S. Bertrando and S. Bianchi, "Cross-polarization transmission system with asynchronous receivers", June 2010.

[10] Z. Shen, A. Papasakellariou, J. Montojo, D. Gerstenberger, and F. Xu, "Overview of 3gpp lte-advanced carrier aggregation for 4g wireless communications", *IEEE Communications Magazine*, vol. 50, no. 2, pp. 122–130, 2012.

[11] 3GPP, "5G; NR; Backhaul adaptation protocol (BAP) specification". 3GPP TS 38.340.

[12] V. L. Granatstein, pp. 5–6. CRC Press, 2 ed., 2012.

[13] Wikipedia contributors, "Radiation pattern — Wikipedia, The Free Encyclopedia". `https://en.wikipedia.org/w/index.php?title=Radiation_pattern&oldid=1170090028`, 2023. Accessed: 21-August-2023.

[14] C. Wolff, "Antenna Radiation Pattern". `https://www.radartutorial.eu/06.antennas/Antenna%20Pattern.en.html`. Accessed: 14-September-2023.

[15] Wikipedia contributors, "Rotation — Wikipedia, the free encyclopedia". `https://en.wikipedia.org/w/index.php?title=Rotation&oldid=1168508107`, 2023. Accessed: 15-August-2023.

[16] R. Kalimulin, A. Artemenko, R. Maslennikov, J. Putkonen, and J. Salmelin, "Impact of mounting structures twists and sways on point-to-point millimeter-wave backhaul links", in *2015 IEEE International Conference on Communication Workshop (ICCW)*, pp. 19–24, 2015.

[17] A. R. Schuler, A. Grammatikos, and K. A. Fegley, "Measuring rotational motion with linear accelerometers", *IEEE Transactions on Aerospace and Electronic Systems*, vol. AES-3, no. 3, pp. 465–472, 1967.

[18] A. V. Oppenheim, R. W. Schafer, M. A. Yoder, and W. T. Padgett, *Discrete-time signal processing*. Upper Saddle River, NJ: Pearson, 3 ed., Aug. 2009.

[19] STMicroelectronics, *iNEMO inertial module: always-on 3D accelerometer and 3D gyroscope*.

[20] A. Silberschatz, P. Galvin, and G. Gagne, *Operating System Concepts, 9th edition*. John Wiley & Sons, 2012.

[21] "Free RTOS Description". `https://www.freertos.org/about-RTOS.html`. Accessed: 27-August-2023.

[22] The MathWorks Inc., "Matlab version: 9.13.0 (r2022b)", 2022.

[23] T. Longcore, C. Rich, P. Mineau, B. MacDonald, D. G. Bert, L. M. Sullivan, E. Mutrie, S. A. Gauthreaux, M. L. Avery, R. L. Crawford, A. M. Manville, E. R. Travis, and D. Drake, "Avian mortality at communication towers in the united states and canada: which species, how many, and where?", *Biological Conservation*, vol. 158, pp. 410–419, 2013.

[24] H. Rohling, *OFDM: Concepts for Future Communication Systems*. Springer, 2011.

[25] J. J. Carr, "Chapter 16 - radio receiver basics", in *The Technician's EMI Handbook* (J. J. Carr, ed.), pp. 163–195, Woburn: Newnes, 2000.

[26] B. N. Datta, *Numerical Linear Algebra and applications*. Society for Industrial and Applied Mathematics, 2 ed., 2010.

[27] S. Okamura and T. Oguchi, "Electromagnetic wave propagation in rain and polarization effects", *Proc Jpn Acad Ser B Phys Biol Sci*, vol. 86, no. 6, pp. 539–562, 2010.

[28] 3GPP, "5G; NR; Physical layer procedures for control". 3GPP TS 38.213.

[29] T. S. Rappaport, *Wireless communications: Principles and Practice*, pp. 89–93. Upper Saddle River, N.J: Prentice Hall PTR, 2 ed., 1996.

[30] R. Penrose, "A generalized inverse for matrices", *Mathematical Proceedings of the Cambridge Philosophical Society*, vol. 51, no. 3, p. 406–413, 1955.

[31] S. Silver, *Microwave Antenna Theory and Design*. P. Peregrinus on behalf of the Institution of Electrical Engineers, 1984.

[32] F. Maass *et al.*, "Analytic Approximation to Bessel Function $J_0(x)$", in *Computational and Applied Mathematics, vol. 39, no. 3 p. 222. Link*, 2020.

[33] C. H. Holbrow, J. N. Lloyd, J. C. Amato, E. Galvez, and M. E. Parks, *Modern Introductory Physics*. Springer New York, 2010.

[34] G. B. Arfken, H. J. Weber, and F. E. Harris, *Mathematical Methods for Physicists*. San Diego, CA: Academic Press, 6 ed., July 2005.

[35] A. H. Jazwinski, *Stochastic Processes and Filtering Theory*. Academic Press, 1970.

[36] H. Jiang and C. Dovrolis, "Why is the Internet Traffic Bursty in Short Time Scales?", *SIGMETRICS Perform. Eval. Rev.*, vol. 33, p. 241–252, jun 2005.

[37] J. A. Farrell, F. O. Silva, F. Rahman, and J. Wendel, "Inertial Measurement Unit Error Modeling Tutorial: Inertial Navigation System State Estimation with Real-Time Sensor Calibration", *IEEE Control Systems Magazine*, vol. 42, no. 6, pp. 40–66, 2022.

[38] J. Watkins, "The Mass-Spring Oscillator". `https://www.math.arizona.edu/~jwatkins/h-ode.pdf`. Accessed: 07-August-2023.

[39] F. S. Tse, I. E. Morse, and R. T. Hinkle, *Mechanical vibrations: Theory and applications*. ALLYN AND BACON, 1979.

[40] J. Bezanson, A. Edelman, S. Karpinski, and V. B. Shah, "Julia: A fresh approach to numerical computing", *SIAM Review*, vol. 59, no. 1, pp. 65–98, 2017.

[41] C. Tsitouras, "Runge–Kutta pairs of order 5(4) satisfying only the first column simplifying assumption", *Computers & Mathematics with Applications*, vol. 62, no. 2, pp. 770–775, 2011.

[42] S. W. Smith, *Moving Average Filters*, ch. 15. California Technical Publishing, 1997.

[43] H. R. Wesley, *Numerical Methods for Scientists and Engineers*. Dover, 1973.

Lund University
Department of Automatic Control
Box 118
SE-221 00 Lund Sweden

Document name
MASTER'S THESIS

Date of issue
September 2023

Document Number
TFRT-6218

Author(s)
Nikhil Challa

Supervisor
Henric Broström, Ericsson, Sweden
Frans Erik Isaksson, Ericsson, Sweden
Bo Bernhardsson, Dept. of Automatic Control, Lund University, Sweden
Emma Tegling, Dept. of Automatic Control, Lund University, Sweden (examiner)

Title and subtitle
Estimation of Parabolic Microwave Antenna Movements Using Sensor Fusion

Abstract

Wireless communication has seamlessly integrated itself into our daily lives, with Ericsson pioneering the development of comprehensive mobile ecosystems. As the demand for data traffic continues to surge, the enhancement of both cellular radio systems and backhaul infrastructure remains paramount. Within this context, Ericsson leverages microwave transport network solutions to address backhaul needs. However, the implementation of microwave radio solutions introduces its own set of challenges, particularly concerning physical movements and meteorological fluctuations. The thesis focuses on analyzing a typical link using microwave radio solutions, which rely on a Line of Sight (LoS) path and narrow beam width for high gain. However, the very attribute that renders the link efficient—its narrow beam width—also renders it vulnerable to potential deterioration or malfunction due to factors such as antenna and mast movements.

In response to these challenges, the thesis puts forth a comprehensive solution involving the deployment of sensors for movement detection. This approach encompasses the development of sensor fusion models and innovative signal processing methodologies. The primary objective revolves around accurately estimating the deviation of the antenna's orientation from the optimal LoS alignment. Existing scholarly works have harnessed magnetometer data from an Inertial Measurement Unit (IMU) sensor to refine estimation precision. However, the radio system under consideration features an embedded sensor located directly on its circuitry. This circuitry is ensconced within a casing, potentially offering shielding against external magnetic fields. To bolster the accuracy of the sensor model, the proposed strategy is to incorporate Received Signal Strength Indicator (RSSI) measurements.

The research outlined within the thesis encompasses two areas. First and foremost, it seeks to establish a correlation between the movements of the antenna and the corresponding variations in the received signal strength. By probing this relationship, the aim is to arrive at an understanding of the underlying causes for the observed link degradation. The second facet of this research delves into the domain of estimation using a variant of Kalman Filter. Specifically, the thesis endeavors to estimate the deviation in the antenna's orientation from its optimal alignment. This estimation process is fortified by leveraging properties from historical data to estimate current deviations and possibly forecast future deviations. Moreover, the thesis recommends certain corrective measures that hold the potential to mitigate the impacts of link degradation. However, the implementation or validation of these corrective actions is not explicitly undertaken within the scope of this study. Instead, this constitutes a fertile ground for subsequent research investigations to explore and validate further.

Keywords inertial measurement unit (IMU), received signal strength indicator (RSSI), extended kalman filter (EKF), numerical methods, optimization.			
Classification system and/or index terms (if any)			
Supplementary bibliographical information			
ISSN and key title 0280-5316			*ISBN*
Language English	*Number of pages* 1-157	*Recipient's notes*	
Security classification			

http://www.control.lth.se/publications/